iScience

CellPress
OPEN ACCESS

Article

Donor-Acceptor Conjugated Macrocycles with Polyradical Character and Global Aromaticity

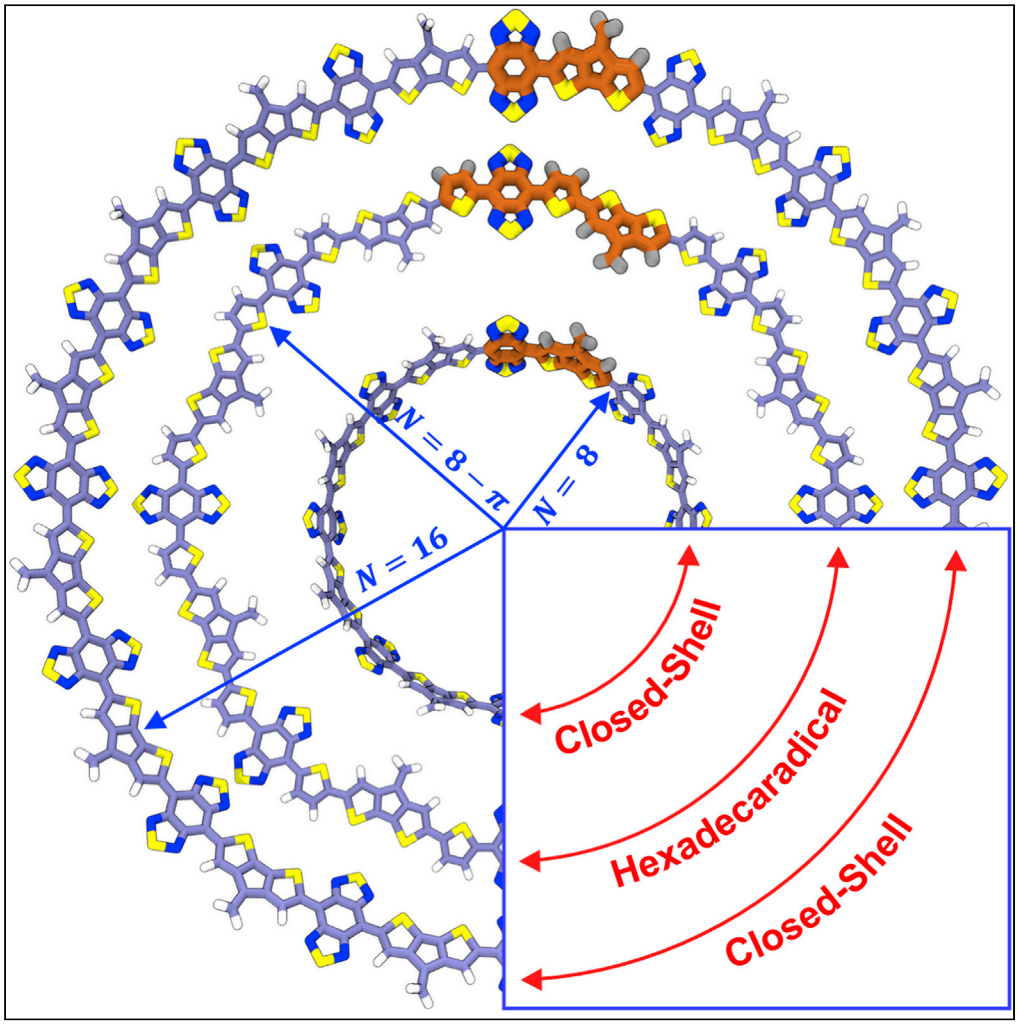

Md Abdus Sabuj, Md Masrul Huda, Neeraj Rai

neerajrai@che.msstate.edu

HIGHLIGHTS

Donor-acceptor macromolecules with open-shell polyradical character are reported.

The antiferromagnetic coupling between the unpaired electrons is modulated with pi-spacer.

The open-shell macrocycles show Baird's aromaticity in the lowest triplet state.

Open-shell macrocycles red-shift absorption spectra.

Sabuj et al., iScience 23, 101675
November 20, 2020
https://doi.org/10.1016/j.isci.2020.101675

iScience

CellPress
OPEN ACCESS

Article

Donor-Acceptor Conjugated Macrocycles with Polyradical Character and Global Aromaticity

Md Abdus Sabuj,[1] Md Masrul Huda,[1] and Neeraj Rai[1,2,*]

SUMMARY

Polyradical character and global aromaticity are fundamental concepts that govern the rational design of cyclic conjugated macromolecules for optoelectronic applications. Here, we report donor-acceptor (D−A) conjugated macromolecules with and without π-spacer derivatives to tune the antiferromagnetic couplings between the unpaired electrons. The macromolecules without π-spacer have a closed-shell electronic configuration and show global nonaromatic character in the singlet and lowest triplet states. However, the derivatives with π-spacer develop a nearly pure open-shell diradical and a very high polyradical character, not reported for D−A type macromolecules. Furthermore, the π-spacer derivatives display global nonaromaticity in the singlet ground state, but global aromaticity in the lowest triplet state, according to Baird's rule. The absorption spectra of the open-shell macromolecules calculated with time-dependent density functional theory indicate intensive light absorption in the near-infrared region and broadening to 2,500 nm, making these materials suitable for numerous optoelectronic applications.

INTRODUCTION

The π-conjugated open-shell organic semiconductors (OSCs) with one or more unpaired electrons in the degenerate or near-degenerate non-bonding molecular orbitals (NBMOs) exhibit unique electronic, optical, and magnetic properties (Lewis, 2015; Stuyver et al., 2019; Rudebusch et al., 2016; Dressler et al., 2018; Gopalakrishna et al., 2018; London et al., 2019; Abe, 2013; Ni et al., 2020a; Rickhaus et al., 2020; Sabuj and Rai, 2020). The open-shell OSCs with di- or polyradical character are of particular interest as their unique electronic structure makes them suitable for optoelectronic applications, such as nonlinear optics, photovoltaics, charge-storage, and spintronics devices (Rajca, 1994; Abe, 2013; Nakano, 2017; Mas-Torrent et al., 2009; Wang et al., 2019). Despite their significance for many technologies, the synthetic routes are not well established for molecules with a higher radical (above diradical) characters. Therefore, new molecular structures are yet to be designed with a significant polyradical character to understand multiple spin-spin interactions (Gopalakrishna et al., 2018) with improved magnetic properties. Arrangement of an alternating donor (D) and acceptor (A) units in a conjugated system is a common approach for tuning the electronic properties. These D−A materials are widely used to design advanced and emerging optoelectronic devices (Dang et al., 2019; Kanimozhi et al., 2012; Yang et al., 2008; Bronstein et al., 2011; Steckler et al., 2009). Although it is commonplace to design, synthesize, and characterize linear π-conjugated D−A oligomers and polymers, very few instances exist for using D−A motifs to design π-conjugated macromolecules with the ring topology.

The traditional approach of designing a diradical molecule is to embed quinoidal units in the π-conjugated system. The aromatic stabilization energy of these subunits overcomes the covalency of a carbon-carbon π-bond to provide the necessary potential to create two unpaired electrons (London et al., 2019). Conceptually, we can expand this process to a larger number of quinoidal units leading to an increased number of aromatic sextet rings, resulting in a large diradical and even polyradical character (Das et al., 2016). Efforts toward designing molecules with polyradical character include cyclic tetracyclopenta[*def,jkl,pqr,vwx*]-tetraphenylene (TCPTP) (Figure 1A) and fused *p*-quinodimethane (*p*-QDM) with a very small tetraradical characters (Nobusue et al., 2015; Hu et al., 2016). Wu et al. have reported several π-conjugated linear and macrocyclic molecules with polyradical character (Das et al., 2016; Lu et al., 2016, 2017; Liu et al., 2019;

[1]Dave C. Swalm School of Chemical Engineering, and Center for Advanced Vehicular Systems, Mississippi State University, Mississippi State, MS 39762, USA

[2]Lead Contact

*Correspondence: neerajrai@che.msstate.edu

https://doi.org/10.1016/j.isci.2020.101675

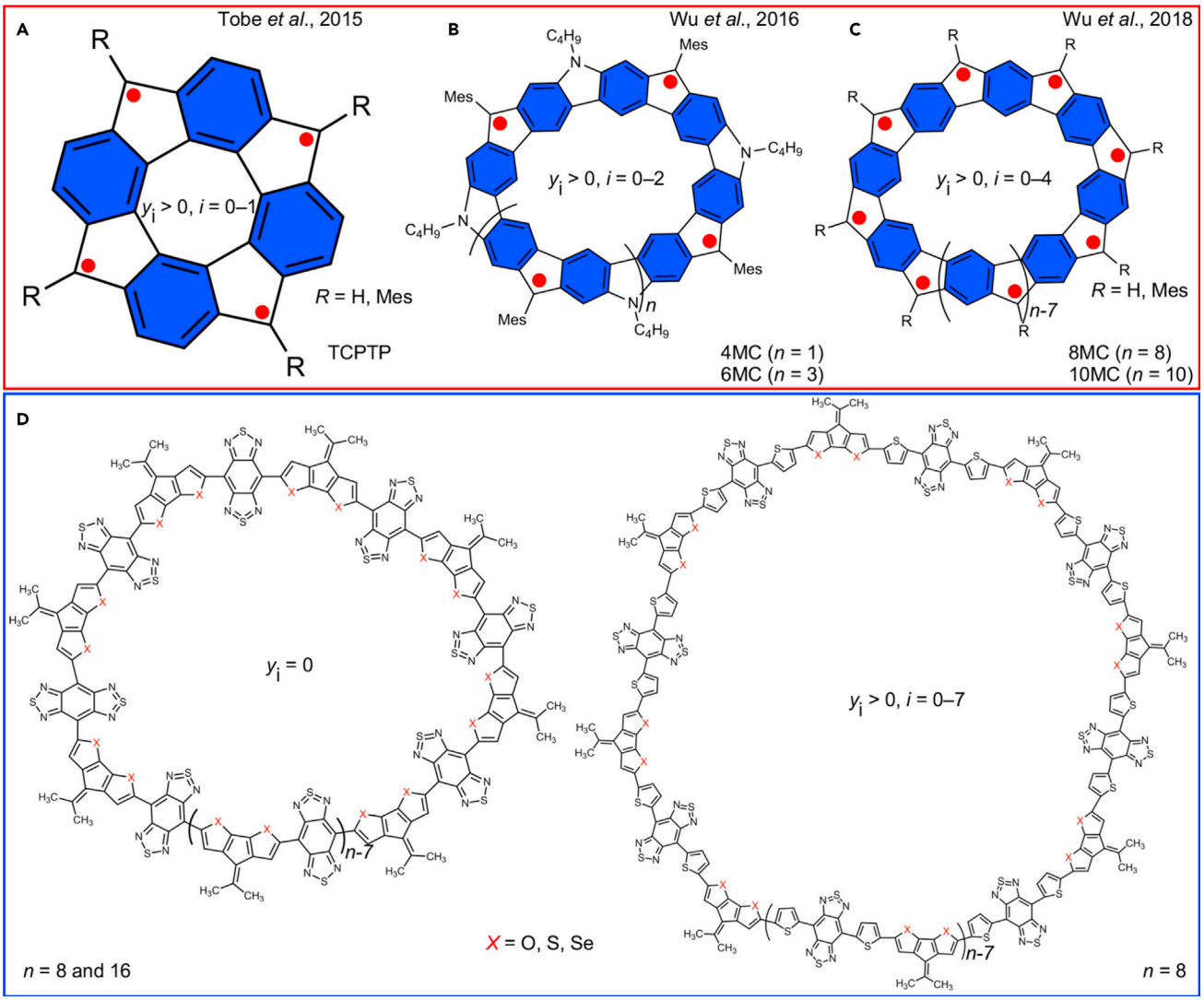

Figure 1. Prototypical Examples of Macromolecular Polyradicaloids

(A–D) (A) TCPTP with a very small tetraradical character; (B) a quinoidal/aromatic carbazole macrocycle with a moderate tetra- and hexaradical characters; (C) an annulene-within-an-annulene (AWA) super-ring structure with decaradical character; and (D) the molecular structures of CPDF-(*X* = O), CPDT-(*X* = S), and CPDS-BBT (*X* = Se) macromolecules with their π-spacer derivatives, having hexadecaradical character studied in this work.

Li et al., 2019b, c). They have synthesized a fully fused quinoidal/aromatic carbazole macrocycle showing a high diradical character with a moderate tetra- and hexaradical characters (Das et al., 2016) (Figure 1B) and an annulene-within-an-annulene (AWA) super-ring structure with decaradical character (Figure 1C) (Liu et al., 2018, 2019). This raises an important question if we can achieve the polyradical character above decaradical in an alternating D–A macromolecule. The cornerstone of polyradical character is the subtle balance between different types of antiferromagnetic (AFM) spin-spin couplings arising within the π-conjugated macrocycle backbone (Liu et al., 2018, 2019; Li et al., 2018). Recent synthetic efforts on D–A macromolecules attempted to tune the highest occupied molecular orbital (HOMO) and lowest unoccupied molecular orbital (LUMO) energy gaps (HOMO-LUMO) by different D–A motifs to analyze optical properties (Ball and Nuckolls, 2015; Van Raden et al., 2016; Yu et al., 2019; Ball et al., 2016, 2018, 2019; Darzi et al., 2015; Kuwabara et al., 2015; Li et al., 2019a). However, cyclic D–A macromolecules with an open-shell character have not been reported in the literature.

It is evident from the prior work (Nobusue et al., 2015; Das et al., 2016; Liu et al., 2018, 2019) that the ring topology facilitates the development of polyradical character due to the high symmetry of these molecular

structures. In this article, we report D−A motifs comprising π-spacer in the ring topology to achieve systems with high polyradical character (Figure 1D). Our study reveals that substitution of π-spacers in D−A molecular backbone can modulate the AFM coupling between the unpaired electrons, developing high polyradical character in a macromolecular system. The rest of the article is organized as follows: first, we discuss the choice of D−A moieties followed by structural features of these macrocycles. In the subsequent sections, we rationalize the evolution of polyradical character based on the electronic structure followed by a discussion on global aromaticity and optical properties.

RESULTS

Selection of Donor and Acceptor Units

The cross-conjugated donors with a highly planar molecular backbone have a high degree of electronic coherence through extended π-conjugation, thereby leading to a small bandgap (London et al., 2017, 2019; Wang et al., 2019; Foster et al., 2014). For example, the cyclopentadithiophene (CPDT) donor, when conjugated with thiadiazoloquinoxaline (TQ) acceptor unit, provides a vanishingly small singlet-triplet energy gap upon increasing oligomer length, resulting into triplet to be the ground state at a longer chain length (London et al., 2019). Here, we have used CPDT and its derivatives cyclopentadifuran (CPDF) and cyclopentadiselenophene (CPDS) as donors and benzo[1,2-c; 4,5-c']bis[1,2,5]thiadiazole (BBT) acceptor to design D−A macrocycles (see Figure 1D). We chose BBT as an acceptor for its high electron affinity and the fact that it intrinsically behaves as a diradical (Liu et al., 2017). As π-spacers can significantly alter the electronic structure, we insert thiophene between the donor and the acceptor units. The heterocyclic quinoidal thiophene unit regains aromatic stabilization energy in the open-shell ground state (Ni et al., 2020b). As a result, macrocycles with thiophene π-spacer achieve a pure diradical character, moderate-to-high polyradical character extending up to hexadecaradical (16 unpaired electrons), and display global aromaticity in the lowest triplet state, following the Baird's rule (*vide infra*) (Baird, 1972). To the best of our knowledge, this is the first report where CPDF-, CPDT-, and CPDS-BBT are rolled into a D−A nano-hoop, which shows not only a very high diradical character but also a significant polyradical character.

Effect of Different Donors and π-Spacer on the Molecular Structure

To understand the effect of donor chemistry and oligomer size on the ring topology, we examine the key geometrical parameters of these macrocycles. The optimized structures of the CPDF-, CPDT-, and CPDS-BBT macrocycles are shown in Figure 2. The CPDT- and CPDS-BBT (n = 8) macromolecules form a bowl-shaped configuration, with a dihedral angle of 175° (Figures S1–S6). The CPDT-BBT (n = 16) has a planar geometry, which improves the π-electron delocalization along the backbone and reduces the reorganization energy (Fei et al., 2017). The CPDS-BBT macromolecule (n = 16) adopts a bowl-shaped configuration with the largest hoop size (58.50 Å) (Williams-Harry et al., 2008). Substitution of the π-spacer (n = 8−π) increases the planarity and hoop size from the macromolecules without π-spacer (n = 8) (Figure 2). Octamer (n = 8) of the CPDF-BBT leads to concavity in the ring structure, whereas the CPDF-BBT macromolecule with n = 16 repeat units form a folded conformation. The difference in the ring topology of CPDF variant with CPDT and CPDS is due to the small bond length between C and O atoms in the donor cyclopenta rings.

Ab initio molecular dynamics (AIMD) simulation is carried out at T = 298.15 K for CPDT-BBT (n = 8) to test the stability of the ring structure. Video S1, related to Figure 2, shows the simulation trajectory of CPDT-BBT (n = 8) macrocycle. The simulation indicates the macromolecule retains its bowl-shaped configuration and the variations are primarily associated with the solubilizing -CH_3 groups. The calculated root-mean-square deviation (RMSD) indicates a plateau is reached after 600 ps (Figure S7A). Also, the ratio of x and y components of the radius of gyration (R_{gx}/R_{gy}) indicates the CPDT-BBT macromolecule retains its ring structure (Figure S7B).

We have analyzed the bond lengths to assess the degree of π-conjugation in the CPDF-, CPDT-, and CPDS-BBT macromolecules (Figures S1–S6). The connecting bonds between a donor and adjacent acceptor unit is 1.39 Å with n = 8 and 16 repeat units, and 1.42 Å for n = 8−π. A smaller linker bond between the donor and acceptor units (Figures S1, S3, and S5) indicates a strong AFM coupling between the paired electrons in the frontier MOs, suppressing polyradical character (Liu et al., 2019; Hu et al., 2016). However, insertion of the thiophene π-spacer increases the length of the linker bonds (1.41–1.42 Å) (Figures S2, S4, and S6), thus reducing the AFM coupling. This reduction in the AFM coupling leads to polyradical character (Liu et al., 2019; Hu et al., 2016). The mixed single and double bond characteristics of the CPDF-, CPDT-, and CPDS-BBT macromolecules indicate a high degree of π-conjugation through the core π framework.

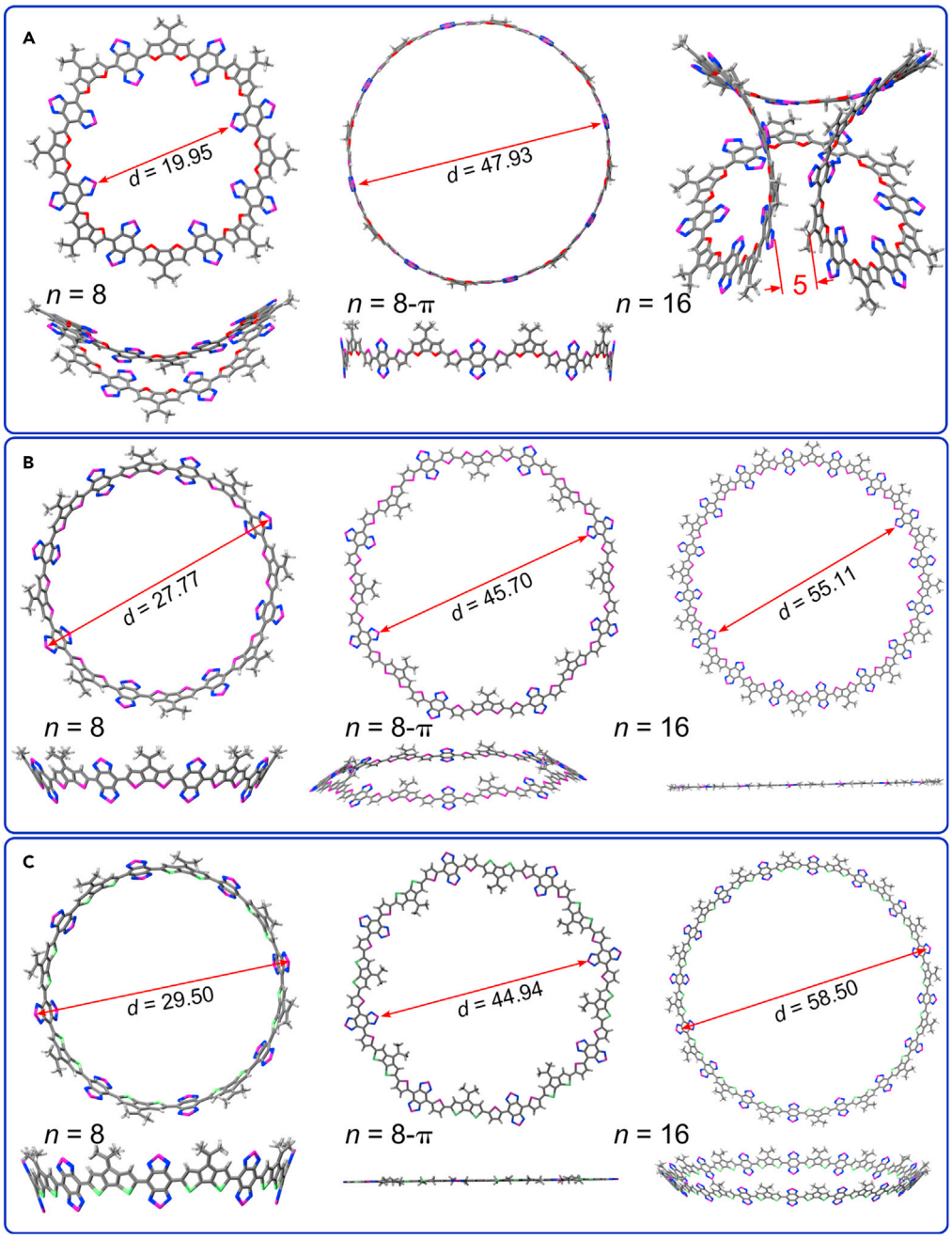

Figure 2. Optimized Configurations of CPDF-, CPDT-, and CPDS-BBT Macromolecules with and without the π-Spacer at C1 Symmetry

(A–C) (A) CPDF-BBT, (B) CPDT-BBT, and (C) CPDS-BBT polymer. Distances are in Å.

See Video S1.

Therefore, the highly π-conjugated macrocycles facilitate delocalization of highest occupied MO (HOMO) and lowest occupied MO (LUMO) throughout the backbone of the CPDF-, CPDT-, and CPDS-BBT (Figures S8–S25), consequently delocalizing the residual charges ($\Delta\rho = S_1 - S_0$) along the rings. The spin density of the singlet open-shell molecules ($n = 8-\pi$) is delocalized along the backbones (Figures S9, S15, and S21), indicating higher thermodynamic stability of the CPDF-, CPDT-, and CPDS-BBT macromolecules in their neutral form.

Polymer	y_0	y_1	y_2	y_3	y_4	y_5	y_6	y_7
CPDF-BBT	0.992	0.517	0.517	0.268	0.268	0.170	0.170	0.144
CPDT-BBT	0.916	0.525	0.525	0.279	0.279	0.179	0.179	0.153
CPDS-BBT	0.937	0.516	0.516	0.267	0.267	0.167	0.167	0.140

Table 1. The Polyradical Character of the CPDF-, CPDT-, and CPDS-BBT with π-Spacers ($n = 8-\pi$). The radical characters reported as the occupation numbers of the lowest unoccupied natural orbitals (LUNO + *i*).

The donor bond lengths indicate two distinct bonding patterns for the macromolecules with and without the π-spacer. For n = 8 and 16 repeat units, the donor units have an alternating single (1.43–1.44 Å) and double bond (1.37–1.38 Å) character (Figures S1–S6), indicating a quinoidal π-conjugated backbone. The six-member ring in the BBT acceptor core has bond lengths close to a single bond (1.45 Å), and the C=N bonds in the thiadiazole rings are shortened. The increased bond length indicates an antiaromatic character in the BBT core with increased aromaticity in the thiadiazole rings. Therefore, a large bond length alternation of these molecules (n = 8 and 16) displays a closed-shell quinoidal form in the ground state.

However, in the case of the π-spacer derivatives ($n = 8-\pi$), the bond length alternation has decreased significantly (Figures S2, S4, and S6). Nearly equal bonds indicate regaining aromaticity of the heteroatom-containing five-member rings in the donor, although quinoidal character exists in the BBT acceptor core. The thiadiazole rings of the BBT acceptor still have equal C=N bonds, indicating larger aromaticity in the open-shell systems ($n = 8-\pi$). It is clear from the bond lengths of each repeat unit that two additional aromatic sextet rings are obtained for each donor along with two thiadiazole rings on the BBT acceptor in the $n = 8-\pi$ macrocycles. Therefore, the aromatic stabilization energy of the π-spacer derivatives has increased to compensate the energy penalty to break double bonds, promoting polyradical character in the CPDF-, CPDT-, and CPDS-BBT macrocycles ($n = 8-\pi$).

Evolution and Origins of Polyradical Character (y_i)

As discussed in the previous section, the addition of π-spacer significantly alters the electronic structure, such as distinct changes in the bond length and aromaticity, which is conducive for the radical character. As a result, the π-spacer derivatives ($n = 8-\pi$) of the CPDF-, CPDT-, and CPDS-BBT show polyradical character (see Table 1). In conjugated systems, there is a delicate competition between the closed-shell and the open-shell electronic structures. As the radical formation requires bond breaking, this endothermic process needs to be closely coupled with the exothermic process such as aromatization, so that the open-shell solution is energetically more favorable. Thus, as the number of potential five- and six-member rings changes from the quinoidal to aromatic resonance structure, so does the "driving force" to create diradical and polyradical characters (Das et al., 2016). It is also important that the aromaticity is recovered in the conjugation path along the backbone of macromolecules. As an example, although two aromatic sextet thiadiazole units are recovered in each BBT unit in the backbone (Figure 3), the CPDF-, CPDT-, and CPDS-BBT macrocycles with n = 8 repeat units do not show any radical character (y_i = 0).

The CPDF-, CPDT-, and CPDS-BBT macromolecules ($n = 8-\pi$) have a near-pure open-shell diradical character (y_0 = 0.90–1.0) (Table 1), where the CPDF-BBT has a slightly higher y_0 than CPDT- and CPDS-BBT macromolecules. The singlet-triplet (ΔE_{ST}) energy gaps of the open-shell molecules calculated with the spin-projection method (Kitagawa et al., 2018) indicate the ΔE_{ST} reduced significantly in the open-shell systems than in the closed-shell systems (Table S1). Also, the CPDF-BBT macromolecule has a lower ΔE_{ST} than the CPDT- and CPDS-BBT ($n = 8-\pi$) macromolecules (Table S1), thus has a higher diradical index. Although there is no clear trend in the energy gap between the singlet and higher spin states, however, a significant reduction in ΔE_{SQT} (singlet-quintet) gap is observed in the CPDS-BBT compared with ΔE_{ST} owing to an increased separation of the unpaired spins from each other in the polymer backbone (Figures S26–S29). However, an increase in the ΔE_{SPT} (singlet-septet) and ΔE_{SNT} (singlet-nonet) is observed from ΔE_{ST} and ΔE_{SQT} owing to an increased electron-electron repulsion in the septet and nonet states of the open-shell CPDF-, CPDT-, and CPDS-BBT ($n = 8-\pi$) macromolecules, which originates from the increased unpaired electron density in the small region.

The π-derivatives also display a high tetraradical (y_1) and hexaradical (y_2) character, moderate octaradical (y_3) and decaradical (y_4) character, and a low dodeca- (y_5), tetradeca- (y_6), and hexadecaradical (y_7)

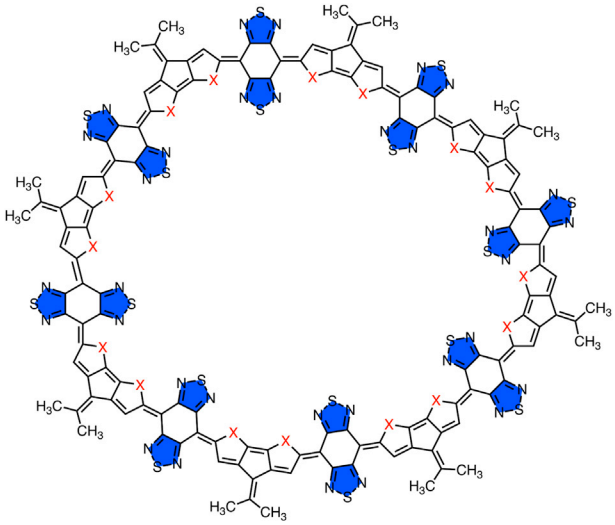

Figure 3. Closed-Shell Resonance Structures

Resonance structures are provided for CPDF-(*X* = O), CPDT-(*X* = S), and CPDS-BBT (*X* = Se) macromolecules with *n* = 8 repeat units. The aromatic thiadiazole units are shown in blue.

character (Table 1). In moving from closed-shell quinoidal form to open-shell configuration, two other aromatic sextet rings in the donor unit gain aromatic stabilization along with the two thiadiazole units in each BBT acceptor (Figures 4, S29–S32). Also, the quinoidal thiophene unit recovers aromaticity in the open-shell ground state (Ni et al., 2020b). Therefore, there is a sufficient energetic driving force for the open-shell form to overcome the covalency to disrupt π bonds. Here, one additional double-bond has been broken to have diradical (2 unpaired electrons) to tetraradical (4 unpaired electrons) and reaching up to hexadecaradical (16 unpaired electrons) characters (Figures S29–S32). Although the polyradical characters are comparable with the reported values in the literature (Das et al., 2016; Lu et al., 2018; Liu et al., 2019), to date, radical characters beyond decaradical is not reported for macrocycles. Owing to the symmetric structure of all the macrocycles, higher energy orbitals are found to be degenerate (Figures S33—S35). Therefore, with similar aromatic stabilization energy, unpaired electrons are generated as a multiple of four. These degenerate MOs (Figures S33–S35) enable higher polyradical character up to hexadecaradical. Interestingly, polyradical character larger than y_0 obtained as pairs, except for the hexadecaradical (y_7). This is due to the degeneracy between LUMO+1 and LUMO+2 (for y_1 and y_2), LUMO+3 and LUMO+4 (for y_3 and y_4) and between LUMO+5 and LUMO+6 (for y_5 and y_6) (Figures S33–S35). The degeneracy lifted after LUMO+6 and higher degenerate orbitals are not energetically accessible. Therefore, the polyradical character is developed up to y_7. We believe that more degenerate orbitals would increase the polyradical character above hexadecaradical; however, DFT calculation is intractable for larger chain lengths with the π-spacer (*n* = 16 −π).

Effect of Ring Size and π-Spacer on Aromaticity

An interesting feature of the π-conjugated macrocycles is that they display global (anti)aromaticity (Ni et al., 2020a; Rickhaus et al., 2020). We use the nucleus-independent chemical shift (NICS) (Schleyer et al., 1996), anisotropy of the induced current density (AICD) (Geuenich et al., 2005), and 2D-iso-chemical shielding surface (2D-ICSS) (Klod and Kleinpeter, 2001) methods to analyze the global (anti)aromaticity of the macrocycles. The CPDF-, CPDT-, and CPDS-BBT macromolecules with *n* = 8 and 16 repeat units have a NICS(0) value close to 0 (Table S2, Figures S1, S3, and S5), indicating global nonaromaticity, with local aromaticity on the individual rings (Lu et al., 2019). Even though the macrocycles with *n* = 8 and 16 repeat units have 96π and 192π (128π and 256π through the hypervalent sulfur of BBT acceptor) (4*N*π) electrons conjugated pathway (Figure 1D), respectively, owing to the very high quinoidal character of these macrocycles, aromaticity is localized on the individual rings along the molecular backbone. This localization of aromaticity can also be observed from the AICD plots and 2D-ICSS maps (Figures S36,S38–S40, S42, and S43–S58), where the ring current is localized on the individual rings and a significant magnetic shielding (negative 2D-ICSS) is observed along the conjugated backbone.

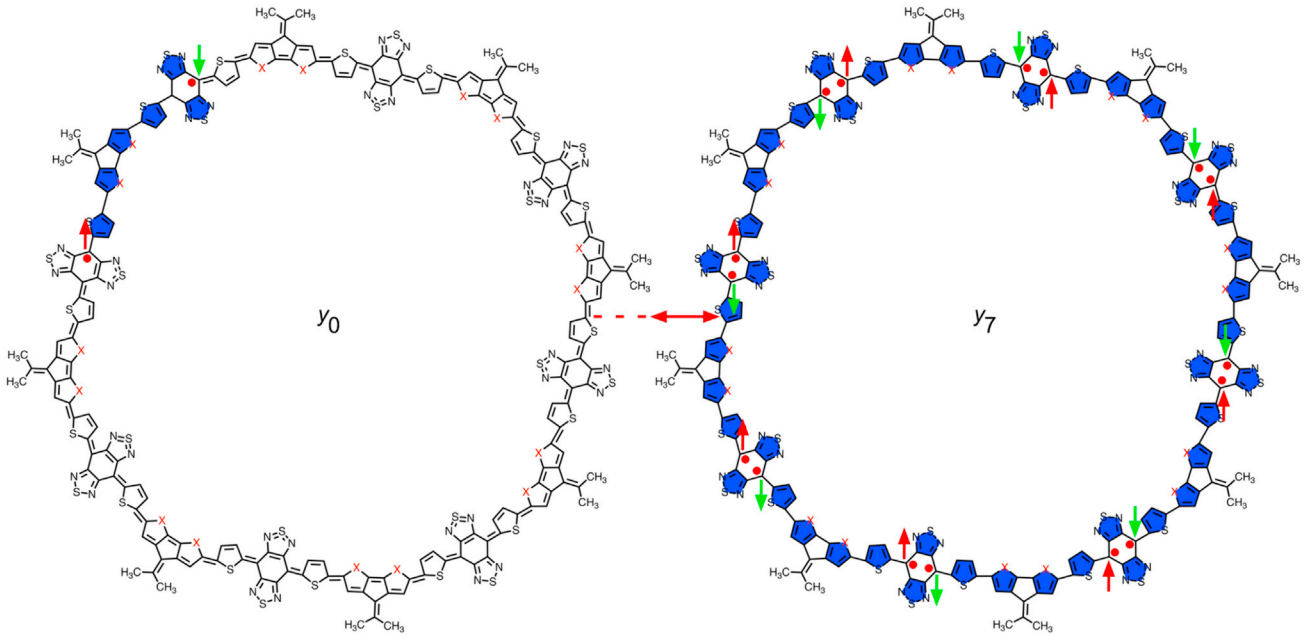

Figure 4. Open-Shell Resonance Structures

Resonance structures are provided for CPDF-(*X* = O), CPDT-(*X* = S), and CPDS-BBT (*X* = Se) macromolecules with *n* = 8−π repeat units. Gradual development of radical characters from diradical to hexadecaradical is due to more aromatic sextet rings (highlighted in blue) in the π-framework. The red and green arrows indicate up- and down-spins, respectively.

See also Figures S29–S32.

The open-shell CPDF-, CPDT-, and CPDS-BBT macromolecules (*n* = 8 −π) also have nonaromatic character, indicated by a very small NICS(0) values at the molecular center (Figures 5A, S2, S4, and S6, Table S3). AICD plots show the ring currents are localized on individual rings, whereas the 2D-ICSS maps show significant magnetic shielding along the molecular backbone (Figures 5A, S37A, and S41A). Although the NICS(0) values for the CPDF-, CPDT-, and CPDS-BBT macromolecules (*n* = 8 −π) in the singlet ground state is close to 0 (Figures 5, S2, S4, and S6), the calculated NICS(0) in their triplet states are negative (−9.82, −10.00, and −10.30 ppm for CPDF-, CPDT-, and CPDS-BBT, respectively) (Table S3, Figures S2, S4, and S6). Therefore, the lowest triplet state of the CPDF-, CPDT-, and CPDS-BBT macromolecules with *n* = 8 −π shows a global aromatic character with 4*N*π electrons, a manifestation of Baird's rule (Baird, 1972). This phenomenon is reported for a highly conjugated bis-rhodium hexaphyrins (Sung et al., 2015) or in an AWA super-ring structure (Liu et al., 2019) but not observed in D−A macromolecules. The AICD plots for the triplet state unambiguously indicate a unidirectional clockwise (diatropic) current flow along the 160π and 192π (4*N*π) electrons conjugated pathway, respectively, which indicates a global aromatic character. The 2D-ICSS maps (Figures 5B, S37B, and S41B) show the inside region of the macrocycles is magnetically shielded (negative 2D-ICSS value), further supporting global aromaticity in the triplet state. The higher energy (quintet, septet, and nonet) states have a very small NICS(0) value (Table S3), indicating global nonaromaticity.

NICS(0) calculations of CPDF-, CPDT-, and CPDS-BBT (*n* = 8) on the individual rings along the backbone indicate the heteroatom-containing five-member rings on the donor units have small aromaticity (NICS(0) ≈ −4.00 to −4.70 ppm), whereas the aromaticity has increased substantially (NICS(0) ≈ −7.00 to −7.75 ppm) in case of the π-spacer derivative (*n* = 8−π) (Figures S1–S6). Therefore, it is evident that the heteroatom-containing five-member rings in the donor unit of the CPDF-, CPDT-, and CPDS-BBT (*n* = 8−π) have regained aromatic character along with the thiadiazole rings in the BBT acceptor unit. The increased aromaticity of the donor units is also consistent with the calculated bond lengths of the open-shell macromolecules (Figures S2, S4, and S6), where reduced bond length alternations on the donor indicated the aromatic character of the heteroatom-containing five-member rings. All the thiophene π-spacers have negative NICS(0) values, recovering aromaticity (Ni et al., 2020b). Therefore, the aromatic stabilization energy has increased in π-spacer derivatives than the unsubstituted systems, facilitating double bond-breaking along the π-conjugated backbone and developing polyradical character.

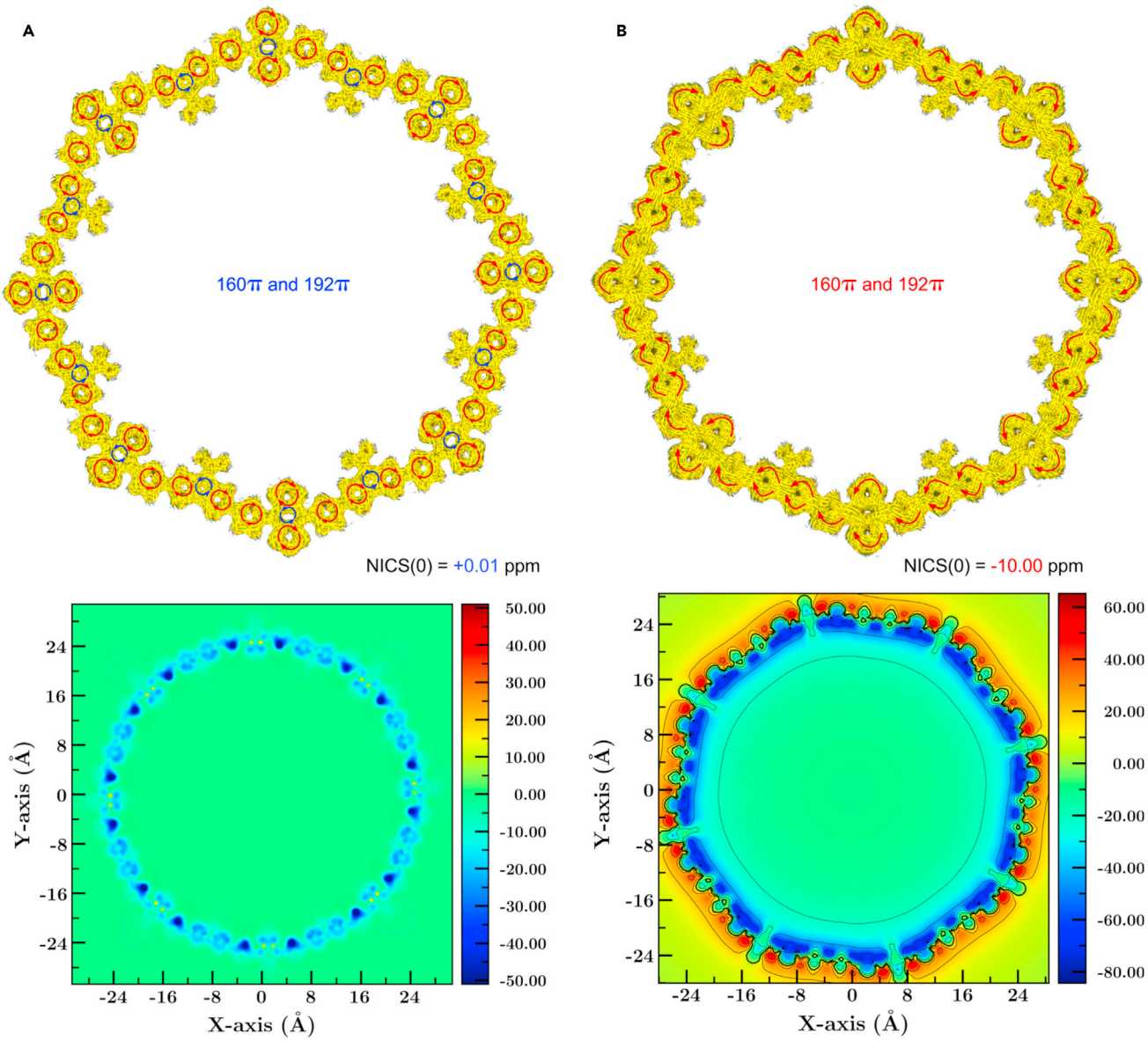

Figure 5. AICD Plots (Top) and 2D-ICSS (Bottom) Maps for CPDT-BBT (n = 8−π)

(A and B) (A) singlet and (B) triplet states. The blue and red arrows along the molecular backbone indicates counter-clockwise (paratropic) and clockwise (diatropic) ring current flow, respectively. The direction of the applied magnetic field is perpendicular to the ring plane and points out through the paper. AICD plots are generated with an isovalue = 0.025 au.

See also Figures S49–S50.

Effect of π-Spacer on the Optical Properties

The optical properties of the macromolecules are explored with the time-dependent density functional theory (TDDFT). It is evident from the calculated spectra that the absorption occurs in the near-infrared (NIR) region (Figure 6). Comparing the absorption spectra of the CPDF-, CPDT-, and CPDS-BBT macromolecules for n = 8 repeat unit, the maximum absorption occurs within 717–756 nm. For the cycloparaphenylenes (CPPs), the maximum absorption reported is only around 340 nm (Jasti et al., 2008), making CPPs less attractive in the optoelectronic devices, whereas in this case, absorption is extended into the NIR region, which is not reported in the case of cyclic D−A macromolecules (Ball et al., 2016, 2019; Li et al., 2019a). A small shoulder is present for both CPDT-BBT and CPDS-BBT macrocycles only with n = 8 repeat units. In the case of CPDT-BBT, the shoulder corresponds to a double-degenerate absorption at 462 nm, with the

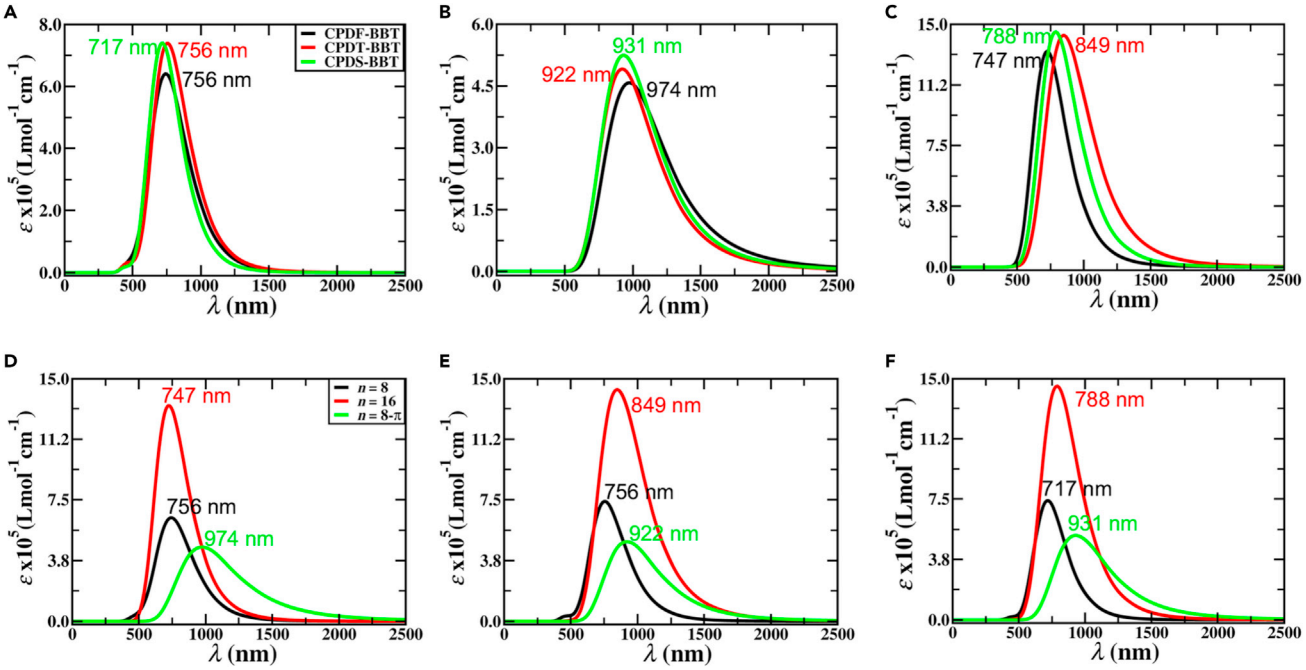

Figure 6. Absorption Spectra of the CPDF-, CPDT-, and CPDS-BBT Macromolecules

(A–F) (A) n = 8, (B) n = 8−π, (C) n = 16, (D) CPDF-BBT, (E) CPDT-BBT, and (F) CPDS-BBT. Calculations are performed with PCM/TD-(U)CAM-B3LYP on the optimized groundstate geometry in the presence of chloroform.

orbital transition occurring from HOMO to LUMO+1 and LUMO+2 (f = 0.3476). Similar orbital transitions involved for CPDS-BBT also, with double-degenerate absorption at 447 nm (f = 0.1861).

The π-conjugation length is elongated in n = 16 repeat units; therefore, the excitation coefficients increased by almost three times than n = 8 and n = 8 −π. The maximum absorption occurs within 747–849 nm, with CPDF-BBT absorption blue-shifted by 9 nm, and CPDT-BBT and CPDS-BBT spectra is red-shifted by 93 and 71 nm from n = 8, respectively. The blue-shift in CPDF-BBT spectra occurs owing to its folded configuration and weaker π-conjugation along the backbone (Figure 2A), although a reduction in the HOMO-LUMO gap is observed from n = 8 to n = 16 (Table S1). Therefore, increasing the chain lengths from n = 8 to 16 facilitates red-shifting the absorption spectra in the CPDT-, and CPDS-BBT macromolecules, indicating a size-dependent absorption in the macrocycles (Williams-Harry et al., 2008).

In the case of the π-spacer derivatives (n = 8−π), the LUMO energies decreased significantly from n = 8 and 16 repeat units of the CPDF-, CPDT-, and CPDS-BBT macromolecules, and an increase in the HOMO energy is observed for CBDT-BBT and CPDS-BBT oligomers; therefore, the calculated E_g decreased significantly (≈0.95 eV) in the open-shell molecules (Table S1). To the best of our knowledge, this is the lowest HOMO-LUMO energy gap of any D−A cyclic macromolecules reported. Owing to the narrowing of the HOMO-LUMO gap, a large red-shift is observed for all π-spacer derivative macromolecules (n = 8−π), now the absorption maximum varies within 922–974 nm. Here, the absorption spectra red-shifted for CPDF-, CPDT-, and CPDS-BBT by 218, 166, and 214 nm from n = 8, respectively, and by 227, 73, and 143 nm from n = 16, respectively. Furthermore, the absorption is broadened up to 2,500 nm, showing extended absorption in the whole near-infrared (NIR) region, which is in accordance with the large polyradical character of the macrocycles (Liu et al., 2018; Das et al., 2016).

All the optical excitations from the ground to the first singlet excited state ($S_0 \rightarrow S_1$) are optically forbidden (Table 2), indicated by zero oscillator strengths (f = 0.0) for the transition. Similar findings were reported for cyclic CPPs and other macrocycles (Darzi and Jasti, 2015). This forbidden transition included electronic excitation from HOMO →LUMO, which indicates the high symmetry of these molecular orbitals involved in the transition. Interestingly, all the allowed transitions obtained were doubly degenerate both for closed- and open-shell macromolecules. This is due to the degenerate MOs for CPDF-, CPDT-, and CPDS-BBT

Polymer	*n*	Excitations	E^*_g (eV)	λ (nm)	*f*	Orbital Contributions	
CPDF-BBT	8	$S_0 \rightarrow S_1$	1.44	862.24	0.00	H→L (37%) H→L+1 (35%) H→L+2 (35%) H→L+4 (30%)	
		$S_0 \rightarrow S_2$	1.64	757.29	7.25		
		$S_0 \rightarrow S_3$	1.64	756.22	7.26		
		$S_0 \rightarrow S_5$	1.97	628.53	2.42		
	16	$S_0 \rightarrow S_1$	1.41	878.03	0.01	H-1→L+1 (13%) H-2→L (19%) H→L+1 (13%) H→L+3 (16%) H→L+4 (14%) H→L+4 (14%)	
		$S_0 \rightarrow S_2$	1.45	851.59	0.98		
		$S_0 \rightarrow S_3$	1.46	849.45	1.05		
		$S_0 \rightarrow S_5$	1.66	747.24	14.96		
		$S_0 \rightarrow S_6$	1.77	698.62	8.54		
		$S_0 \rightarrow S_7$	1.77	698.62	8.54		
	8-π	$S_0 \rightarrow S_1$	1.22	1015.70	0.00	H(α)→L(α) (16%)	H(β)→L(β) (16%)
		$S_0 \rightarrow S_2$	1.27	974.03	5.61	H(α)→L(α)+1 (16%)	H(β)-2→L(β) (14%)
		$S_0 \rightarrow S_3$	1.27	974.03	5.61	H(α)→L(α)+2 (16%)	H(β)-1→L(β) (14%)
CPDT-BBT	8	$S_0 \rightarrow S_1$	1.45	853.95	0.00	H→L (34%) H→L+1 (34%) H→L+2 (34%)	
		$S_0 \rightarrow S_2$	1.64	853.95	9.13		
		$S_0 \rightarrow S_3$	1.64	755.80	9.13		
	16	$S_0 \rightarrow S_1$	1.40	887.48	0.00	H→L (18%) H→L+1 (13%) H→L+2 (13%)	
		$S_0 \rightarrow S_2$	1.46	849.22	17.69		
		$S_0 \rightarrow S_3$	1.46	849.22	17.69		
	8-π	$S_0 \rightarrow S_1$	1.30	956.34	0.00	H(α)→L(α) (16%)	H(β)→L(β) (16%)
		$S_0 \rightarrow S_2$	1.34	921.79	6.03	H(α)→L(α)+1 (12%)	H(β)→L(β)+2 (16%)
		$S_0 \rightarrow S_3$	1.34	921.79	6.03	H(α)→L(α)+2 (13%)	H(β)→L(β)+1 (16%)
CPDS-BBT	8	$S_0 \rightarrow S_1$	1.56	794.60	0.00	H→L (31%) H→L+1 (31%) H→L+2 (31%)	
		$S_0 \rightarrow S_2$	1.73	716.95	9.13		
		$S_0 \rightarrow S_3$	1.73	716.95	9.13		
	16	$S_0 \rightarrow S_1$	1.52	817.63	0.00	H→L (16%) H→L+1 (16%) H→L+2 (16%)	
		$S_0 \rightarrow S_2$	1.57	788.39	17.95		
		$S_0 \rightarrow S_3$	1.57	788.39	17.95		
	8-π	$S_0 \rightarrow S_1$	1.28	967.65	0.00	H(α)→L(α) (16%)	H(β)→L(β) (16%)
		$S_0 \rightarrow S_2$	1.33	930.79	6.45	H(α)→L(α)+1 (15%)	H(β)-2→L(β) (14%)
		$S_0 \rightarrow S_3$	1.33	930.79	6.45	H(α)→L(α)+2 (15%)	H(β)-2→L(β) (14%)

Table 2. Optical Properties for CPDF-, CPDT-, and CPDS-BBT Macromolecules as a Function of Oligomer Length (*n*). The calculated excitations from the ground state, excitation energies (E^*_g), the wavelength of the excitations (λ), oscillator strength of the excitations (*f*), MOs involved in the transitions, and the percent contribution of the individual transitions. Calculations performed at PCM/(U)CAM-B3LYP level and chloroform used as an implicit solvent.

macromolecules (Figures S33–S35). The allowed transitions involved excitation from the ground to the second and third excited states ($S_0 \rightarrow S_2$ and $S_0 \rightarrow S_3$) (Table 2), except for CPDF-BBT (*n* = 16), where all the excitations from lower energy states are allowed, having S_6 and S_7 excited states as doubly degenerate. For the closed-shell macromolecules, the allowed transitions assigned as HOMO to LUMO+1, HOMO to

LUMO+2, and HOMO to LUMO+4. For CPDF-BBT (n = 16), the maximum oscillator strength (f = 14.96) observed in HOMO to LUMO+3 transition, with degenerate excitation assigned to HOMO to LUMO+5 and HOMO to LUMO+6. In the case of the open-shell macromolecules, the HOMO to LUMO transitions is still forbidden, with allowed transition assigned to HOMO-2 to LUMO, HOMO-1 to LUMO, and the other allowed transition obtained similar to the closed-shell system.

DISCUSSION

We have designed D−A macromolecules with and without thiophene π-spacer. Macromolecules with the π-spacer show a near pure diradical character and moderate-to-high polyradical character, not previously observed in D−A type macrocycles. The closed-shell macromolecules have higher singlet-triplet and HOMO-LUMO energy gaps and a global nonaromatic character. However, the open-shell molecules have a significantly reduced singlet-triplet and HOMO-LUMO energy gaps. Although the macromolecules without π-spacer have a quinoidal character, the π-spacer derivatives benefit from the aromatic stabilization energy in the donor units. Therefore, the π-spacer derivatives develop a near pure diradical and moderate-to-high polyradical character, extended to hexadecaradical (16 unpaired electrons). Although the singlet ground state shows a global nonaromatic character, the lowest triplet state of the open-shell macromolecules indicates a global aromatic character following Baird's rule, which has not been observed for the D−A type macromolecules. The delocalized spin density distribution of the open-shell macromolecules indicates their thermodynamic stability in the neutral form. Furthermore, the TDDFT calculations show that the open-shell macromolecules absorb photons in the NIR region with absorption spectra broadening to 2,500 nm. Going from the closed-shell to the open-shell macromolecules, we observe a significant red-shift in the absorption maxima. Our work shows that the CPDF-, CPDT- and CPDS-BBT macrocycles are potential synthetic targets for optoelectronic devices, particularly as NIR sensors, charge-storage devices, and in non-linear optics (NLO) applications.

Limitations of the Study

In this work, we have considered the electronic structure of the isolated gas-phase molecules using density functionals (B3LYP, CAM-B3LYP, PBE-D3, see supplementary information) that have worked best for a specific molecular property based on our past experiences. One can use different functionals to calculate molecular properties provided these functionals exhibit low spin contamination. It is also desirable to compute ensemble averages for molecular properties and include solvation effects. The large system sizes (the largest system is approximately 6 nm) considered in the present work precludes *ab initio* molecular dynamics simulations with explicit solvent molecules. The solvents used in the synthesis of these materials tend to non-polar molecules with low dielectric constant. Thus, we expect solvothermal effects to be similar for macromolecules considered in this work.

Resource Availability

Lead Contact

Correspondence and requests for materials should be addressed to Neeraj Rai (email: neerajrai@che.msstate.edu).

Materials Availability

This study did not generate new unique reagents.

Data and Code Availability

The data that support the findings of this study are available from the Lead Contact Neeraj Rai upon reasonable request.

METHODS

All methods can be found in the accompanying Transparent Methods supplemental file.

SUPPLEMENTAL INFORMATION

Supplemental Information can be found online at https://doi.org/10.1016/j.isci.2020.101675.

ACKNOWLEDGMENTS

This work is supported by the National Science Foundation (NSF) under grant no. OIA-1757220. The DFT calculations were performed at the high-performance computing center at Mississippi State University. Also, the Extreme Science and Engineering Discovery Environment (XSEDE) is used, which is supported by NSF grant number ACI-1548562. We acknowledge the Texas Advanced Computing Center (TACC) at The University of Texas at Austin for providing (HPC, Stampede 2 [through XSEDE allocation, TG-CHE140141]) resources that have contributed to the research results reported within this paper.

AUTHOR CONTRIBUTIONS

M.A.S. conceived the design idea and performed the DFT calculations and analysis with inputs from N.R. M.A.S. wrote the first draft of the manuscript. M.M.H. developed codes for generating AICD and 2D-ICSS diagrams and performed the AIMD simulations and analysis. N.R. supervised the project and revised the manuscript.

DECLARATION OF INTERESTS

The authors declare that they have no competing financial interests.

Received: April 29, 2020
Revised: September 1, 2020
Accepted: October 9, 2020
Published: November 20, 2020

REFERENCES

Abe, M. (2013). Diradicals. Chem. Rev. *113*, 7011–7088.

Baird, N.C. (1972). Quantum organic photochemistry. ii. resonance and aromaticity in the lowest 3. pi.. pi.* state of cyclic hydrocarbons. J. Am. Chem. Soc. *94*, 4941–4948.

Ball, M., and Nuckolls, C. (2015). Stepping into the Light: Conjugated Macrocycles with Donor–Acceptor Motifs. ACS Cent Sci *1*, 416–417.

Ball, M., Zhang, B., Zhong, Y., Fowler, B., Xiao, S., Ng, F., Steigerwald, M., and Nuckolls, C. (2019). Conjugated macrocycles in organic electronics. Acc. Chem. Res. *52*, 1068–1078.

Ball, M., Zhong, Y., Fowler, B., Zhang, B., Li, P., Etkin, G., Paley, D.W., Decatur, J., Dalsania, A.K., and Li, H. (2016). Macrocyclization in the design of organic n-type electronic materials. J. Am. Chem. Soc. *138*, 12861–12867.

Ball, M.L., Zhang, B., Xu, Q., Paley, D.W., Ritter, V.C., Ng, F., Steigerwald, M.L., and Nuckolls, C. (2018). Influence of molecular conformation on electron transport in giant, conjugated macrocycles. J. Am. Chem. Soc. *140*, 10135–10139.

Bronstein, H., Chen, Z., Ashraf, R.S., Zhang, W., Du, J., Durrant, J.R., Shakya Tuladhar, P., Song, K., Watkins, S.E., and Geerts, Y. (2011). Thieno [3, 2-b] thiophene- diketopyrrolopyrrole-containing polymers for high-performance organic field-effect transistors and organic photovoltaic devices. J. Am. Chem. Soc. *133*, 3272–3275.

Dang, D., Yu, D., and Wang, E. (2019). Conjugated donor–acceptor terpolymers toward high-efficiency polymer solar cells. Adv. Mater. *31*, 1807019.

Darzi, E.R., Hirst, E.S., Weber, C.D., Zakharov, L.N., Lonergan, M.C., and Jasti, R. (2015). Synthesis, properties, and design principles of donor–acceptor nanohoops. ACS Cent. Sci. *1*, 335–342.

Darzi, E.R., and Jasti, R. (2015). The dynamic, size-dependent properties of [5]–[12] cycloparaphenylenes. Chem. Soc. Rev. *44*, 6401–6410.

Das, S., Herng, T.S., Zafra, J.L., Burrezo, P.M., Kitano, M., Ishida, M., Gopalakrishna, T.Y., Hu, P., Osuka, A., and Casado, J. (2016). Fully fused quinoidal/aromatic carbazole macrocycles with poly-radical characters. J. Am. Chem. Soc. *138*, 7782–7790.

Dressler, J.J., Teraoka, M., Espejo, G.L., Kishi, R., Takamuku, S., Gómez-García, C.J., Zakharov, L.N., Nakano, M., Casado, J., and Haley, M.M. (2018). Thiophene and its sulfur inhibit indenoindenodibenzothiophene diradicals from low-energy lying thermal triplets. Nat. Chem. *10*, 1134–1140.

Fei, Z., Han, Y., Gann, E., Hodsden, T., Chesman, A.S., McNeill, C.R., Anthopoulos, T.D., and Heeney, M. (2017). Alkylated selenophene-based ladder-type monomers via a facile route for high-performance thin-film transistor applications. J. Am. Chem. Soc. *139*, 8552–8561.

Foster, M.E., Zhang, B.A., Murtagh, D., Liu, Y., Sfeir, M.Y., Wong, B.M., and Azoulay, J.D. (2014). Solution-processable donor–acceptor polymers with modular electronic properties and very narrow bandgaps. Macromol. Rapid Commun. *35*, 1516–1521.

Geuenich, D., Hess, K., Köhler, F., and Herges, R. (2005). Anisotropy of the induced current density (acid), a general method to quantify and visualize electronic delocalization. Chem. Rev. *105*, 3758–3772.

Gopalakrishna, T.Y., Zeng, W., Lu, X., and Wu, J. (2018). From open-shell singlet diradicaloids to polyradicaloids. ChemComm *54*, 2186–2199.

Hu, P., Lee, S., Herng, T.S., Aratani, N., Gonçalves, T.P., Qi, Q., Shi, X., Yamada, H., Huang, K.W., and Ding, J. (2016). Toward tetraradicaloid: the effect of fusion mode on radical character and chemical reactivity. J. Am. Chem. Soc. *138*, 1065–1077.

Jasti, R., Bhattacharjee, J., Neaton, J.B., and Bertozzi, C.R. (2008). Synthesis, characterization, and theory of [9]-,[12]-, and [18] cycloparaphenylene: carbon nanohoop structures. J. Am. Chem. Soc. *130*, 17646–17647.

Kanimozhi, C., Yaacobi-Gross, N., Chou, K.W., Amassian, A., Anthopoulos, T.D., and Patil, S. (2012). Diketopyrrolopyrrole–diketopyrrolopyrrole-based conjugated copolymer for high-mobility organic field-effect transistors. J. Am. Chem. Soc. *134*, 16532–16535.

Kitagawa, Y., Saito, T., and Yamaguchi, K. (2018). Approximate spin projection for broken-symmetry method and its application. In Symmetry (Group Theory) and Mathematical Treatment in Chemistry, A. Takashiro, ed., pp. 121–139.

Klod, S., and Kleinpeter, E. (2001). Ab initio calculation of the anisotropy effect of multiple bonds and the ring current effect of arenes—application in conformational and configurational analysis. J. Chem. Soc. Perkin. Trans. *2*, 1893–1898.

Kuwabara, T., Orii, J., Segawa, Y., and Itami, K. (2015). Curved oligophenylenes as donors in shape-persistent donor–acceptor macrocycles

with solvatofluorochromic properties. Angew. Chem. Int. Ed. *54*, 9646–9649.

Lewis, S.E. (2015). Cycloparaphenylenes and related nanohoops. Chem. Soc. Rev. *44*, 2221–2304.

Li, C., Wang, C., Guo, Y., Jin, Y., Yao, N., Wu, Y., Zhang, F., and Li, W. (2019a). A diketopyrrolopyrrole-based macrocyclic conjugated molecule for organic electronics. J. Mater. Chem. C *7*, 3802–3810.

Li, G., Gopalakrishna, T.Y., Phan, H., Herng, T.S., Ding, J., and Wu, J. (2018). From open-shell singlet diradicaloid to closed-shell global antiaromatic macrocycles. Angew. Chem. *130*, 7284–7288.

Li, G., Han, Y., Zou, Y., Lee, J.J.C., Ni, Y., and Wu, J. (2019b). Dearomatization approach toward superbenzoquinone-based diradicaloid, tetraradicaloid, and hexaradicaloid. Angew. Chem. *131*, 14457–14464.

Li, Z., Gopalakrishna, T.Y., Han, Y., Gu, Y., Yuan, L., Zeng, W., Casanova, D., and Wu, J. (2019c). [6] cyclo-para-phenylmethine: an analog of benzene showing global aromaticity and open-shell diradical character. J. Am. Chem. Soc. *141*, 16266–16270.

Liu, C., Ni, Y., Lu, X., Li, G., and Wu, J. (2019). Global aromaticity in macrocyclic polyradicaloids: Huckel's rule or baird's rule? Acc. Chem. Res. *52*, 2309–2321.

Liu, C., Sandoval-Salinas, M.E., Hong, Y., Gopalakrishna, T.Y., Phan, H., Aratani, N., Herng, T.S., Ding, J., Yamada, H., and Kim, D. (2018). Macrocyclic polyradicaloids with unusual super-ring structure and global aromaticity. Chem *4*, 1586–1595.

Liu, Y., Phan, H., Herng, T.S., Gopalakrishna, T.Y., Ding, J., and Wu, J. (2017). Toward benzobis (thiadiazole)-based diradicaloids. Chem. Asian J. *12*, 2177–2182.

London, A.E., Chen, H., Sabuj, M., Tropp, J., Saghayezhian, M., Eedugurala, N., Zhang, B., Liu, Y., Gu, X., Wong, B., et al. (2019). A high-spin ground-state donor-acceptor conjugated polymer. Sci. Adv. *5*, eaav2336.

London, A.E., Huang, L., Zhang, B.A., Oviedo, M.B., Tropp, J., Yao, W., Wu, Z., Wong, B.M., Ng, T.N., and Azoulay, J.D. (2017). Donor–acceptor polymers with tunable infrared photoresponse. Polym. Chem. *8*, 2922–2930.

Lu, X., Gopalakrishna, T.Y., Han, Y., Ni, Y., Zou, Y., and Wu, J. (2019). Bowl-shaped carbon nanobelts showing size-dependent properties and selective encapsulation of c70. J. Am. Chem. Soc. *141*, 5934–5941.

Lu, X., Gopalakrishna, T.Y., Phan, H., Herng, T.S., Jiang, Q., Liu, C., Li, G., Ding, J., and Wu, J. (2018). Global aromaticity in macrocyclic cyclopenta-fused tetraphenanthrenylene tetraradicaloid and its charged species. Angew. Chem. *130*, 13236–13240.

Lu, X., Lee, S., Hong, Y., Phan, H., Gopalakrishna, T.Y., Herng, T.S., Tanaka, T., Sandoval-Salinas, M.E., Zeng, W., and Ding, J. (2017). Fluorenyl based macrocyclic polyradicaloids. J. Am. Chem. Soc. *139*, 13173–13183.

Lu, X., Lee, S., Kim, J.O., Gopalakrishna, T.Y., Phan, H., Herng, T.S., Lim, Z., Zeng, Z., Ding, J., and Kim, D. (2016). Stable 3, 6-linked fluorenyl radical oligomers with intramolecular antiferromagnetic coupling and polyradical characters. J. Am. Chem. Soc. *138*, 13048–13058.

Mas-Torrent, M., Crivillers, N., Mugnaini, V., Ratera, I., Rovira, C., and Veciana, J. (2009). Organic radicals on surfaces: towards molecular spintronics. J. Mater. Chem. *19*, 1691–1695.

Nakano, M. (2017). Open-shell-character-based molecular design principles: applications to nonlinear optics and singlet fission. Chem. Rec. *17*, 27–62.

Ni, Y., Gopalakrishna, T.Y., Phan, H., Kim, T., Herng, T.S., Han, Y., Tao, T., Ding, J., Kim, D., and Wu, J. (2020a). 3d global aromaticity in a fully conjugated diradicaloid cage at different oxidation states. Nat. Chem. *12*, 242–248.

Ni, Y., Gopalakrishna, T.Y., Wu, S., and Wu, J. (2020b). A stable all-thiophene-based core-modified [38] octaphyrin diradicaloid: conformation and aromaticity switch at different oxidation states. Angew. Chem. Int. Ed. *59*, 7414–7418.

Nobusue, S., Miyoshi, H., Shimizu, A., Hisaki, I., Fukuda, K., Nakano, M., and Tobe, Y. (2015). Tetracyclopenta [def, jkl, pqr, vwx] tetraphenylene: a potential tetraradicaloid hydrocarbon. Angew. Chem. Int. Ed. *54*, 2090–2094.

Rajca, A. (1994). Organic diradicals and polyradicals: from spin coupling to magnetism? Chem. Rev. *94*, 871–893.

Rickhaus, M., Jirasek, M., Tejerina, L., Gotfredsen, H., Peeks, M.D., Haver, R., Jiang, H.W., Claridge, T.D., and Anderson, H.L. (2020). Global aromaticity at the nanoscale. Nat. Chem. *12*, 236–241.

Rudebusch, G.E., Zafra, J.L., Jorner, K., Fukuda, K., Marshall, J.L., Arrechea-Marcos, I., Espejo, G.L., Ortiz, R.P., Gómez-García, C.J., and Zakharov, L.N. (2016). Diindeno-fusion of an anthracene as a design strategy for stable organic biradicals. Nat. Chem. *8*, 753–759.

Sabuj, M.A., and Rai, N. (2020). Open-shell donor−π−acceptor conjugated metal-free dyes for dye-sensitized solar cells. Mol. Syst. Des. Eng. https://doi.org/10.1039/D0ME00091D.

Schleyer, P.v.R., Maerker, C., Dransfeld, A., Jiao, H., and van Eikema Hommes, N.J. (1996). Nucleus-independent chemical shifts: a simple and efficient aromaticity probe. J. Am. Chem. Soc. *118*, 6317–6318.

Steckler, T.T., Zhang, X., Hwang, J., Honeyager, R., Ohira, S., Zhang, X.H., Grant, A., Ellinger, S., Odom, S.A., and Sweat, D. (2009). A spray-processable, low bandgap, and ambipolar donor- acceptor conjugated polymer. J. Am. Chem. Soc. *131*, 2824–2826.

Stuyver, T., Chen, B., Zeng, T., Geerlings, P., De Proft, F., and Hoffmann, R. (2019). Do diradicals behave like radicals? Chem. Rev. *119*, 11291–11351.

Sung, Y.M., Yoon, M.C., Lim, J.M., Rath, H., Naoda, K., Osuka, A., and Kim, D. (2015). Reversal of hückel (anti) aromaticity in the lowest triplet states of hexaphyrins and spectroscopic evidence for baird's rule. Nat. Chem. *7*, 418.

Van Raden, J., Darzi, E., Zakharov, L., and Jasti, R. (2016). Synthesis and characterization of a highly strained donor–acceptor nanohoop. Org. Biomol. Chem. *14*, 5721–5727.

Wang, K., Huang, L., Eedugurala, N., Zhang, S., Sabuj, M.A., Rai, N., Gu, X., Azoulay, J.D., and Ng, T.N. (2019). Wide potential window supercapacitors using open-shell donor–acceptor conjugated polymers with stable n-doped states. Adv. Energy Mater. *9*, 1902806.

Williams-Harry, M., Bhaskar, A., Ramakrishna, G., Goodson, T., Imamura, M., Mawatari, A., Nakao, K., Enozawa, H., Nishinaga, T., and Iyoda, M. (2008). Giant thienylene-acetylene-ethylene macrocycles with large two-photon absorption cross section and semishape-persistence. J. Am. Chem. Soc. *130*, 3252–3253.

Yang, Y., Farley, R.T., Steckler, T.T., Eom, S.H., Reynolds, J.R., Schanze, K.S., and Xue, J. (2008). Near infrared organic light-emitting devices based on donor-acceptor-donor oligomers. Appl. Phys. Lett. *93*, 388.

Yu, Y., Bian, L., Zhang, Y., Liu, Z., Li, Y., Zhang, R., Ju, R., Yin, C., Yang, L., and Yi, M. (2019). Synthesis of donor–acceptor gridarenes with tunable electronic structures for synaptic learning memristor. ACS Omega *4*, 5863–5869.

iScience, Volume *23*

Supplemental Information

Donor-Acceptor Conjugated Macrocycles with Polyradical Character and Global Aromaticity

Md Abdus Sabuj, Md Masrul Huda, and Neeraj Rai

Table S1: Related to Table 1. Calculated electronic properties for the CPDF-, CPDT-, and CPDS-BBT macromolecules as a function repeating units.

Polymer	n	ΔE_{ST}	ΔE_{SQT}	ΔE_{SSP}	ΔE_{SNT}	HOMO	LUMO	E_g
	8	-0.545	-	-	-	-4.24	-3.01	1.23
CPDF-BBT	8-π	-0.120	-0.119	-0.433	-0.541	-4.25	-3.30	0.95
	16	-0.545	-	-	-	-4.10	-2.96	1.14
	8	-0.563	-	-	-	-4.52	-3.24	1.28
CPDT-BBT	8-π	-0.130	-0.169	-0.402	-0.605	-4.39	-3.42	0.97
	16	-0.537	-	-	-	-4.47	-3.25	1.22
	8	-0.639	-	-	-	-4.62	-3.22	1.40
CPDS-BBT	8-π	-0.122	-0.107	-0.410	-0.642	-4.38	-3.43	0.95
	16	-0.618	-	-	-	-4.58	-3.23	1.35

Table S2: Related to Figure 5. NICS(0) (ppm) values for CPDF-, CPDT-, and CPDS-BBT calculated for singlet and triplet states at the center of the macromolecule.

Polymer	n	singlet	triplet
CPDF-BBT	8	0.28	0.22
	16	-	-
CPDT-BBT	8	-0.21	-0.24
	16	0.06	0.06
CPDS-BBT	8	-0.23	-0.25
	16	0.00	0.00

Table S3: Related to Figure 5. NICS(0) (ppm) values for CPDF-, CPDT-, and CPDS-BBT with $n = 8-\pi$ calculated at the center of the macromolecule.

Polymer	singlet	triplet	quintet	septet	nonet
CPDF-BBT	-0.12	-9.82	-0.1187	-	-0.1149
CPDT-BBT	+0.01	-10.00	+0.009	-0.002	+0.009
CPDS-BBT	+0.04	-10.30	+0.047	-	+0.048

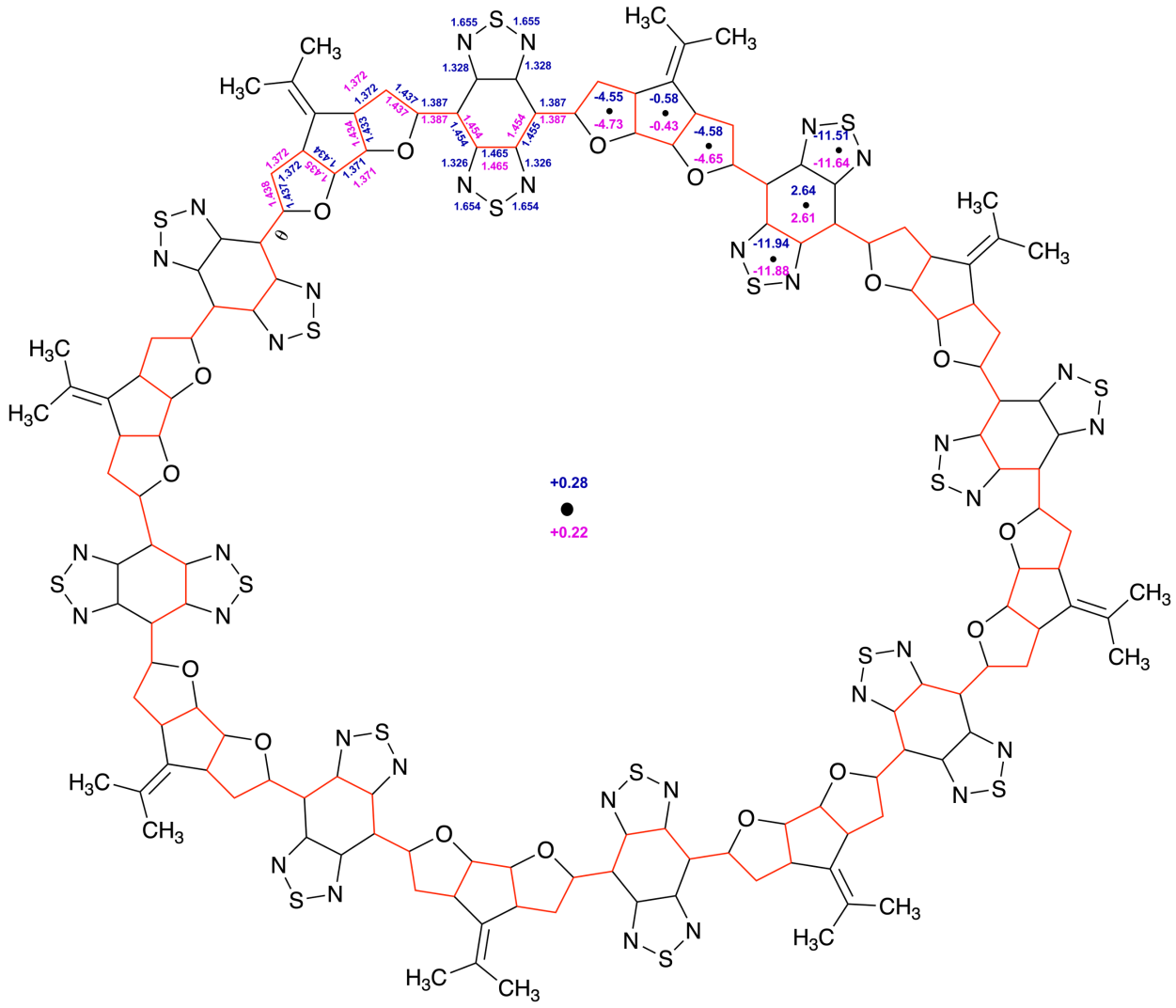

Figure S1: Related to Figure 2. Bond lengths (Å) and NICS(0) (ppm) values for CPDF-BBT (n = 8) calculated at (U)B3LYP/6-31G** level of theory and basis set.

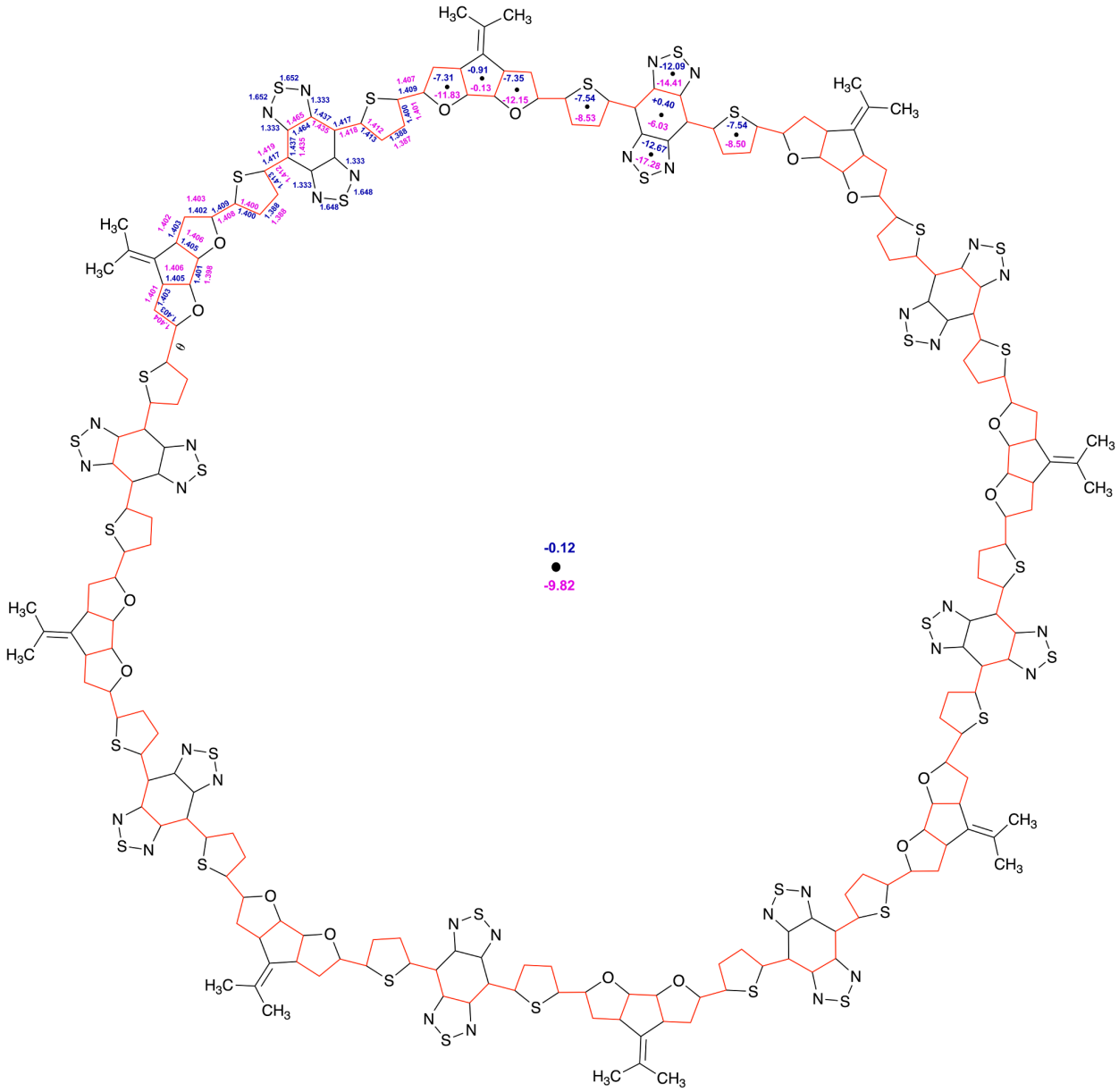

Figure S2: Related to Figure 2. Bond lengths (Å) and NICS(0) (ppm) values for CPDF-BBT ($n = 8 - \pi$) calculated at UB3LYP/6-31G** level of theory and basis set.

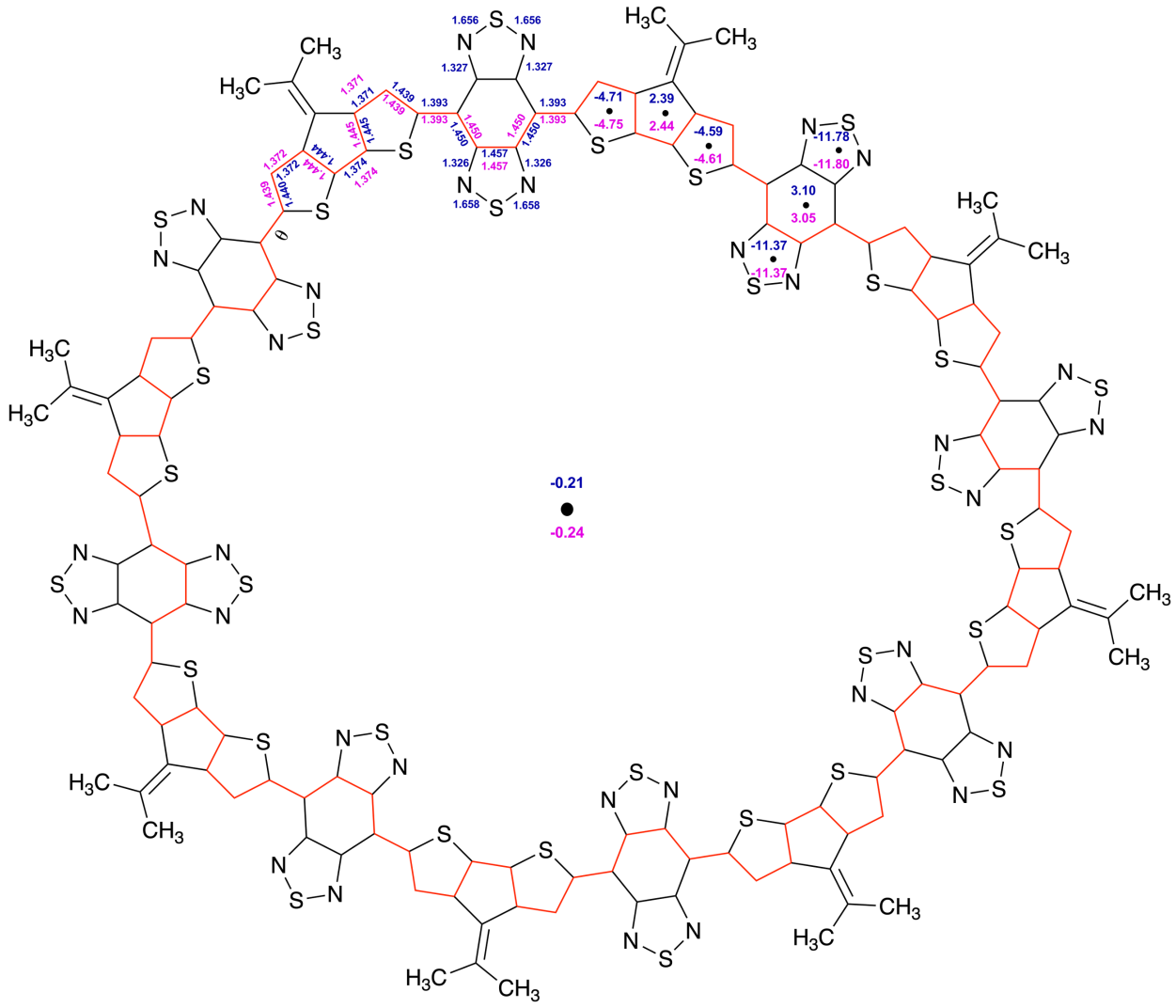

Figure S3: Related to Figure 2. Bond lengths (Å) and NICS(0) (ppm) values for CPDT-BBT (n = *8*) calculated at (U)B3LYP/6-31G** level of theory and basis set.

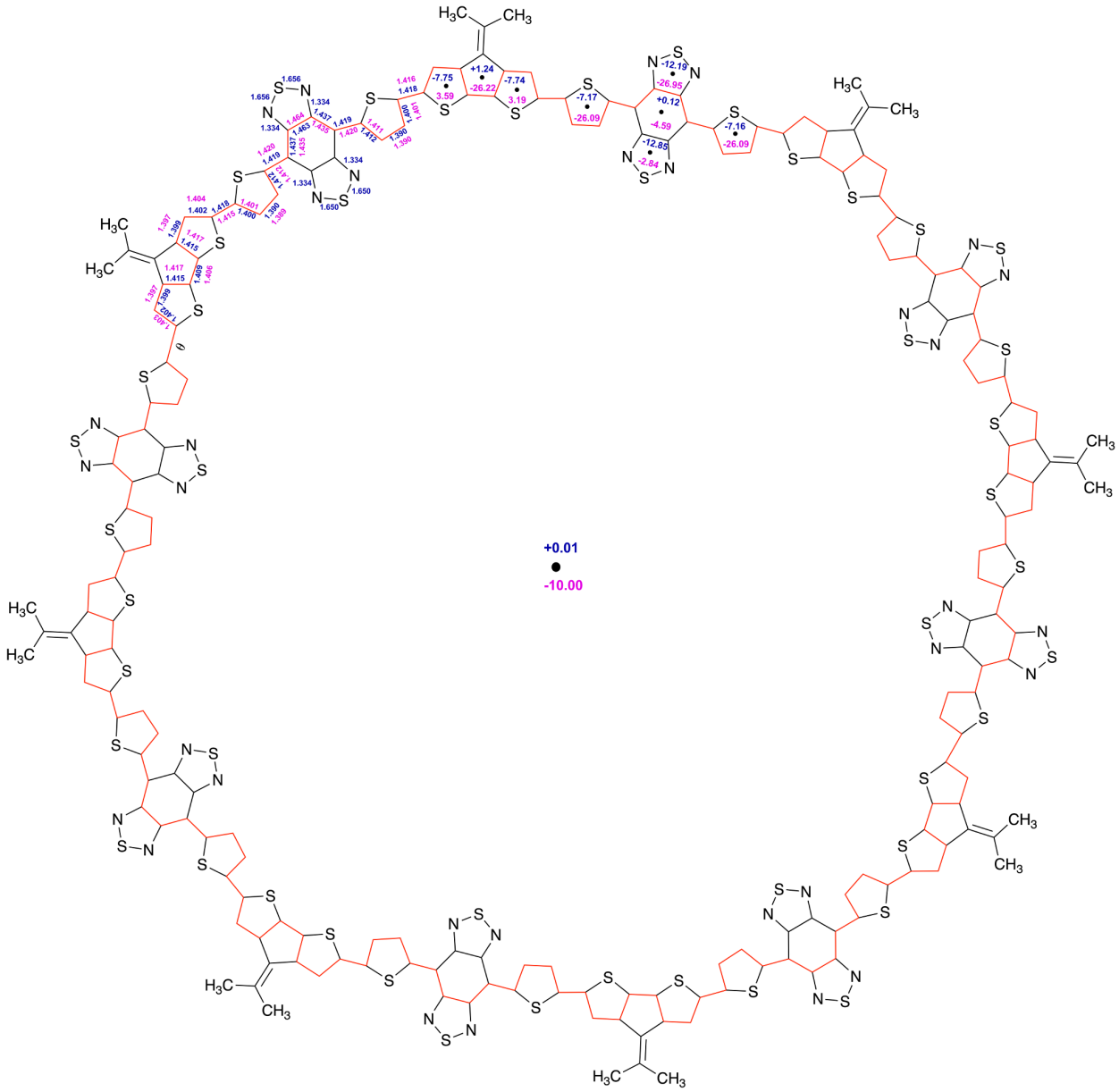

Figure S4: Related to Figure 2. Bond lengths (Å) and NICS(0) (ppm) values for CPDT-BBT ($n = 8 - \pi$) calculated at UB3LYP/6-31G** level of theory and basis set.

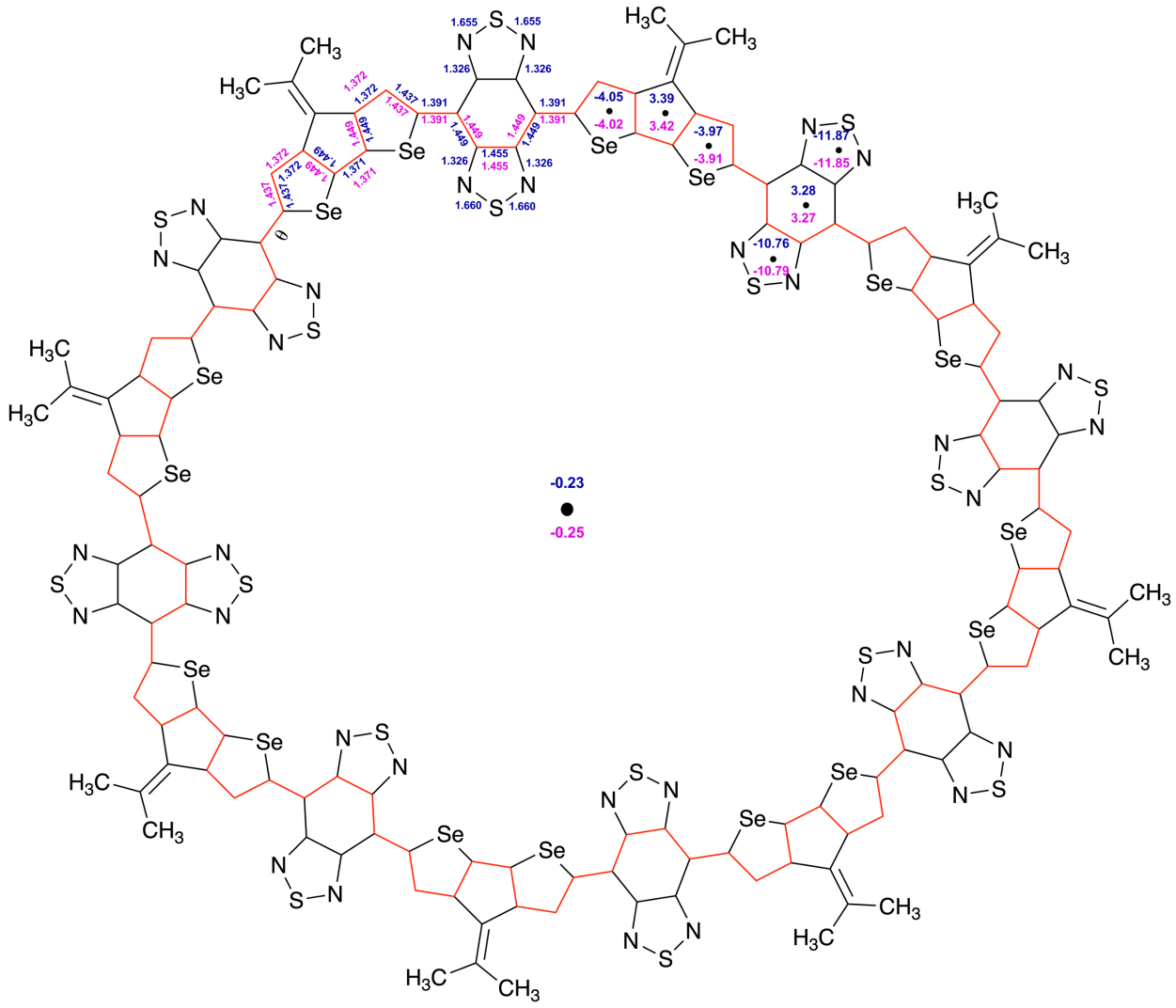

Figure S5: Related to Figure 2. Bond lengths (Å) and NICS(0) (ppm) values for CPDS-BBT (n = 8) calculated at (U)B3LYP/6-31G** level of theory and basis set.

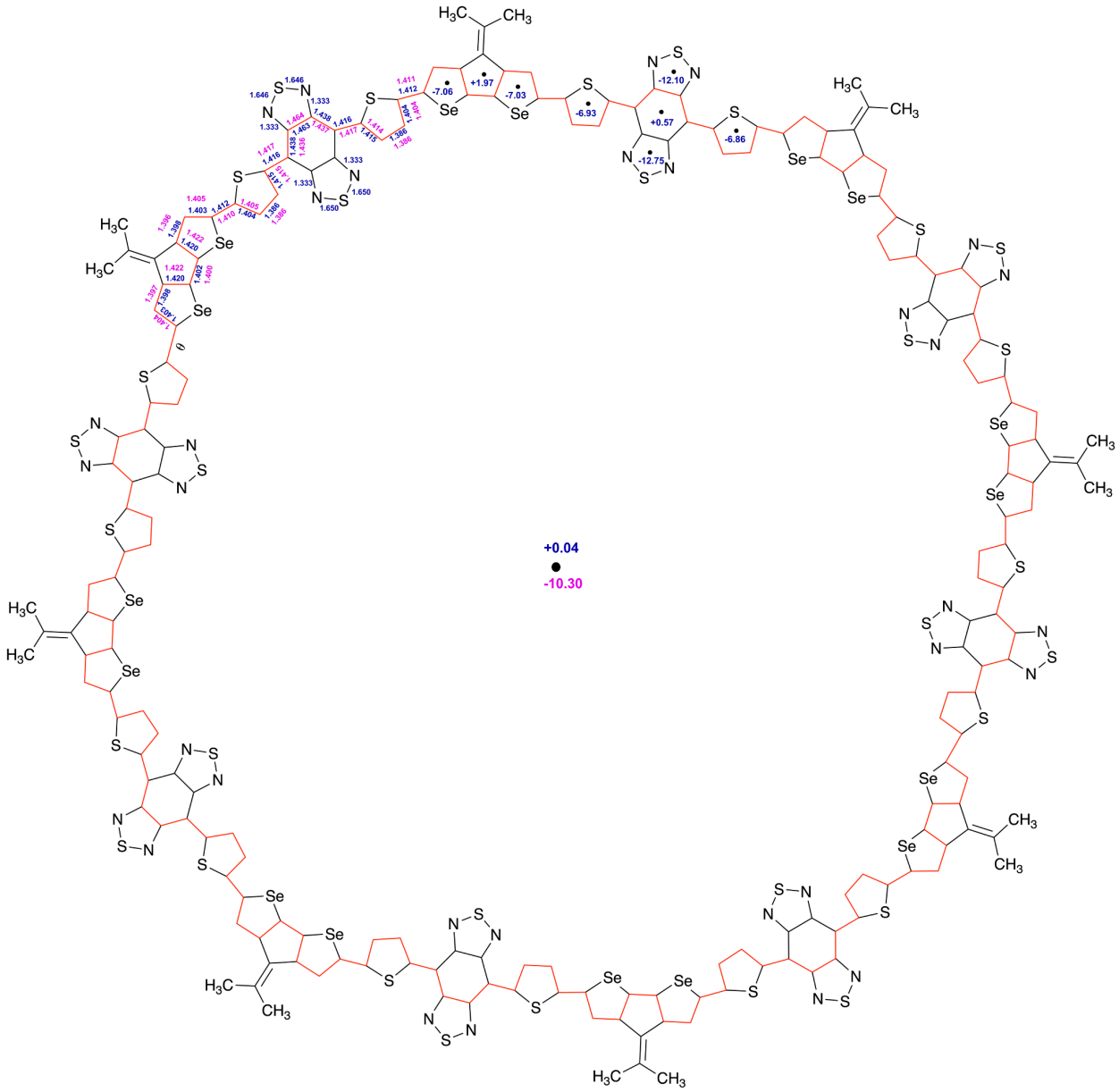

Figure S6: Related to Figure 2. Bond lengths (Å) and NICS(0) (ppm) values for CPDS-BBT ($n = 8 - \pi$) calculated at UB3LYP/6-31G** level of theory and basis set.

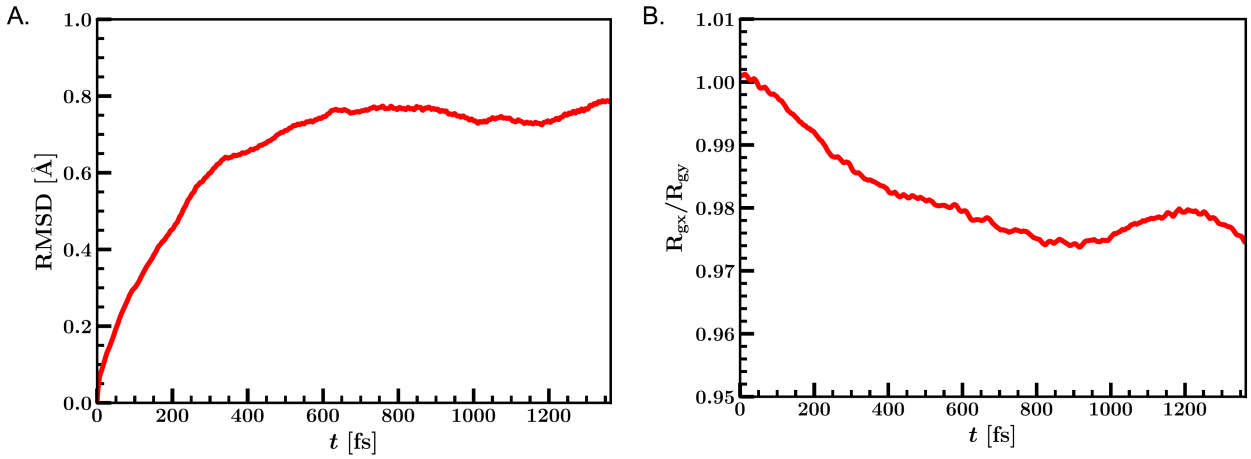

Figure S7: Related to Figure 2. (A) Root mean square deviation (RMSD) and (B) ratio of *x* and *y* component of radius of gyration (R_{gx}/R_{gy}) for CPDT-BBT (n = 8) macromolecule.

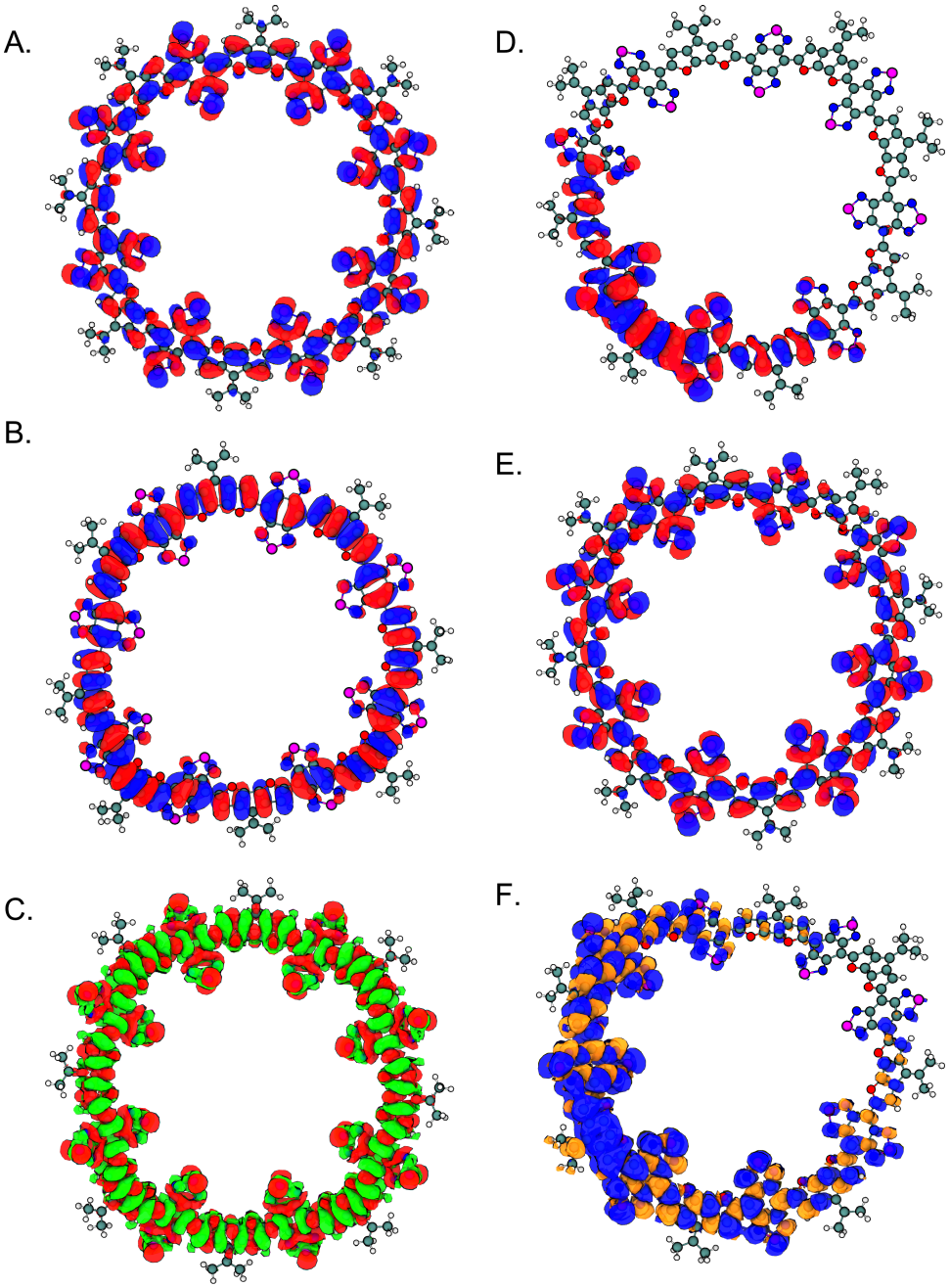

Figure S8: Related to Figure 2. Molecular orbital (MO) diagram and spin density distribution of CPDF-BBT polymer for $n = 8$. (A) HOMO and (B) LUMO for the closed-shell singlet state, (C) spin density difference ($\Delta\rho$) between the first singlet excited state and ground electronic state ($\Delta\rho = S_1 - S_0$), (D) SOMO and (E) SOMO-1 for the triplet state, (F) spin density of the triplet state.

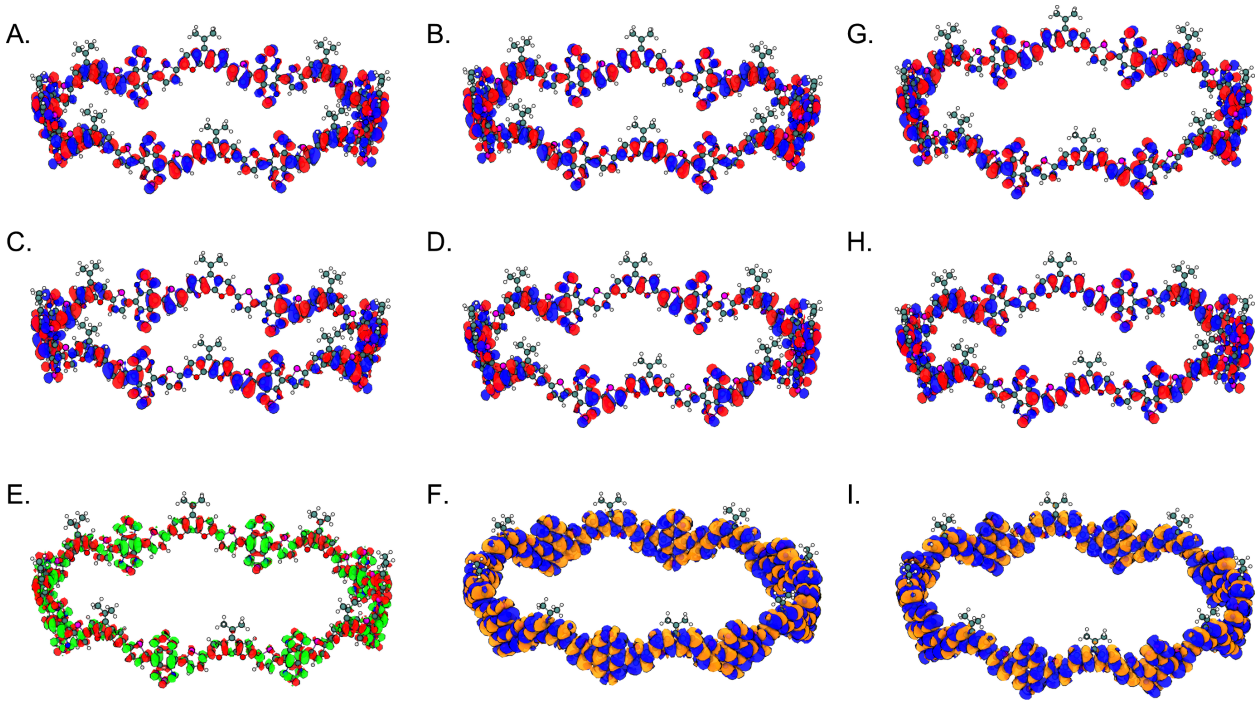

Figure S9: Related to Figure 2. Molecular orbital (MO) diagram and spin density distribution of CPDF-BBT polymer for $n = 8 - \pi$. (A) α-SOMO, (B) β-SOMO, (C) α-LUMO and (D) β-LUMO for the open-shell singlet state, (E) spin density difference ($\Delta\rho$) between the first singlet excited state and ground electronic state ($\Delta\rho = S_1 - S_0$), (G) SOMO and (H) SOMO-1 for the triplet state, (F) and (I) are spin density of the singlet and triplet state.

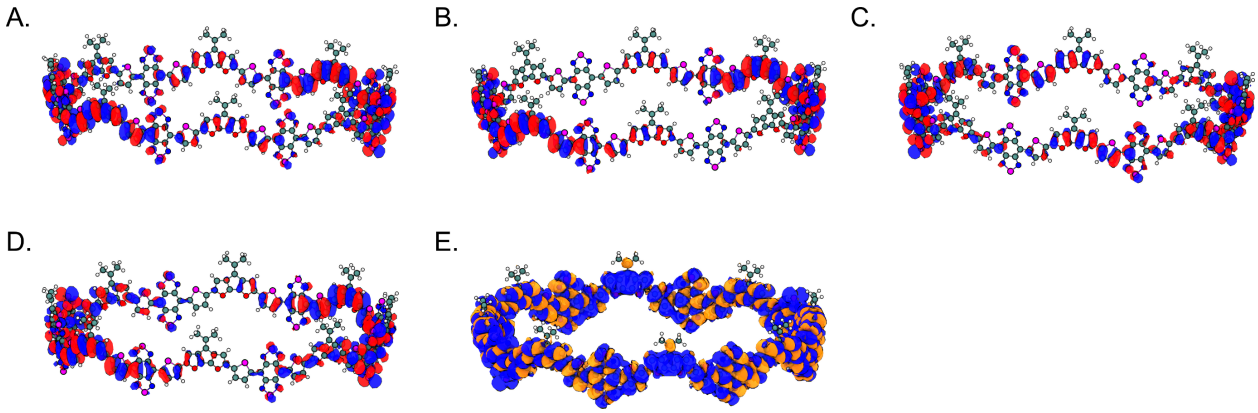

Figure S10: Related to Figure 2. Molecular orbital (MO) diagram and spin density distribution of CPDF-BBT polymer for $n = 8 - \pi$. (A) SOMO, (B) SOMO-1, (C) SOMO-2, (D) SOMO-3 for quintet state, (E) spin density of the quintet state.

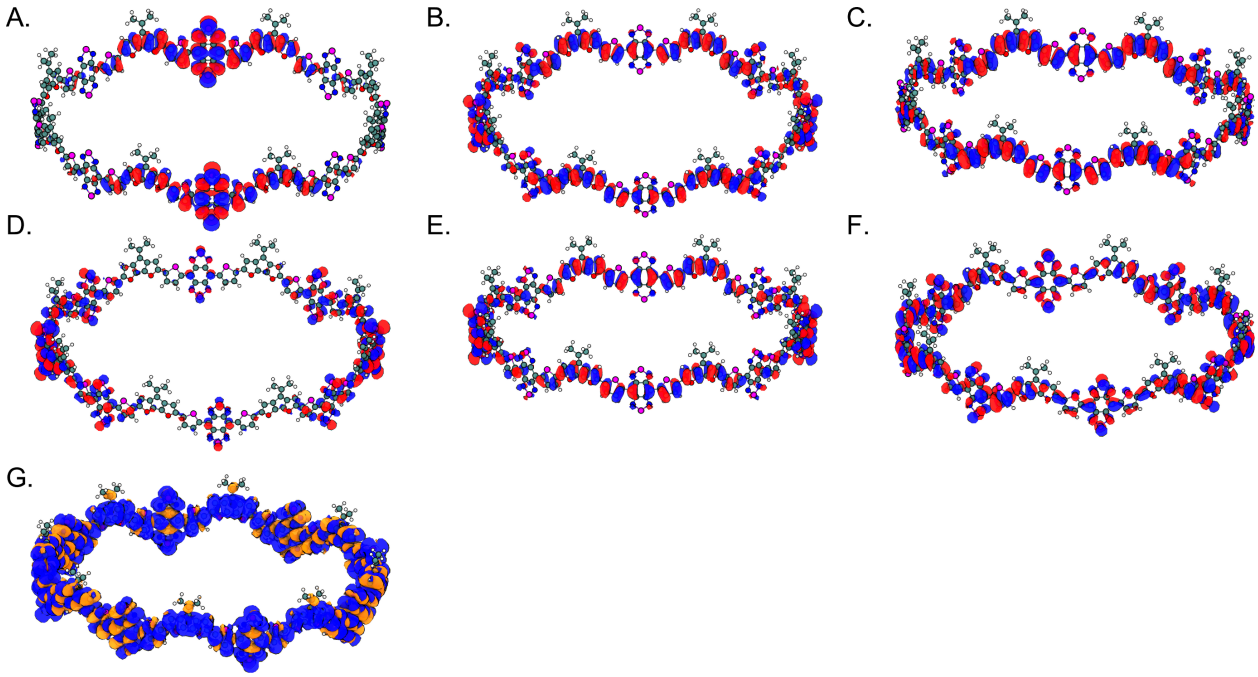

Figure S11: Related to Figure 2. Molecular orbital (MO) diagram and spin density distribution of CPDF-BBT polymer for $n = 8 - \pi$. (A) SOMO, (B) SOMO-1, (C) SOMO-2, (D) SOMO-3 (E) SOMO-4, and (F) SOMO-5 for the septet state, (G) spin density of the septet state.

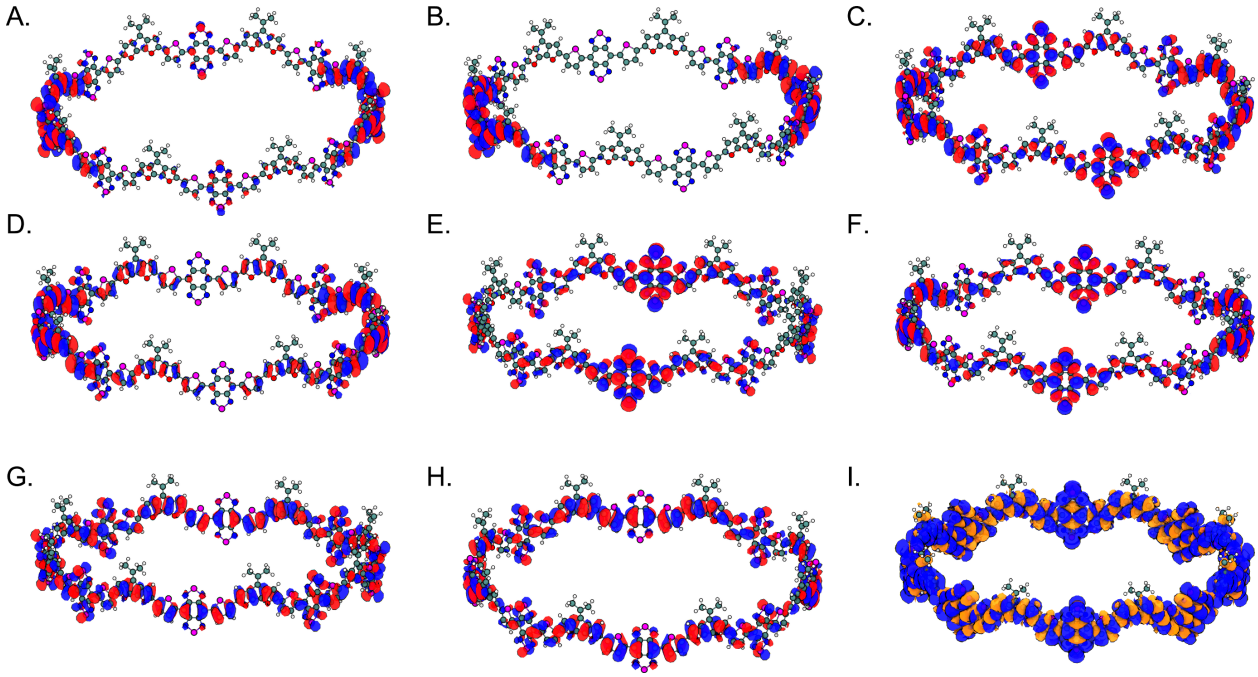

Figure S12: Related to Figure 2. Molecular orbital (MO) diagram and spin density distribution of CPDF-BBT polymer for $n = 8 - \pi$. (A) SOMO, (B) SOMO-1, (C) SOMO-2, (D) SOMO-3 (E) SOMO-4, (F) SOMO-5, (G) SOMO-6, and (H) SOMO-7 for the nonet state, (I) spin density of the nonet state.

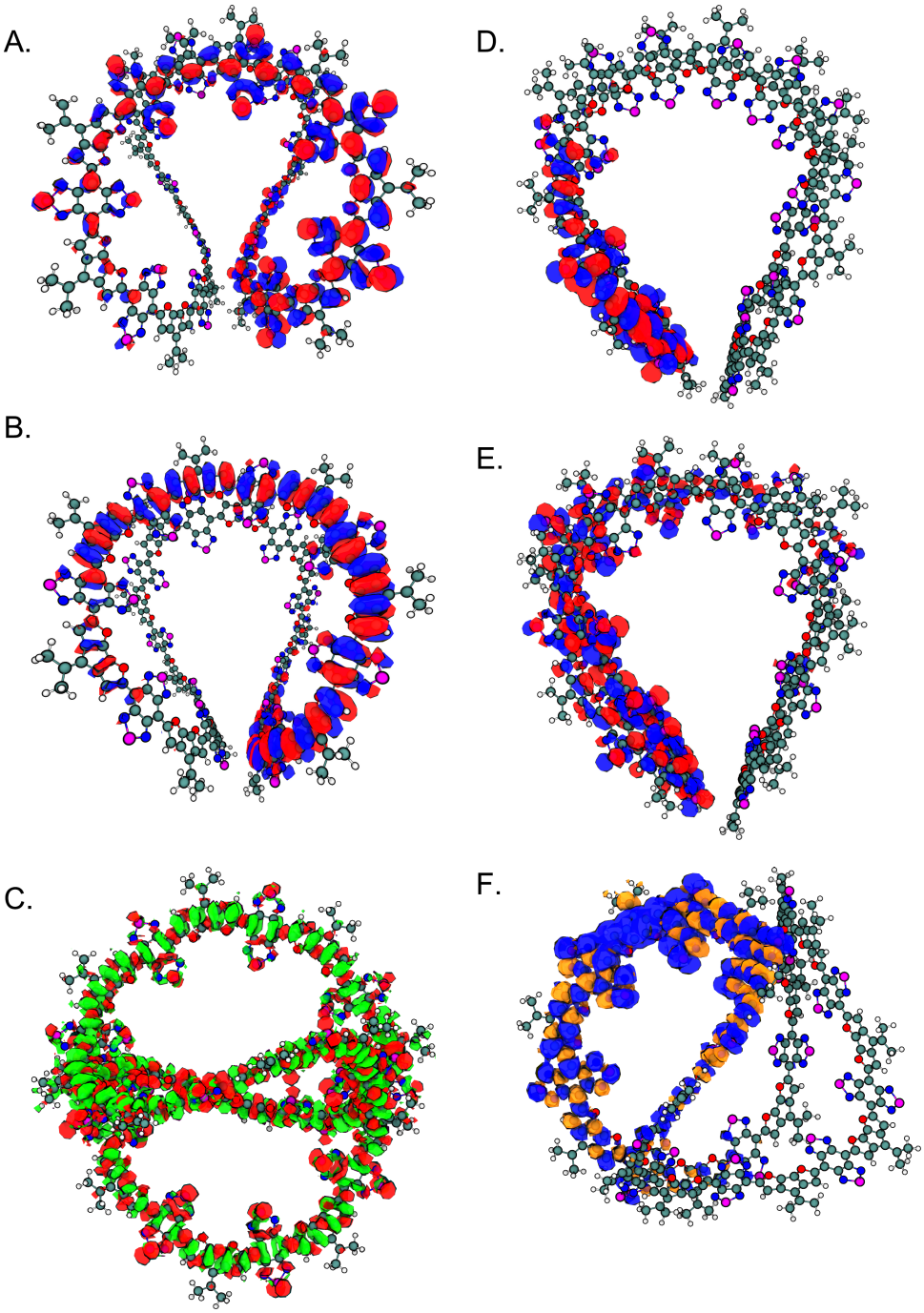

Figure S13: Related to Figure 2. Molecular orbital (MO) diagram and spin density distribution of CPDF-BBT polymer for $n = 16$. (A) HOMO and (B) LUMO for the closed-shell singlet state, (C) spin density difference ($\Delta\rho$) between the first singlet excited state and ground electronic state ($\Delta\rho = S_1 - S_0$), (D) SOMO and (E) SOMO-1 for the triplet state, (F) spin density of the triplet state.

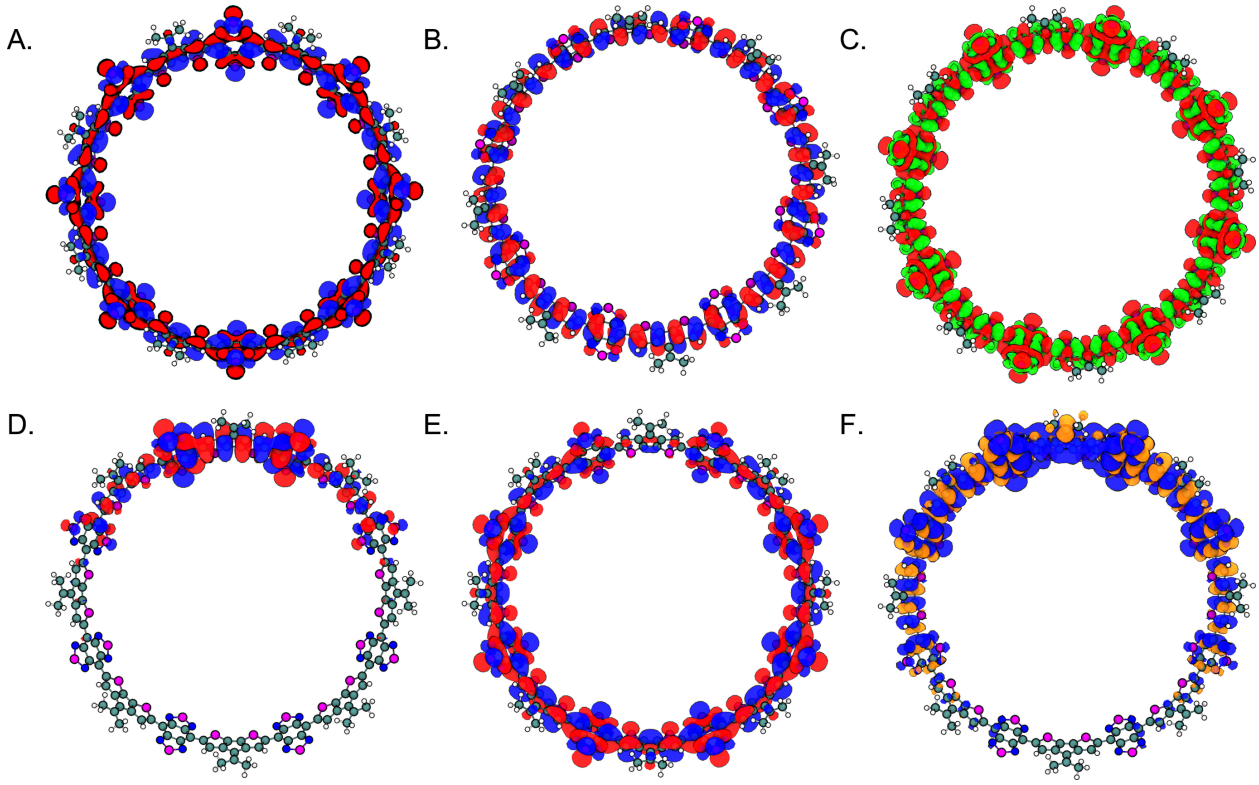

Figure S14: Related to Figure 2. Molecular orbital (MO) diagram and spin density distribution of CPDT-BBT polymer for $n = 8$. (A) HOMO and (B) LUMO for the closed-shell singlet state, (C) The spin density difference ($\Delta\rho$) between the first singlet excited and ground electronic state ($\Delta\rho = S_1 - S_0$), (D) SOMO and (E) SOMO-1 for the triplet state, (F) The spin density of the triplet state.

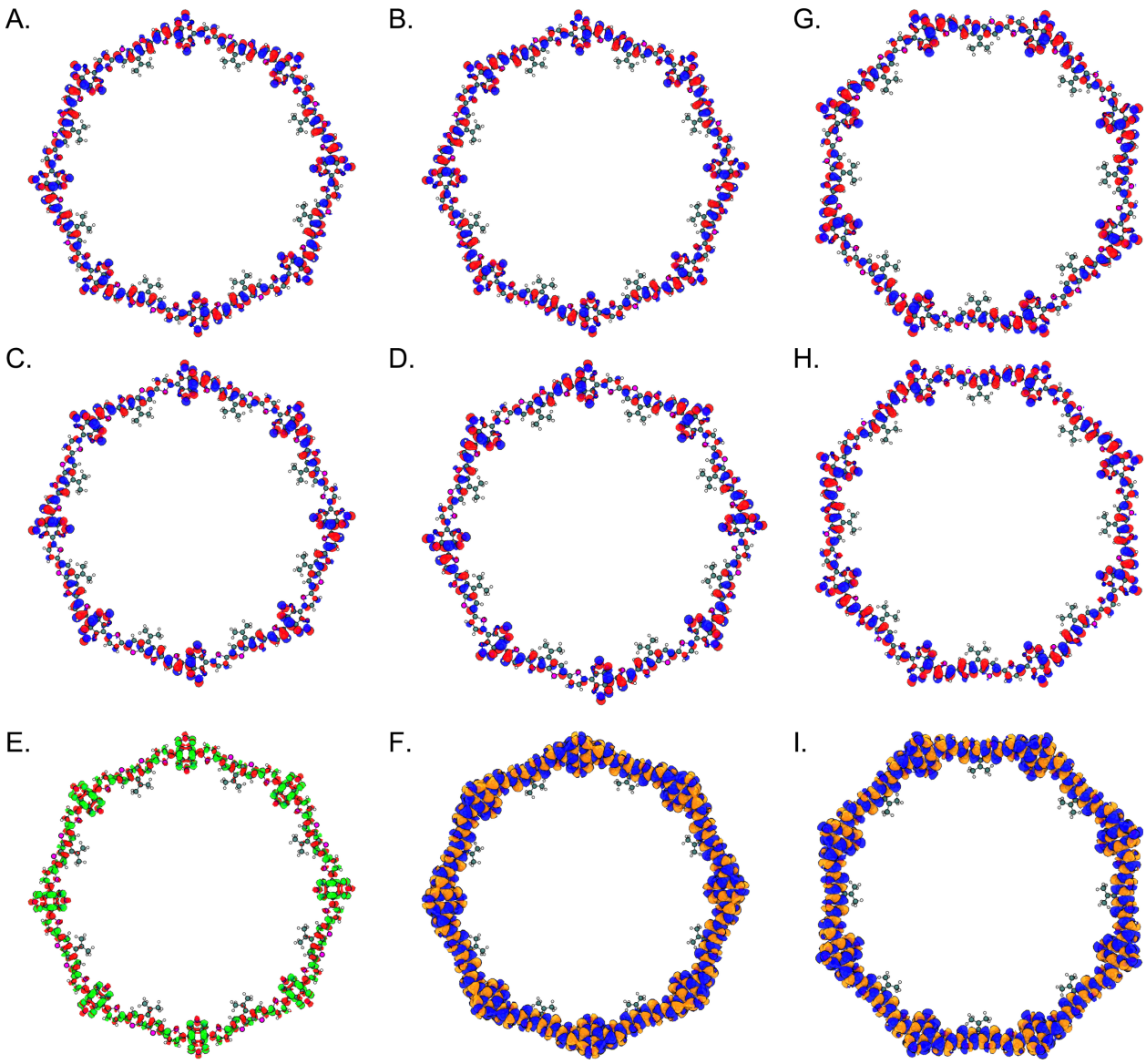

Figure S15: Related to Figure 2. Molecular orbital (MO) diagram and spin density distribution of CPDT-BBT polymer for $n = 8 - \pi$. (A) α-SOMO, (B) β-SOMO, (C) α-LUMO and (D) β-LUMO for the open-shell singlet state, (E) The spin density difference ($\Delta\rho$) between the first singlet excited and ground electronic state ($\Delta\rho = S_1 - S_0$), (G) SOMO and (H) SOMO-1 for the triplet state, (F) and (I) are spin density of the singlet and triplet state.

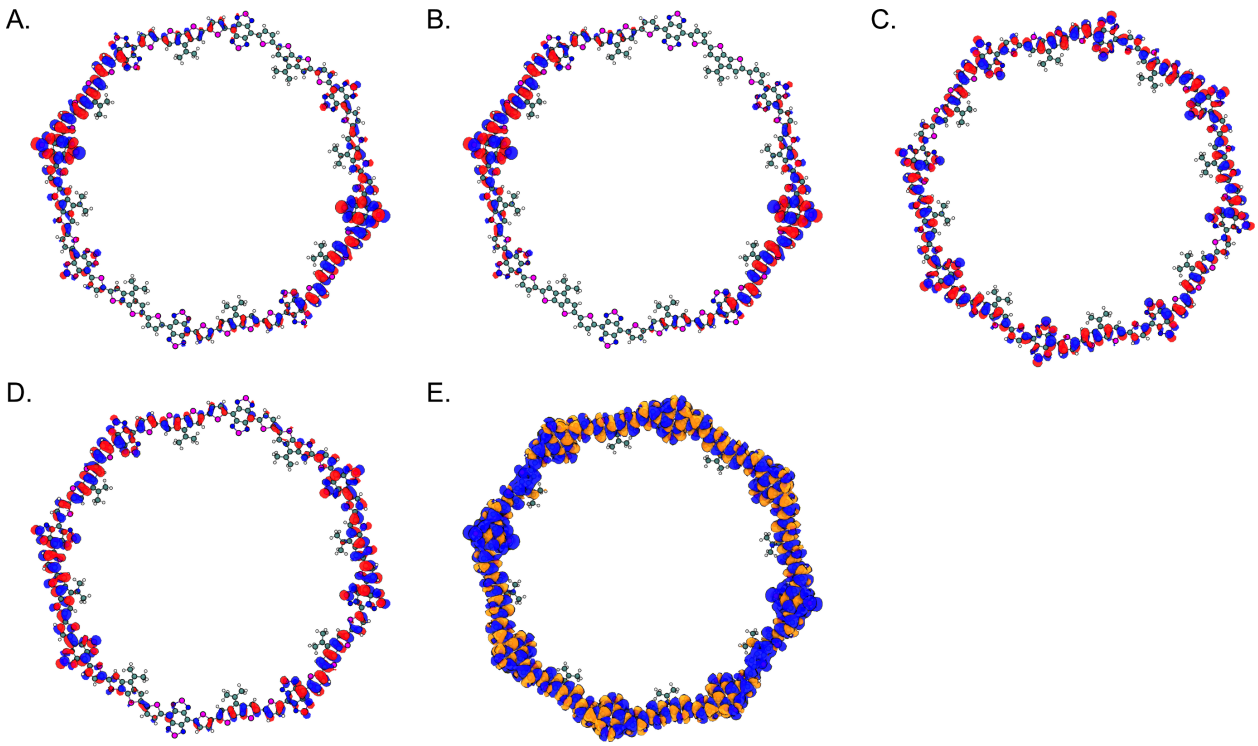

Figure S16: Related to Figure 2. Molecular orbital (MO) diagram and spin density distribution of CPDT-BBT polymer for $n = 8 - \pi$. (A) SOMO, (B) SOMO-1, (C) SOMO-2 and (D) SOMO-3 for quintet state, (E) spin density of the quintet state.

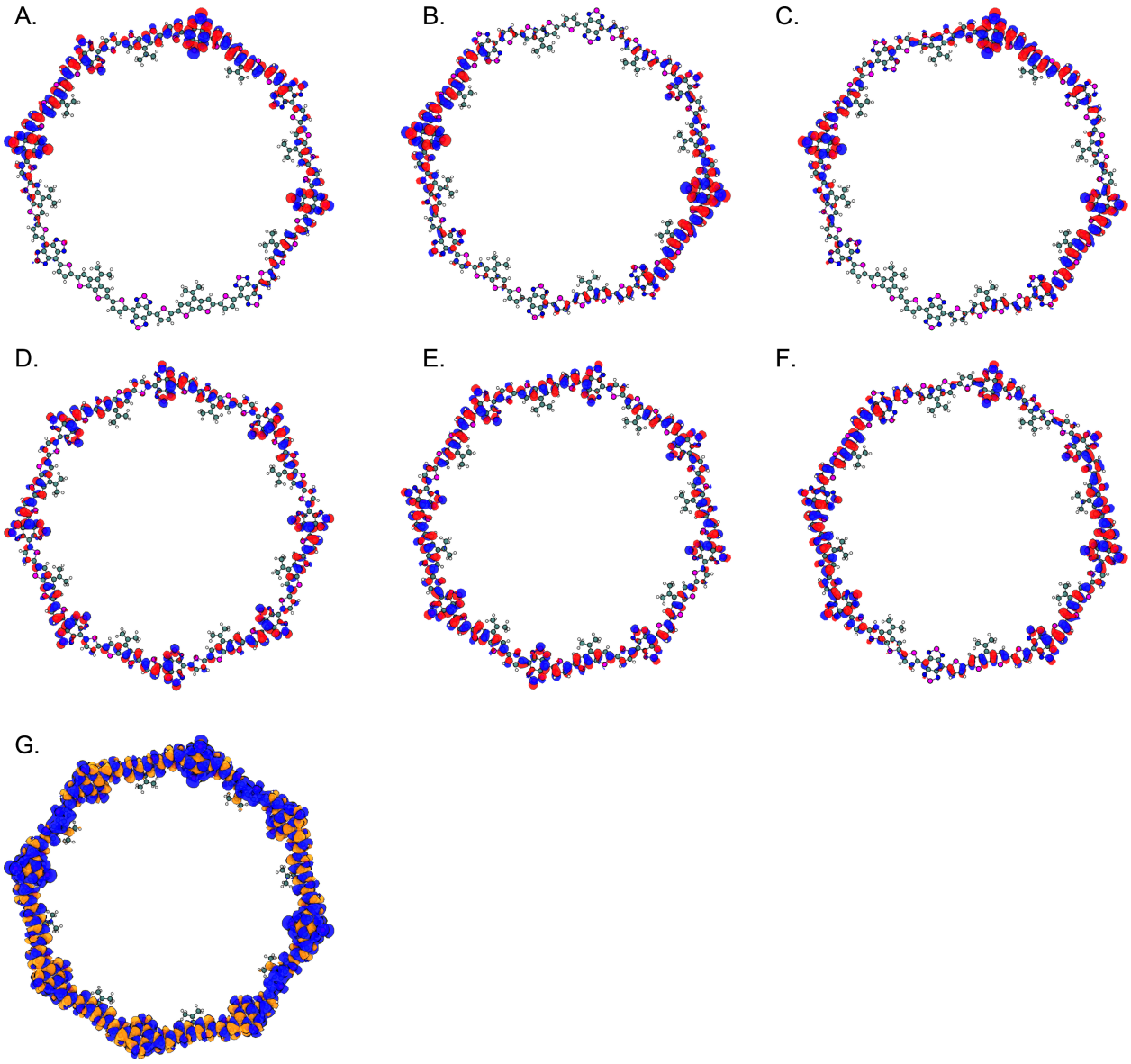

Figure S17: Related to Figure 2. Molecular orbital (MO) diagram and spin density distribution of CPDT-BBT polymer for $n = 8 - \pi$. (A) SOMO, (B) SOMO-1, (C) SOMO-2, (D) SOMO-3 (E) SOMO-4, and (F) SOMO-5 for the septet state, (G) spin density of the septet state.

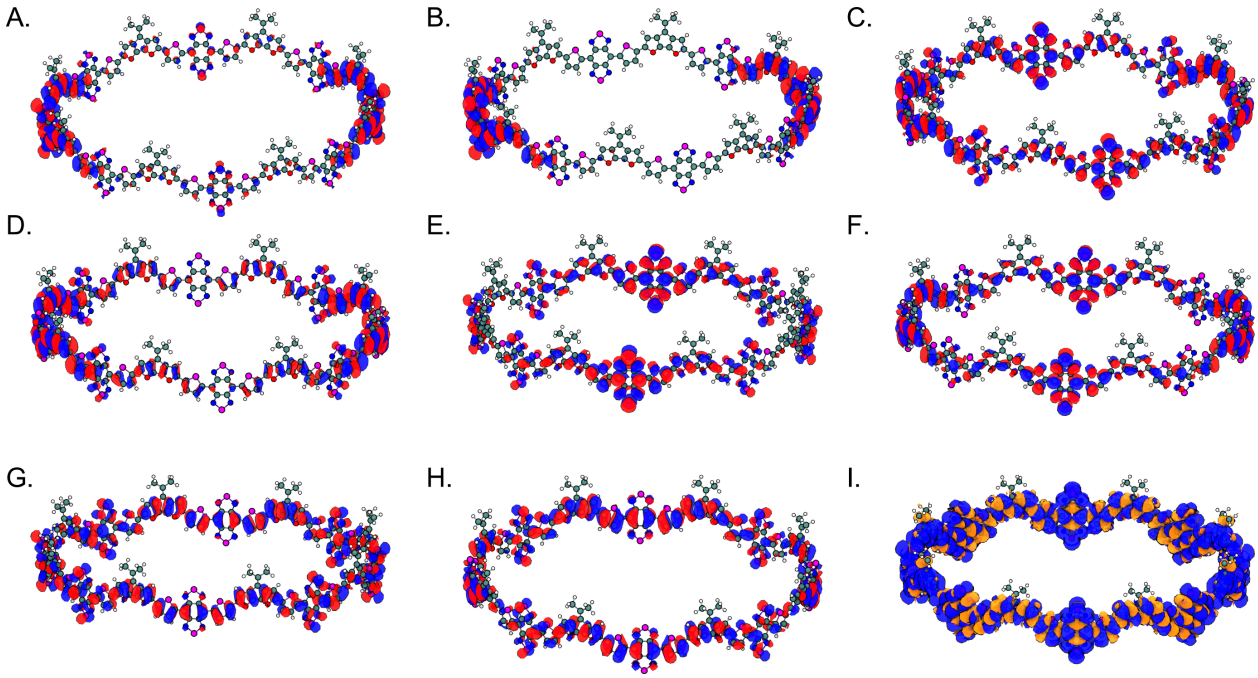

Figure S18: Related to Figure 2. Molecular orbital (MO) diagram and spin density distribution of CPDT-BBT polymer for $n = 8 - \pi$. (A) SOMO, (B) SOMO-1, (C) SOMO-2, (D) SOMO-3 (E) SOMO-4, (F) SOMO-5, (G) SOMO-6, and (H) SOMO-7 for the nonet state, (I) spin density of the nonet state.

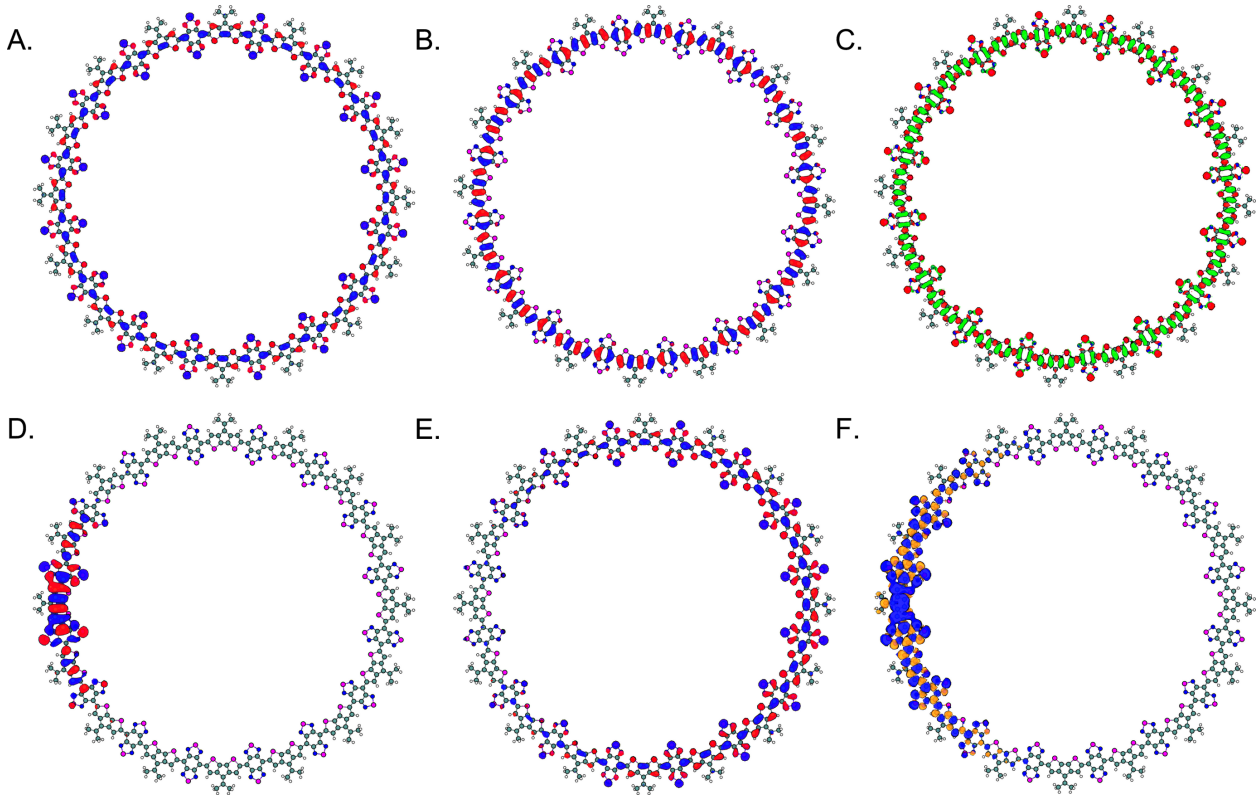

Figure S19: Related to Figure 2. Molecular orbital (MO) diagram and spin density distribution of CPDT-BBT polymer for n = 16. (A) HOMO and (B) LUMO for the closed-shell singlet state, (C) The spin density difference ($\Delta\rho$) between the first singlet excited and ground electronic state ($\Delta\rho = S_1 - S_0$), (D) SOMO and (E) SOMO-1 for the triplet state, (F) spin density of the triplet state.

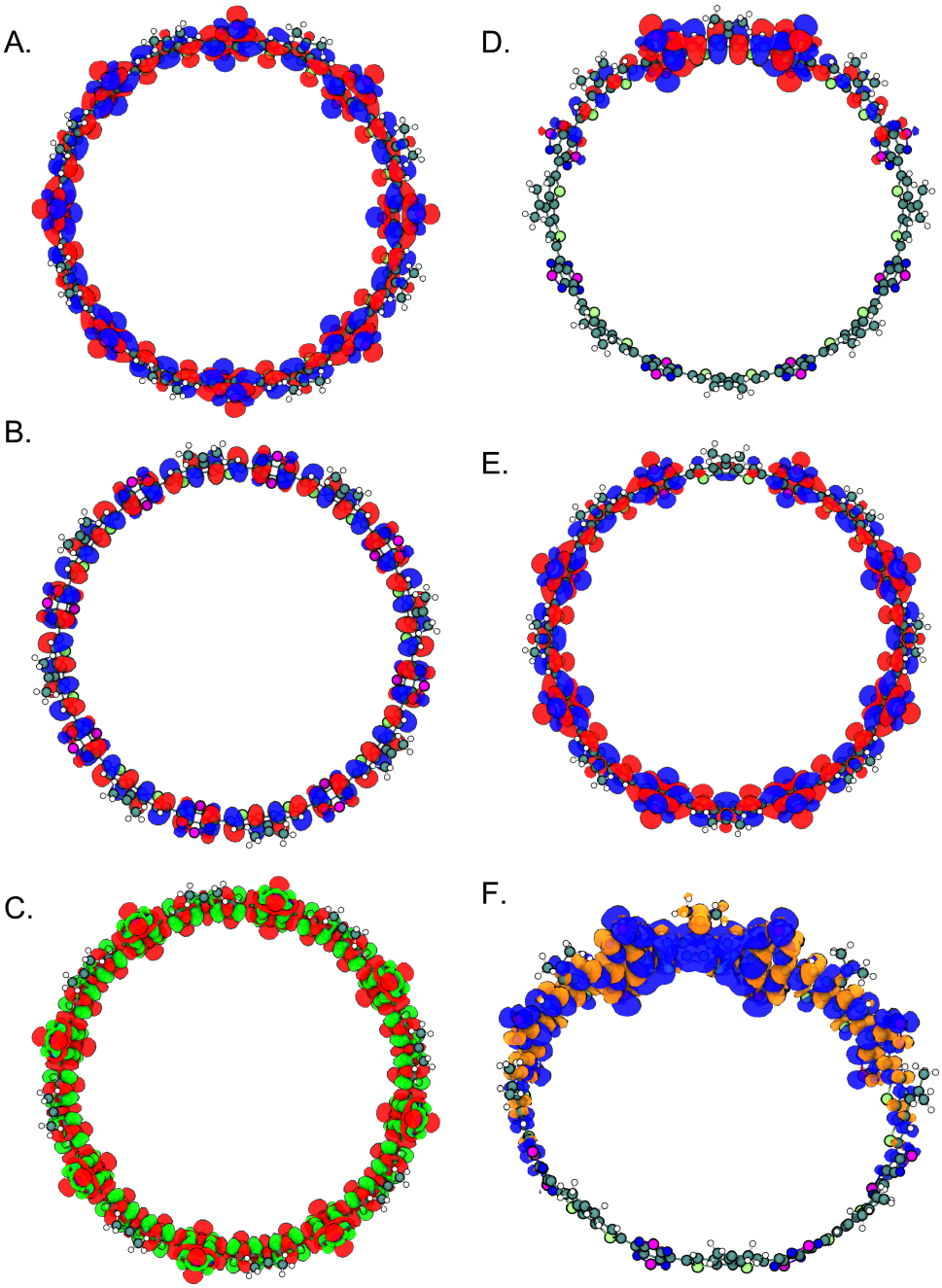

Figure S20: Related to Figure 2. Molecular orbital (MO) diagram and spin density distribution of CPDS-BBT polymer for $n = 8$. (A) HOMO and (B) LUMO for the closed-shell singlet state, (C) spin density difference ($\Delta\rho$) between the first singlet excited state and ground electronic state ($\Delta\rho = S_1 - S_0$), (D) SOMO and (E) SOMO-1 for the triplet state, (F) spin density of the triplet state.

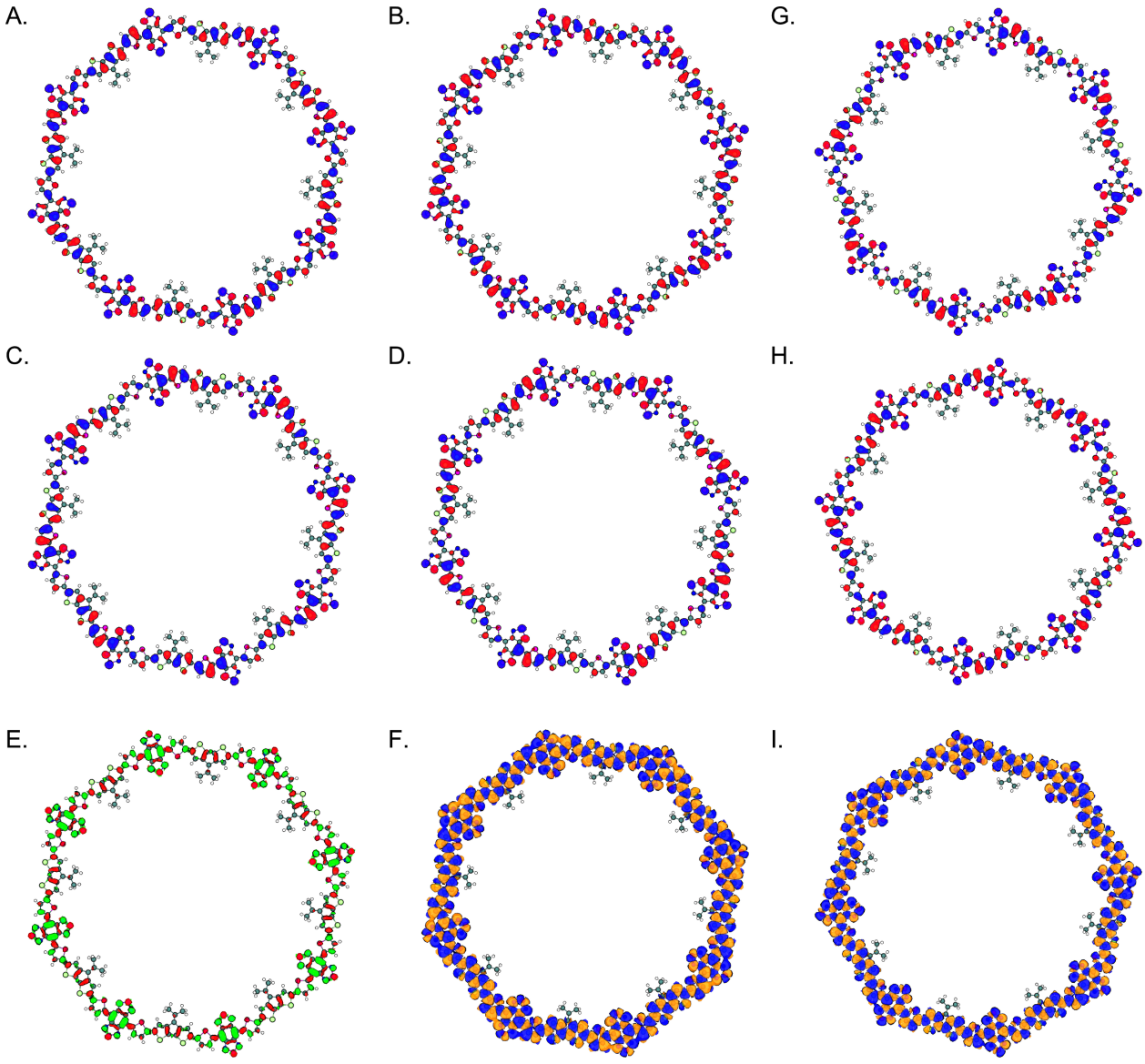

Figure S21: Related to Figure 2. Molecular orbital (MO) diagram and spin density distribution of CPDS-BBT polymer for $n = 8 - \pi$. (A) α-SOMO, (B) β-SOMO, (C) α-LUMO and (D) β-LUMO for the open-shell singlet state, (E) spin density difference ($\Delta\rho$) between the first singlet excited state and ground electronic state ($\Delta\rho = S_1 - S_0$), (G) SOMO and (H) SOMO-1 for the triplet state, (F) and (I) are spin density of the singlet and triplet state.

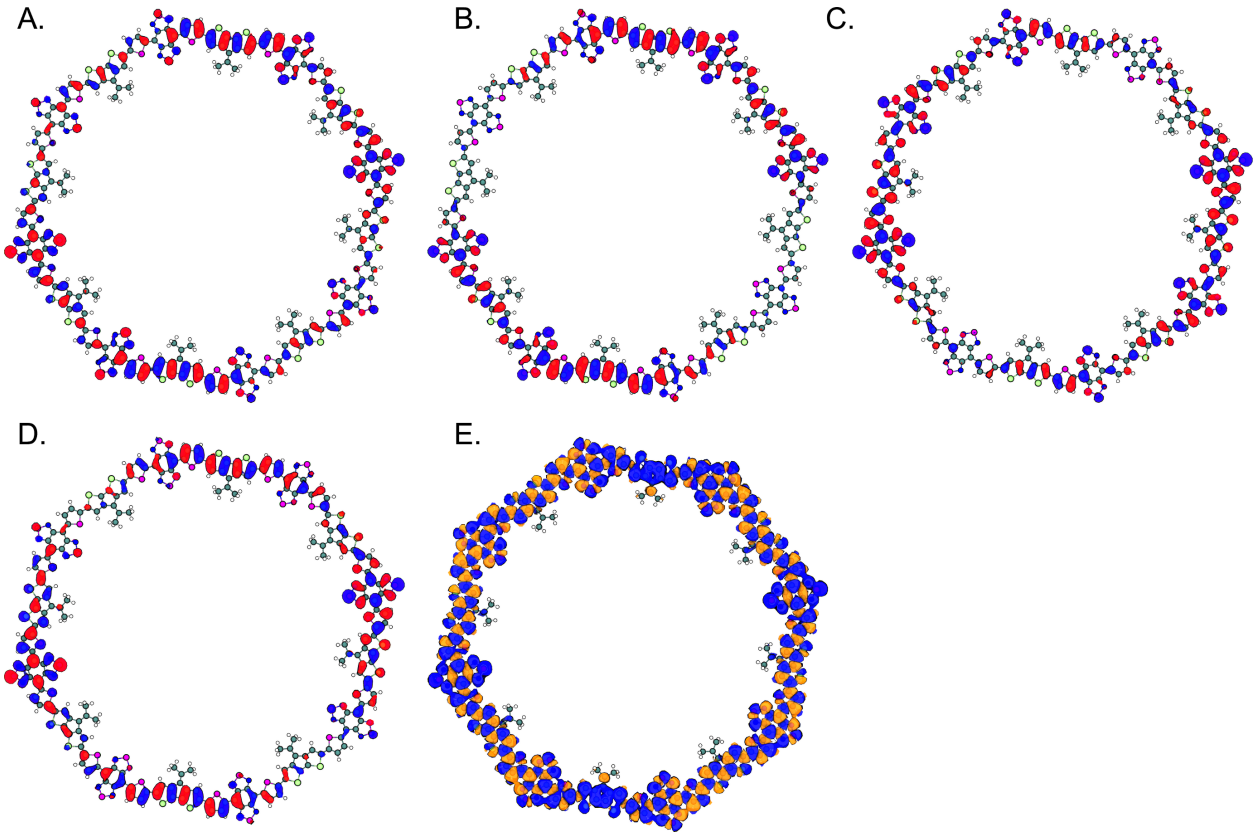

Figure S22: Related to Figure 2. Molecular orbital (MO) diagram and spin density distribution of CPDS-BBT polymer for $n = 8 - \pi$. (A) SOMO, (B) SOMO-1, (C) SOMO-2 and (D) SOMO-3 for quintet state, (E) spin density of the quintet state.

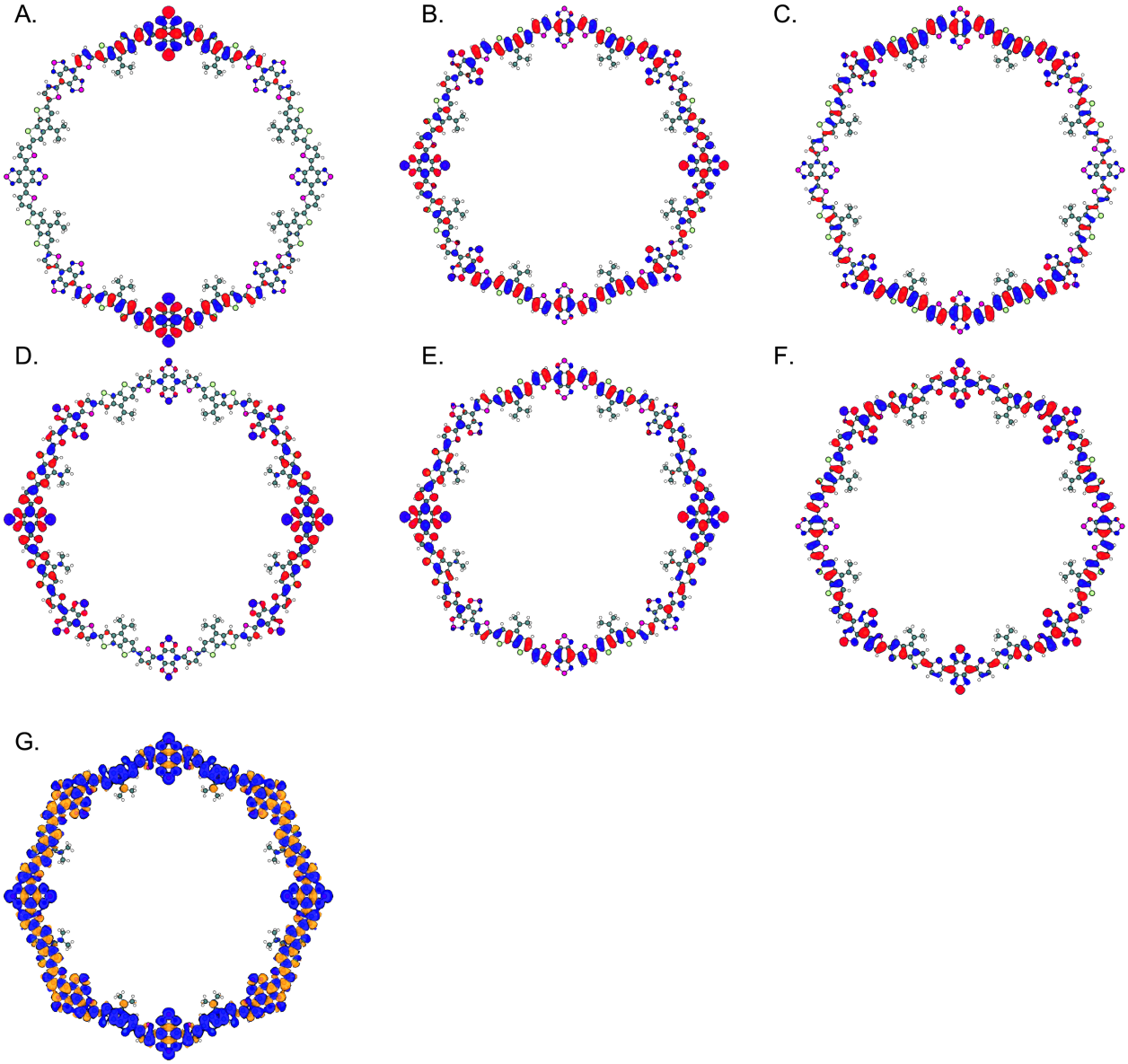

Figure S23: Related to Figure 2. Molecular orbital (MO) diagram and spin density distribution of CPDS-BBT polymer for $n = 8 - \pi$. (A) SOMO, (B) SOMO-1, (C) SOMO-2, (D) SOMO-3 (E) SOMO-4, and (F) SOMO-5 for the septet state, (G) spin density of the septet state.

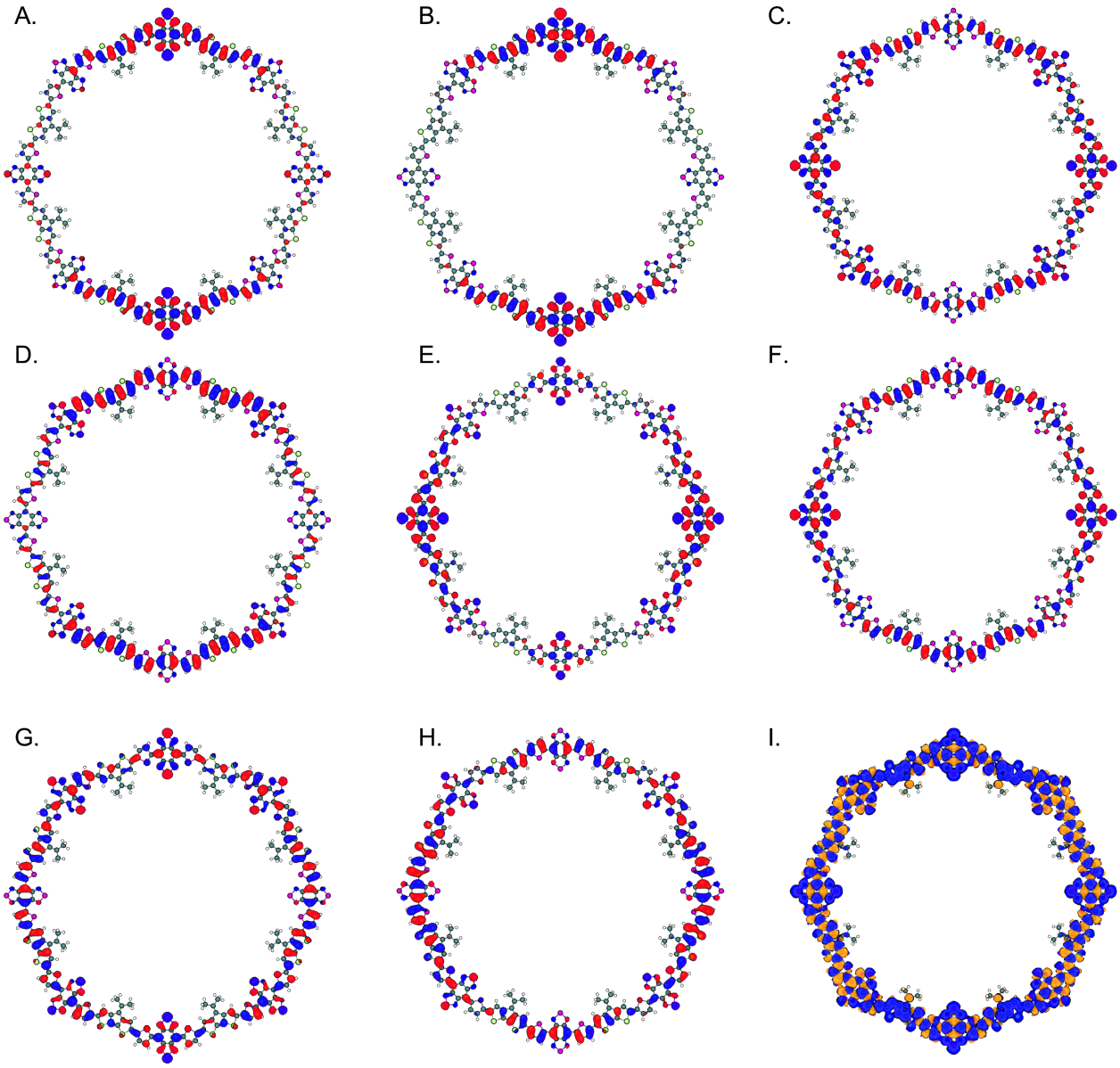

Figure S24: Related to Figure 2. Molecular orbital (MO) diagram and spin density distribution of CPDS-BBT polymer for $n = 8 - \pi$. (A) SOMO, (B) SOMO-1, (C) SOMO-2, (D) SOMO-3 (E) SOMO-4, (F) SOMO-5, (G) SOMO-6, and (H) SOMO-7 for the nonet state, (I) spin density of the nonet state.

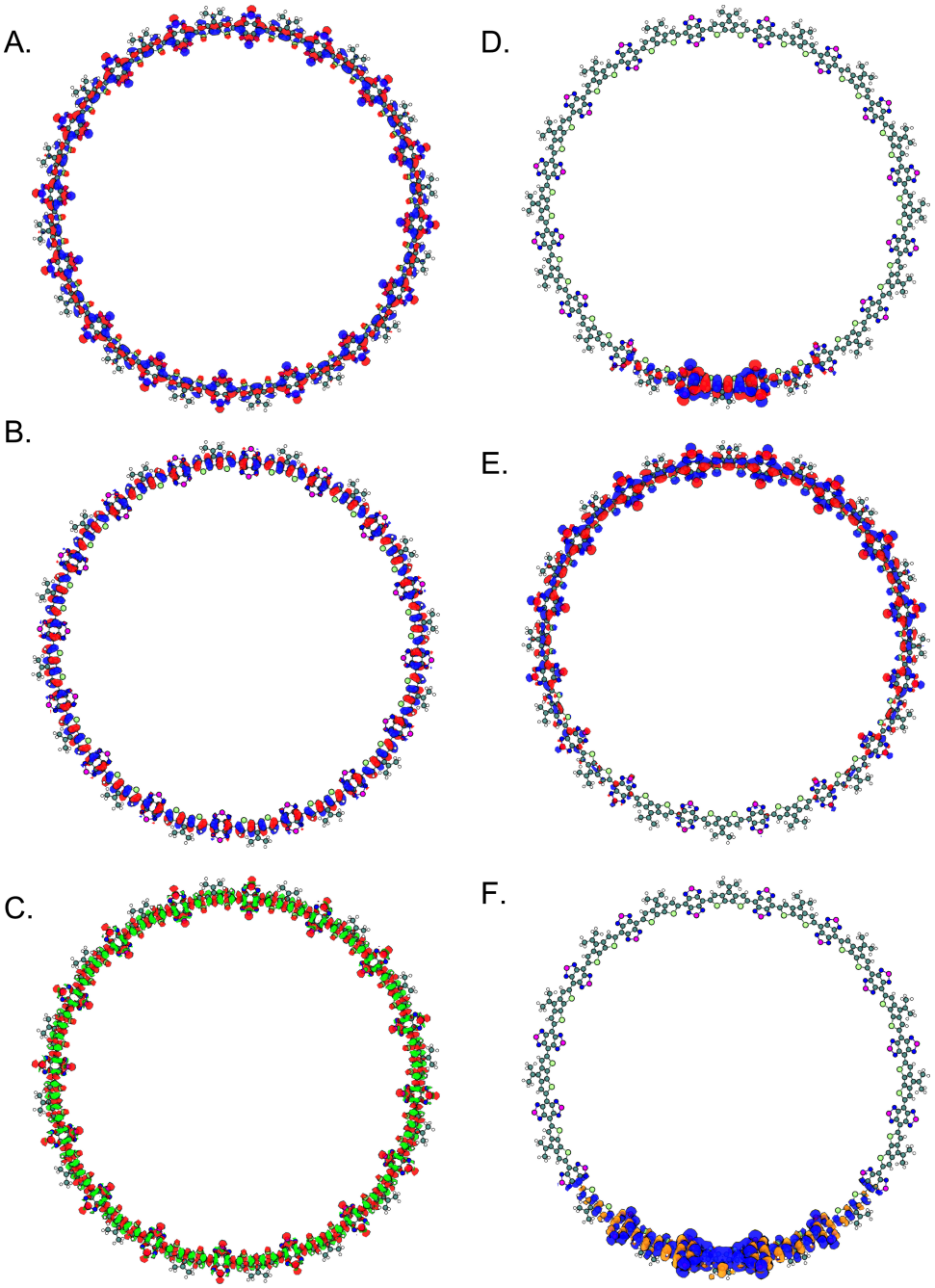

Figure S25: Related to Figure 2. Molecular orbital (MO) diagram and spin density distribution of CPDS-BBT polymer for $n = 16$. (A) HOMO and (B) LUMO for the closed-shell singlet state, (C) spin density difference ($\Delta\rho$) between the first singlet excited state and ground electronic state ($\Delta\rho = S_1 - S_0$), (D) SOMO and (E) SOMO-1 for the triplet state, (F) spin density of the triplet state.

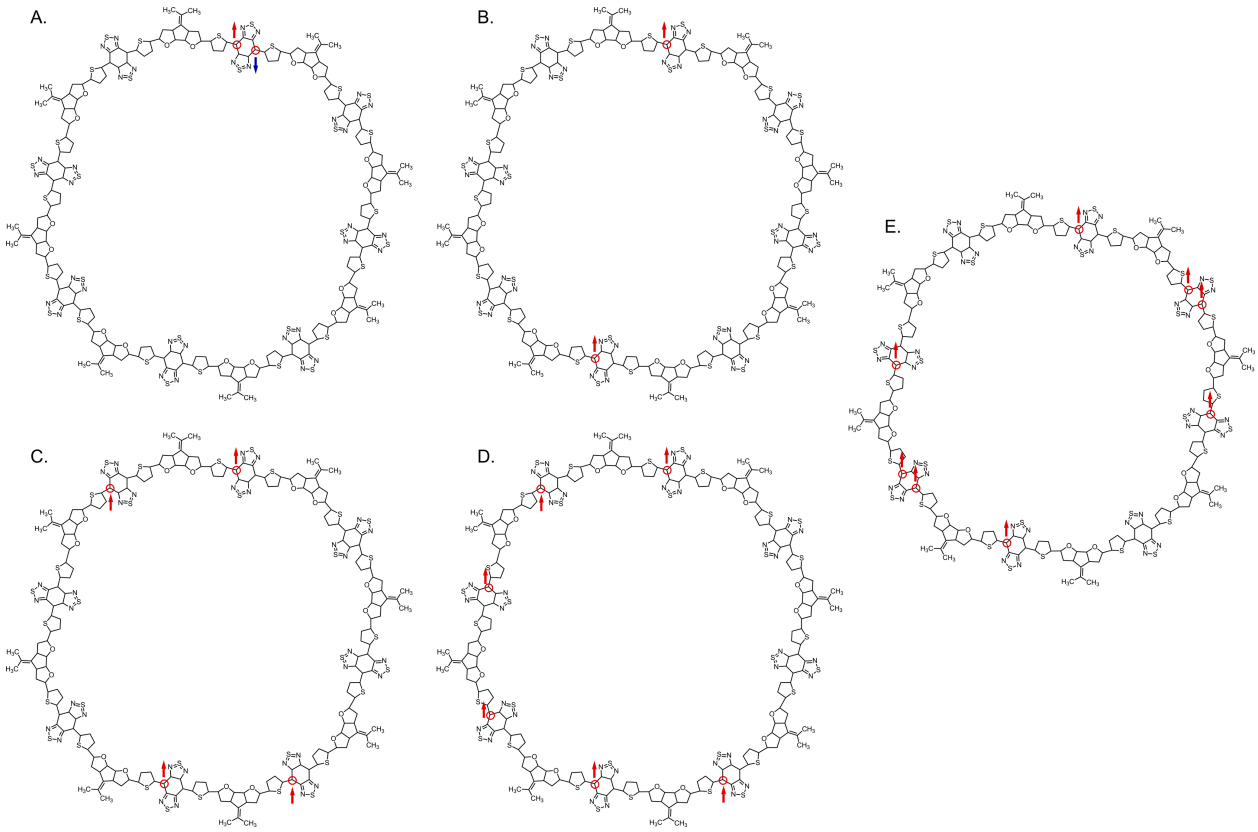

Figure S26: Related to Figure 4. The unpaired spins locations of CPDF-BBT on the macrocycle backbone for $n = 8 - \pi$. (A) singlet, (B) triplet, (C) quintet, (D) septet, and (E) nonet state.

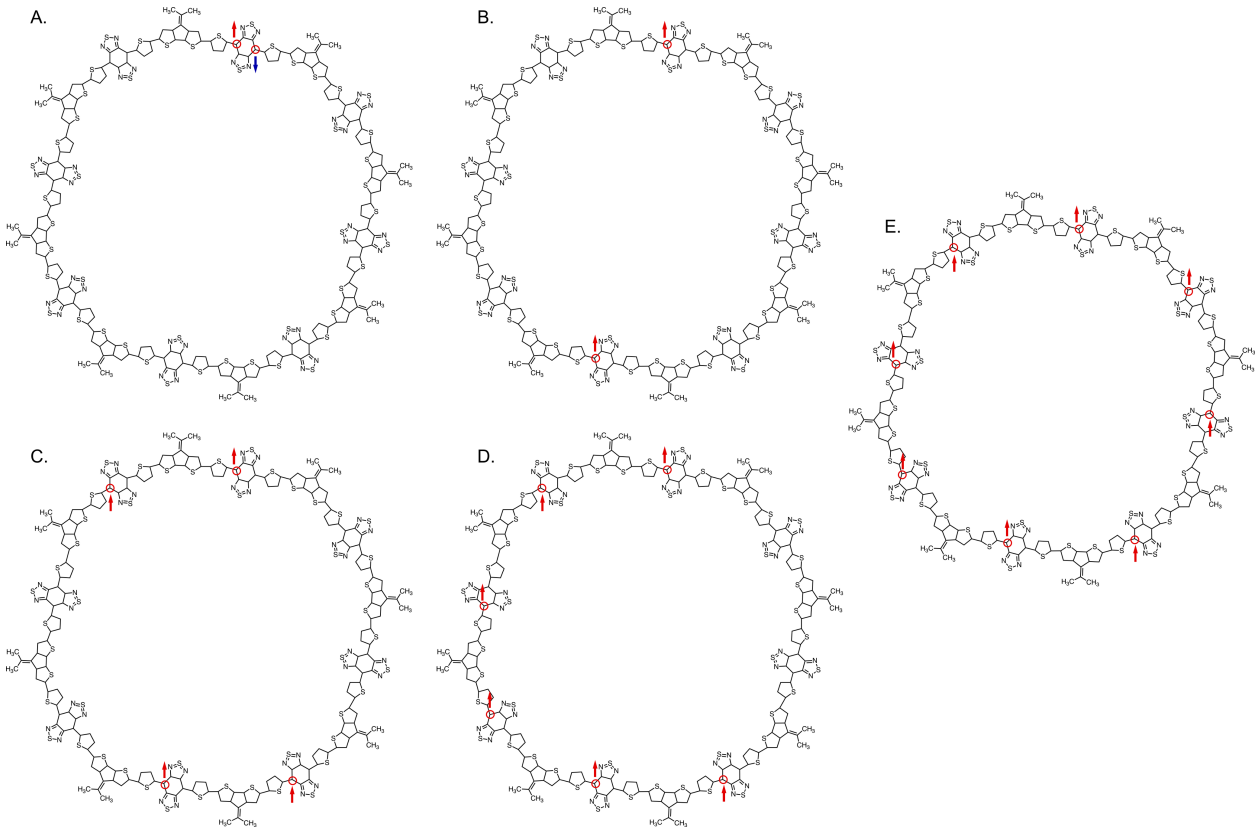

Figure S27: Related to Figure 4. The unpaired spins locations of CPDT-BBT on the macrocycle backbone for $n = 8 - \pi$. (A) singlet, (B) triplet, (C) quintet, (D) septet, and (E) nonet state.

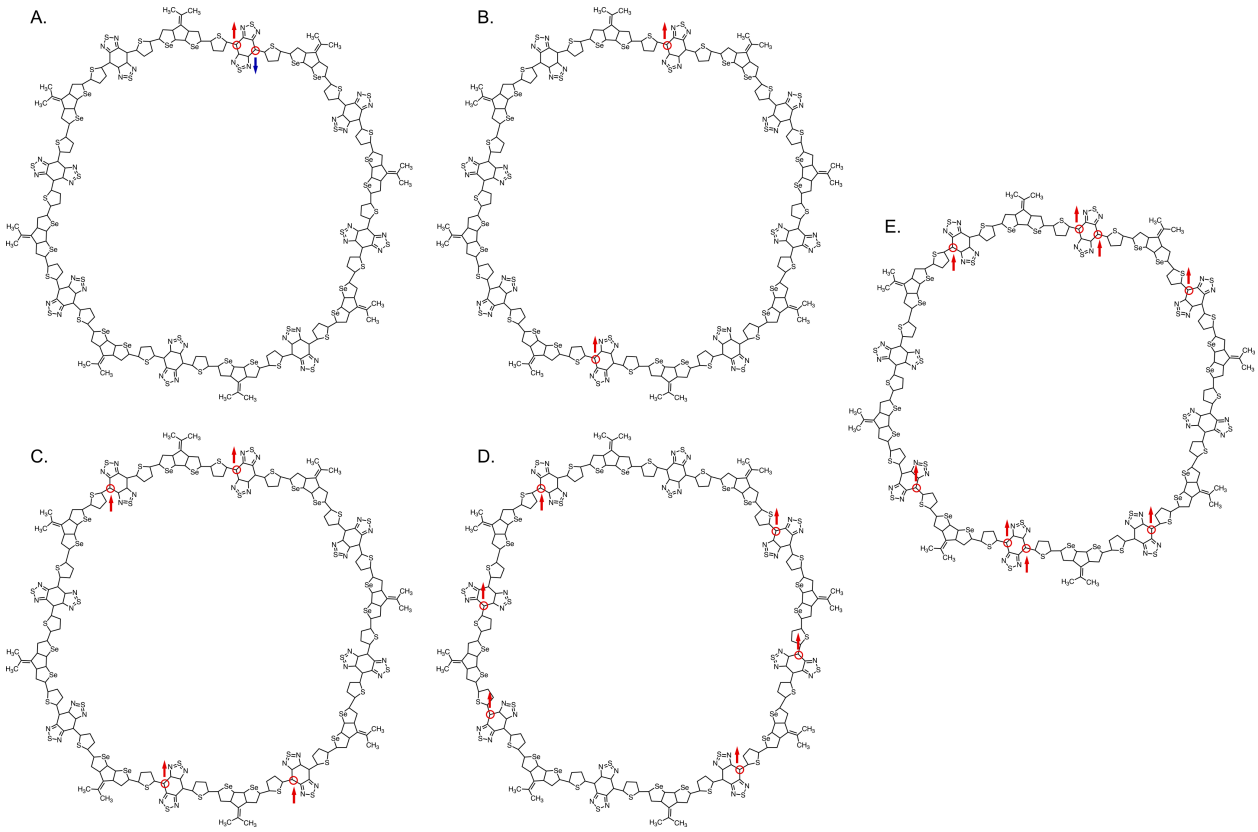

Figure S28: Related to Figure 4. The unpaired spins locations of CPDS-BBT on the macrocycle backbone for $n = 8 - \pi$. (A) singlet, (B) triplet, (C) quintet, (D) septet, and (E) nonet state.

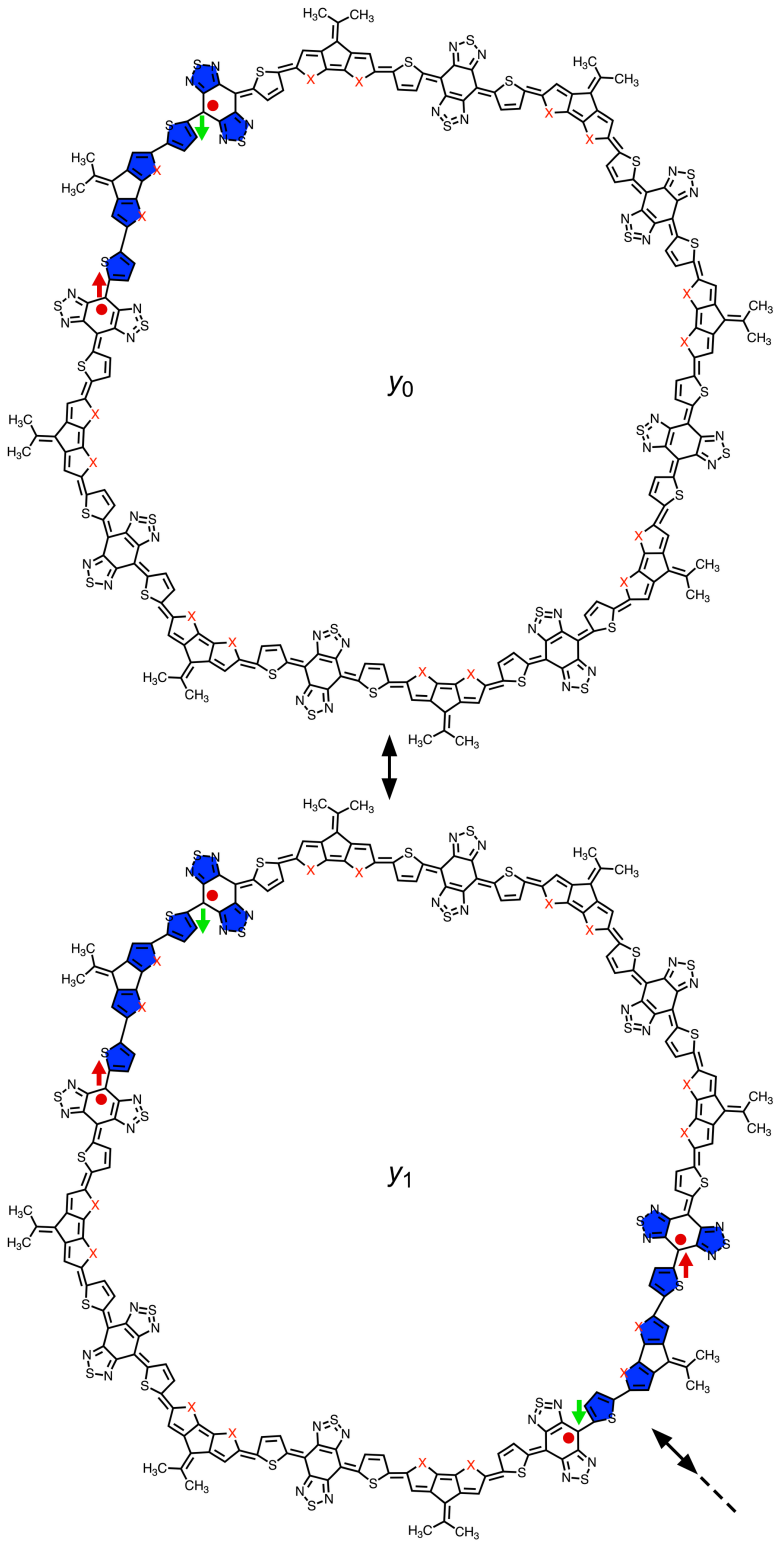

Figure S29: Related to Figure 4. Resonance structures of the CPDF-(X = O), CPDT-(X = S), and CPDS-BBT (X = Se) macromolecules with $n = 8 - \pi$ repeat units.

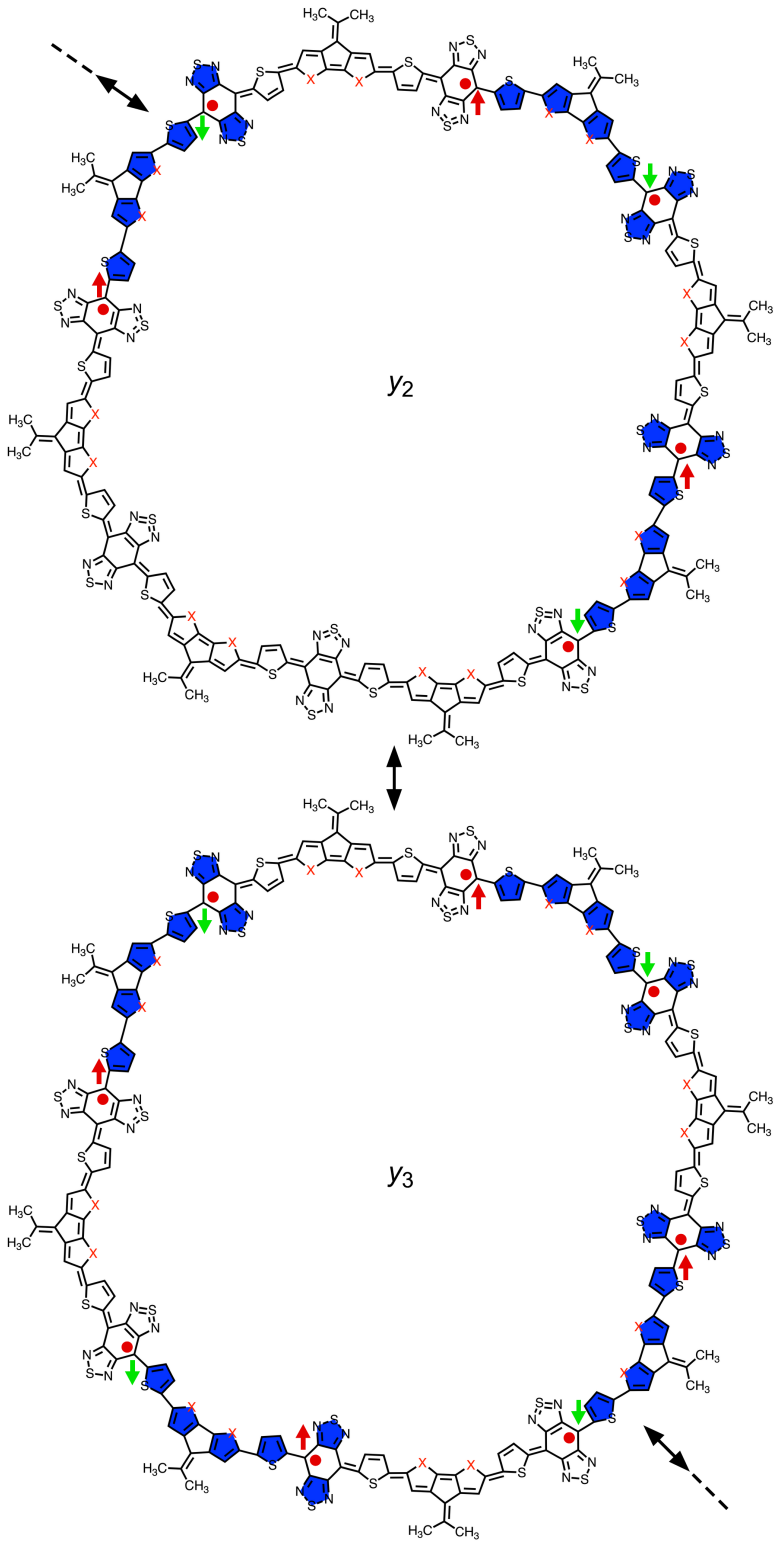

Figure S30: Related to Figure 4. Resonance structures of the CPDF-(X = O), CPDT-(X = S), and CPDS-BBT (X = Se) macromolecules with $n = 8 - \pi$ repeat units.

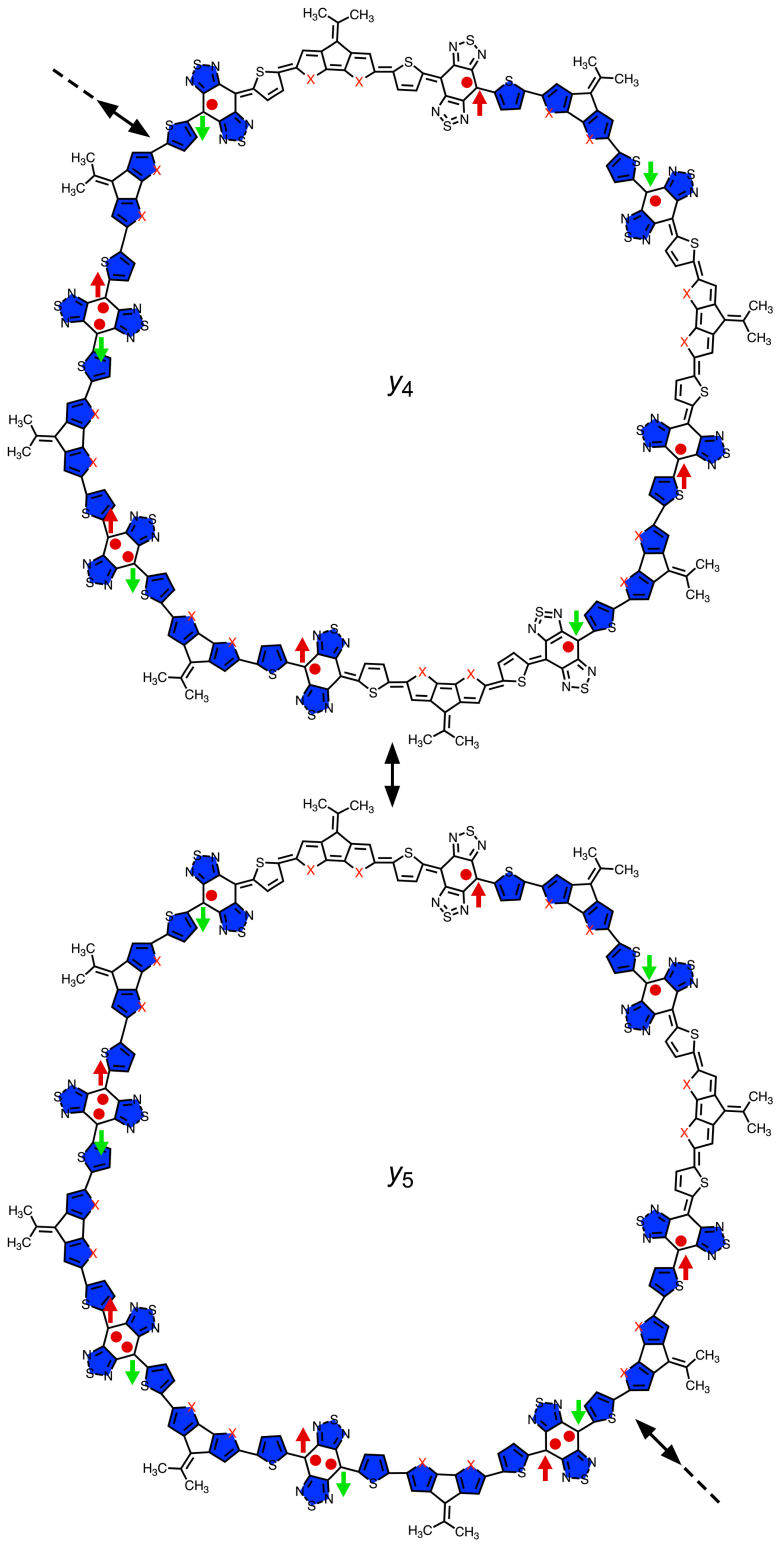

Figure S31: Related to Figure 4. Resonance structures of the CPDF-(X = O), CPDT-(X = S), and CPDS-BBT (X = Se) macromolecules with $n = 8 - \pi$ repeat units.

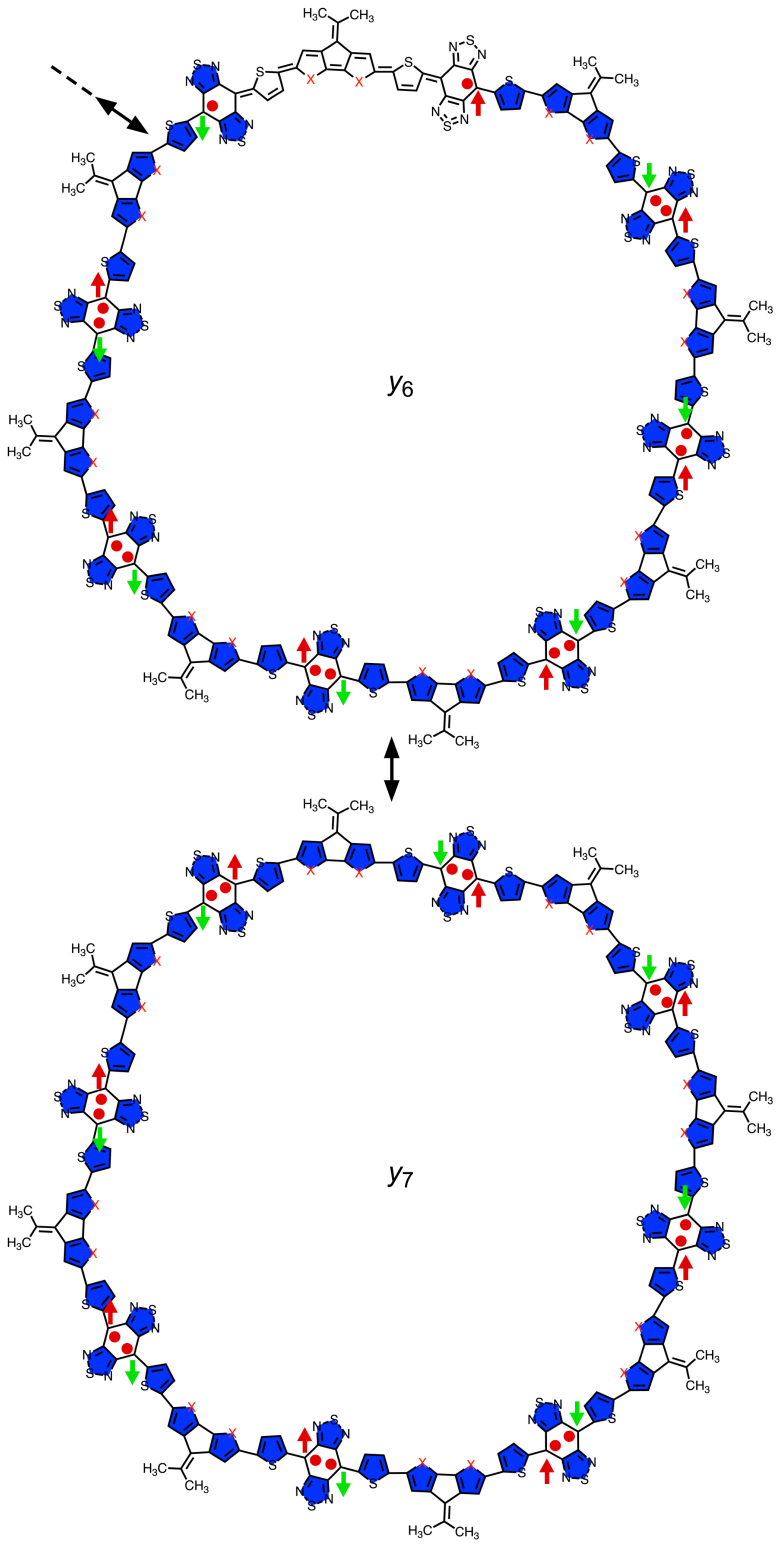

Figure S32: Related to Figure 4. Resonance structures of the CPDF-(X = O), CPDT-(X = S), and CPDS-BBT (X = Se) macromolecules with $n = 8 - \pi$ repeat units.

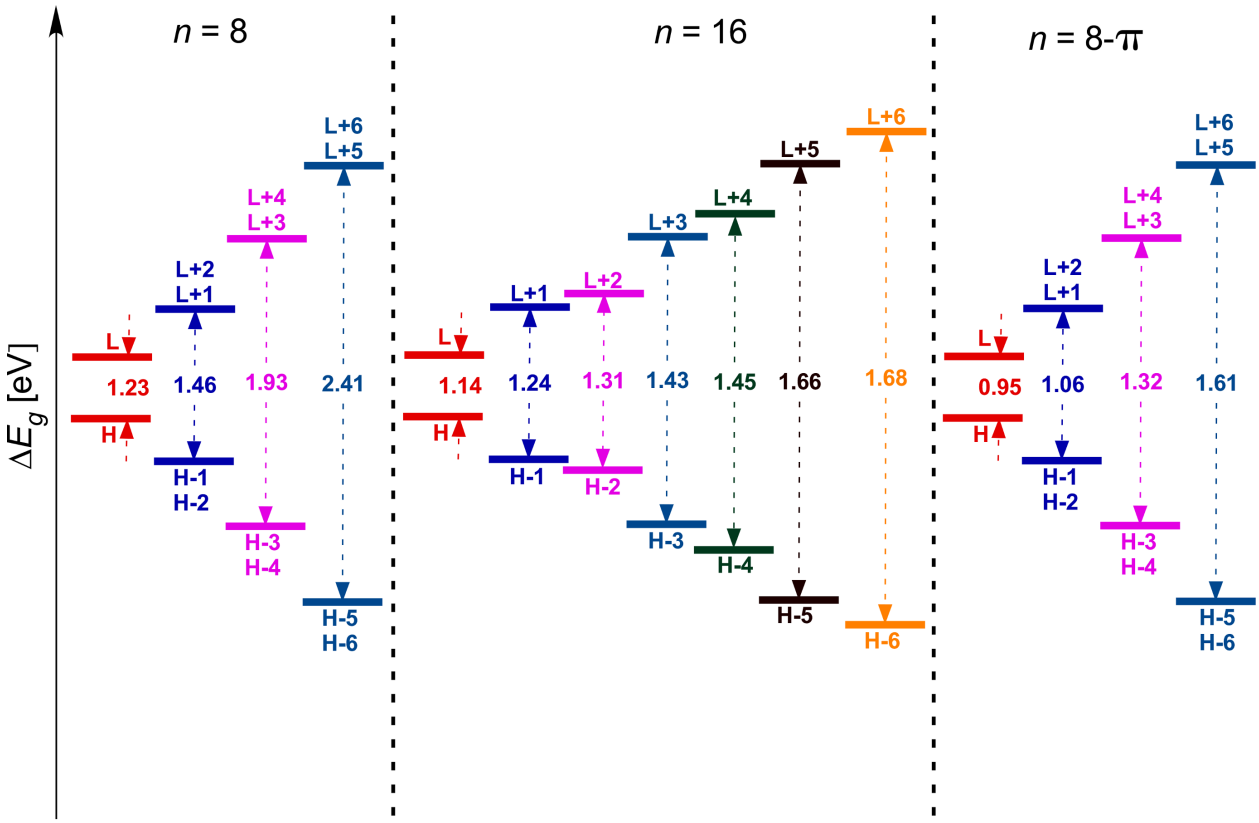

Figure S33: Related to Table 1. Energy diagram of the frontier and higher degenerate MOs for CPDF-BBT polymer obtained as a function of chain length.

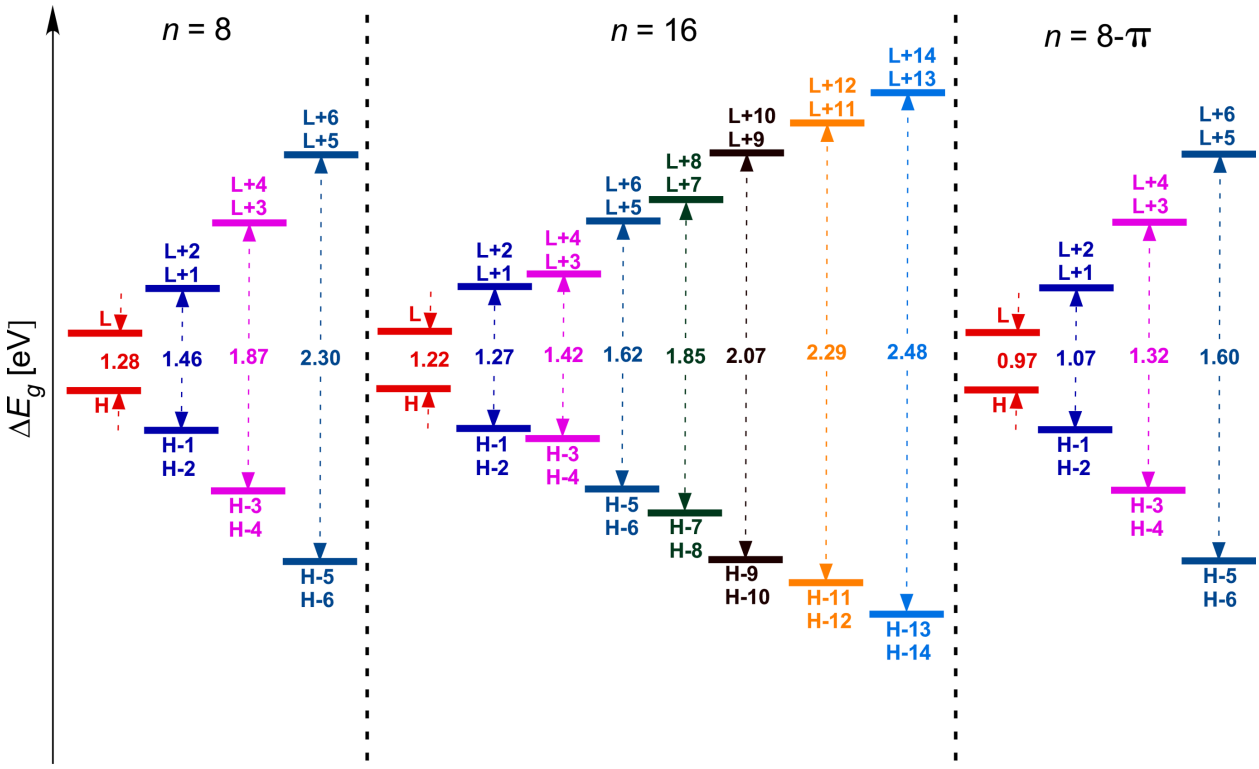

Figure S34: Related to Table 1. Energy diagram of the frontier and higher degenerate MOs for CPDT-BBT polymer obtained as a function of chain length.

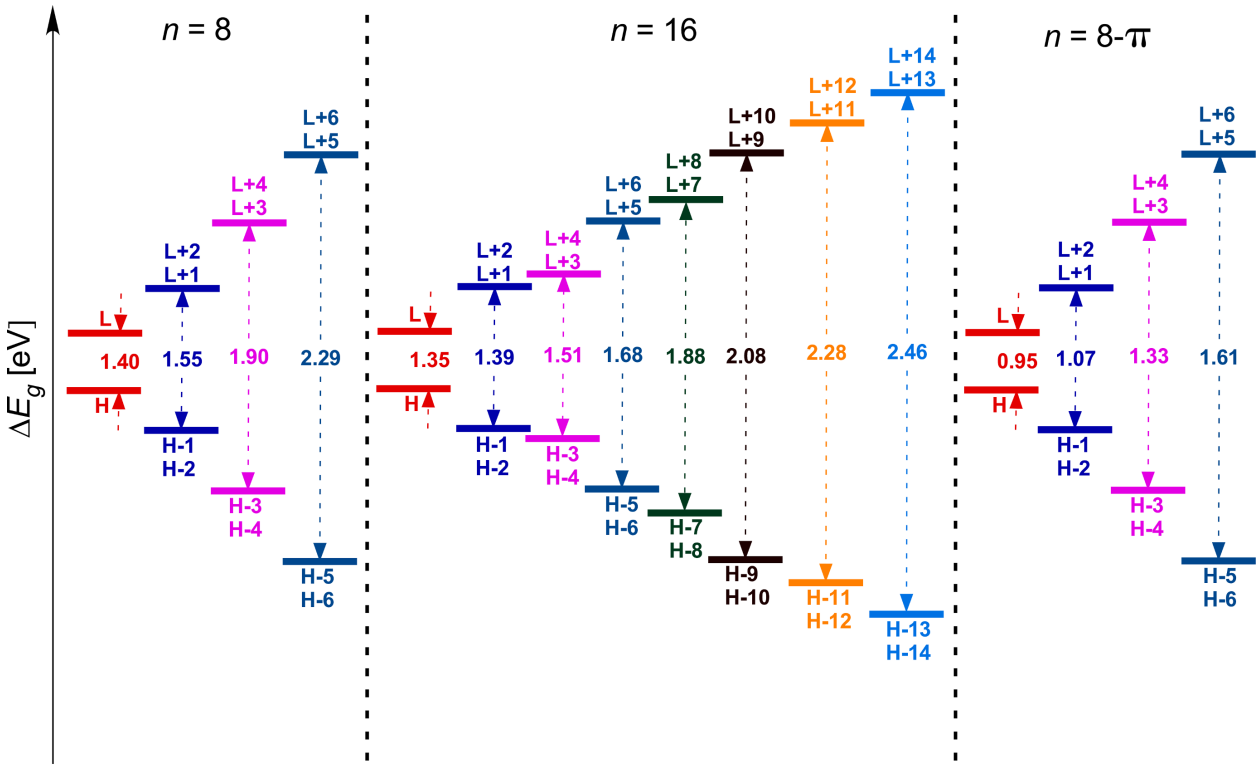

Figure S35: Related to Table 1. Energy diagram of the frontier and higher degenerate MOs for CPDS-BBT polymer obtained as a function of chain length.

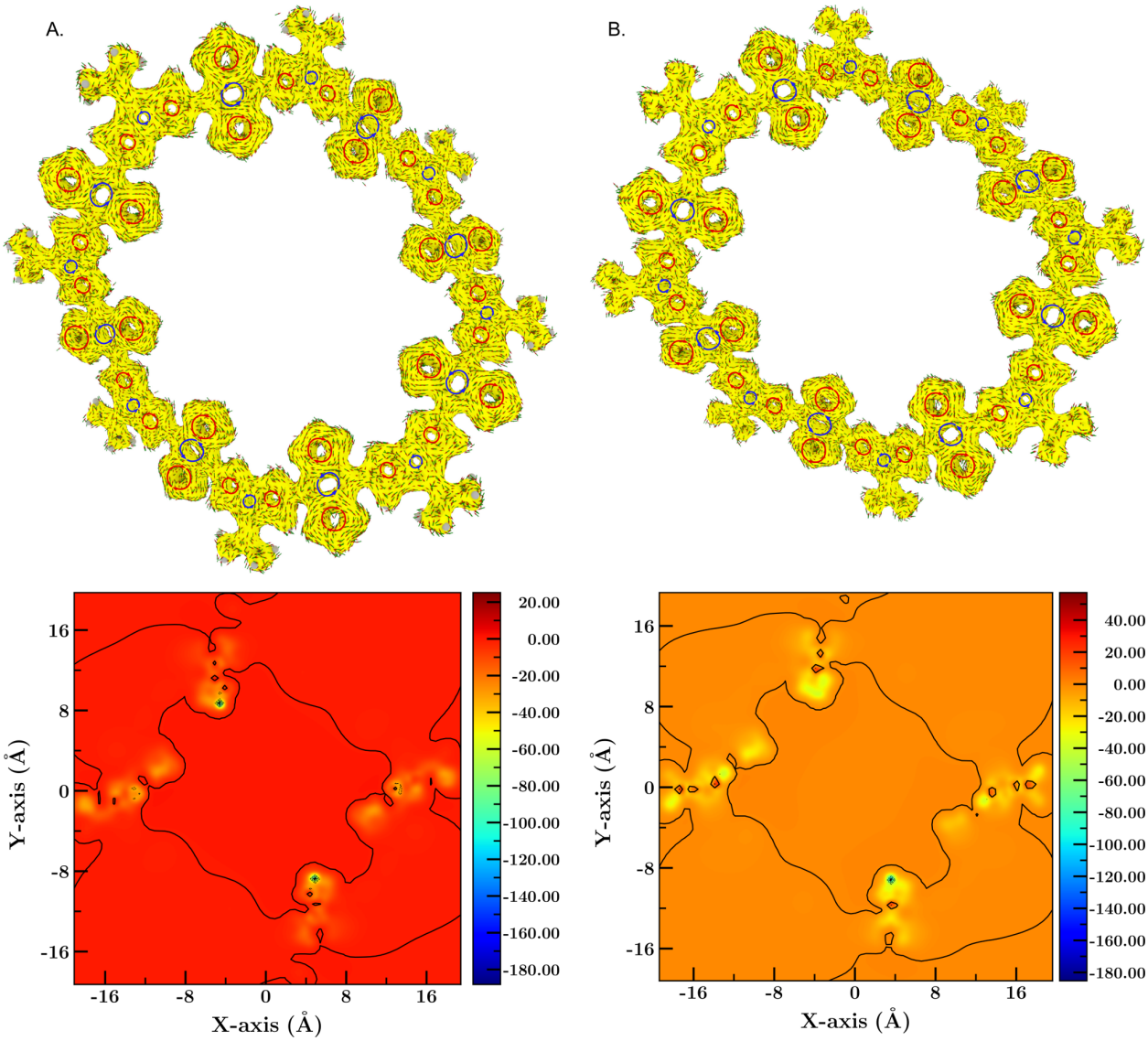

Figure S36: Related to Figure 5. AICD plots (top) and 2D-ICSS (bottom) maps for CPDF-BBT in the (A) singlet and (B) triplet states, respectively, at $n = 8$.

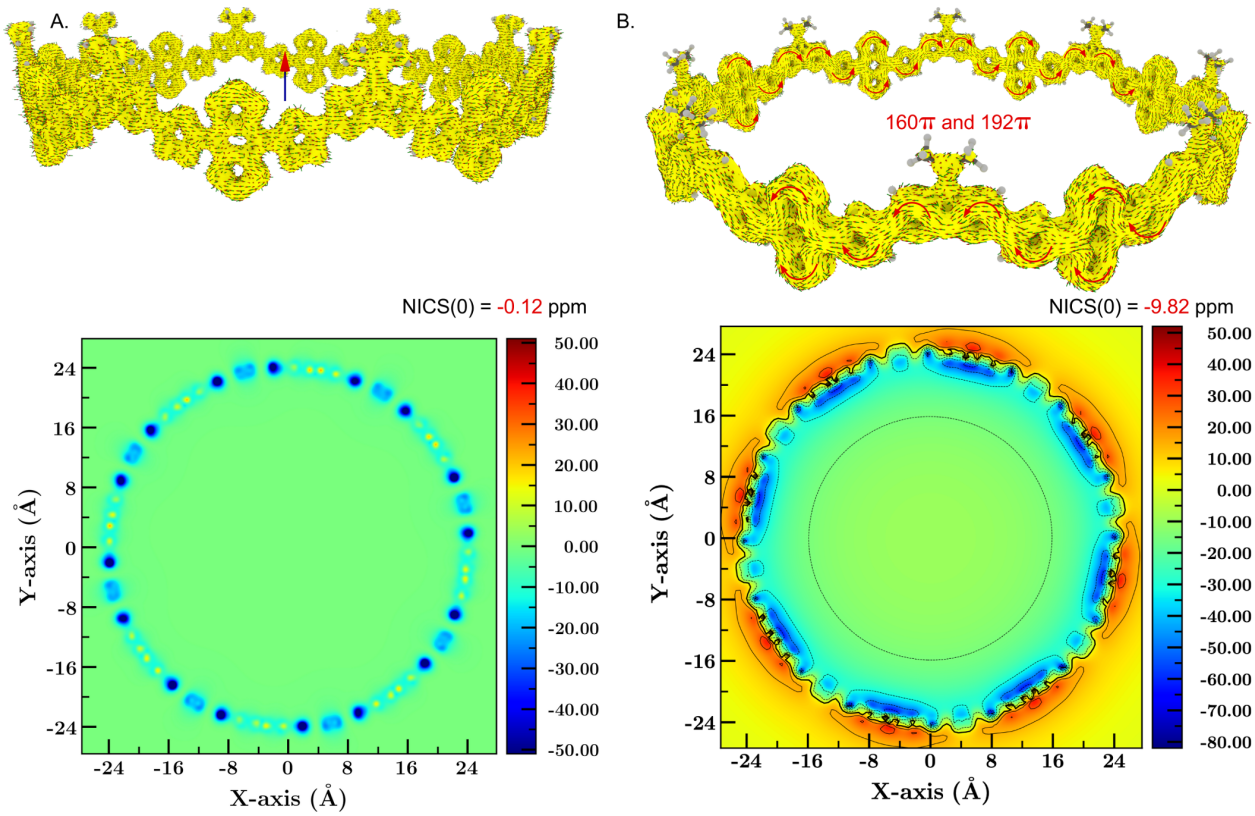

Figure S37: Related to Figure 5. AICD plots (top) and 2D-ICSS (bottom) maps for CPDF-BBT in the (A) singlet and (B) triplet states, respectively, at $n = 8 - \pi$.

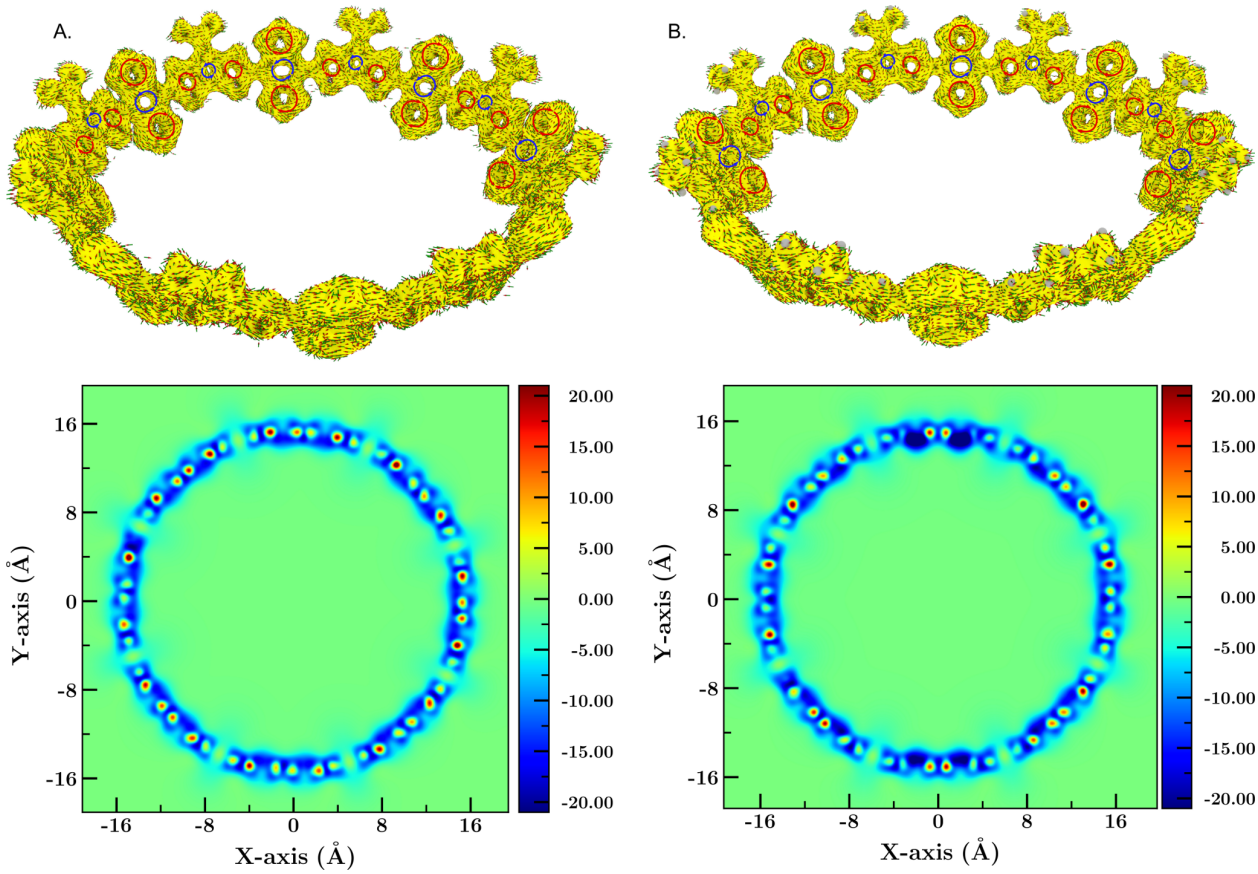

Figure S38: Related to Figure 5. AICD plots (top) and 2D-ICSS (bottom) maps for CPDT-BBT in the (A) singlet and (B) triplet states, respectively, at $n = 8$.

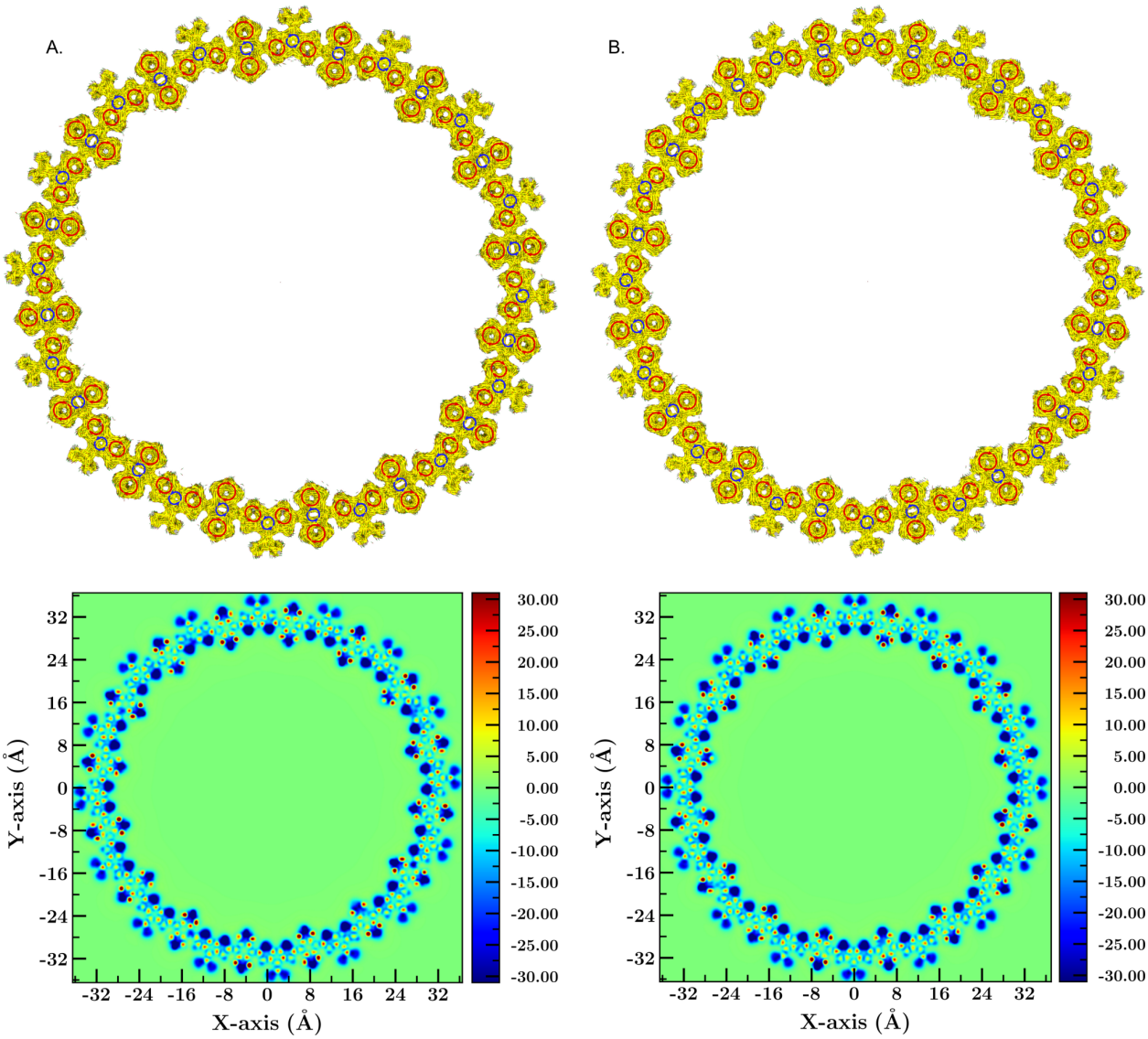

Figure S39: Related to Figure 5. AICD plots (top) and 2D-ICSS (bottom) maps for CPDT-BBT in the (A) singlet and (B) triplet states, respectively, at $n = 16$.

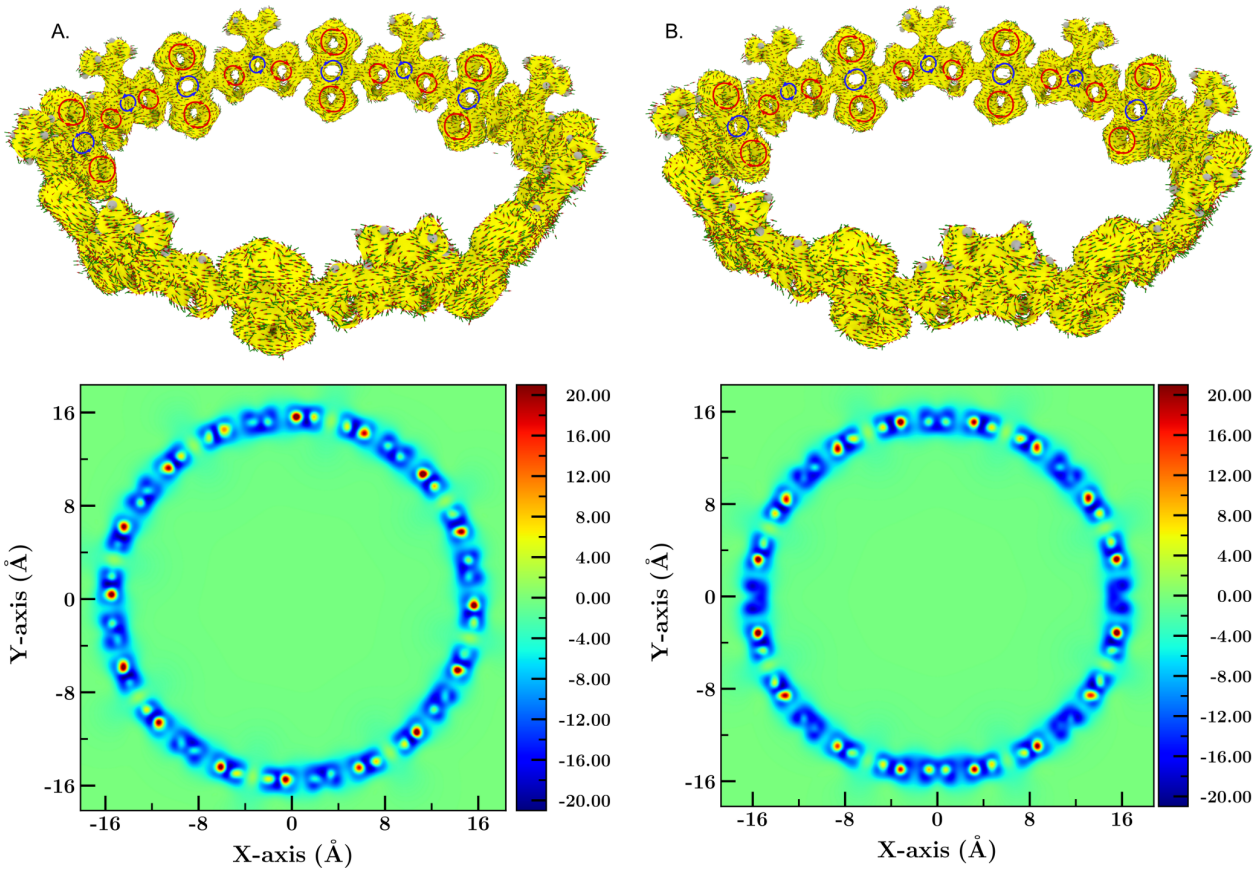

Figure S40: Related to Figure 5. AICD plots (top) and 2D-ICSS (bottom) maps for CPDS-BBT in the (A) singlet and (B) triplet states, respectively, at n = 8.

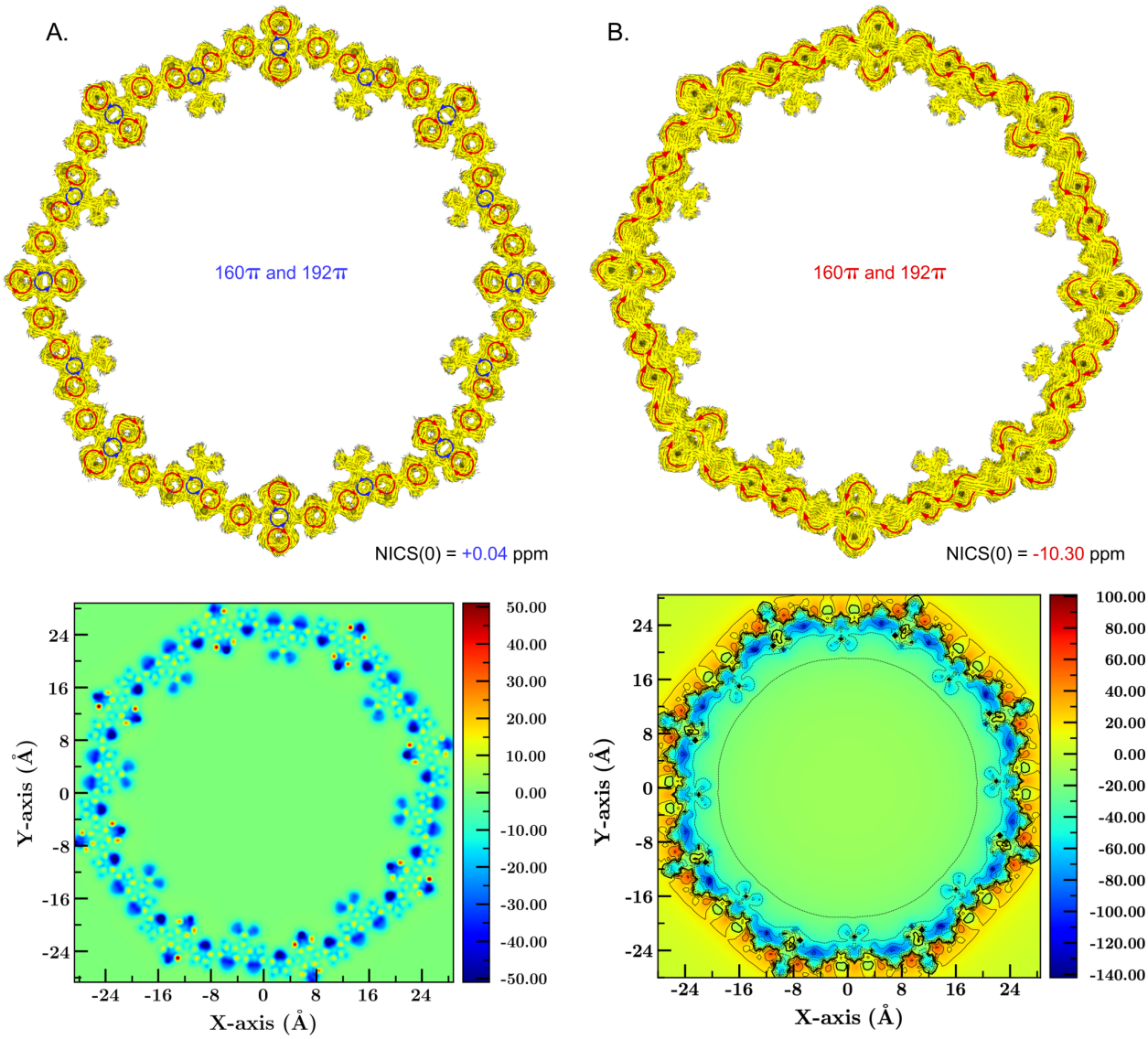

Figure S41: Related to Figure 5. AICD plots (top) and 2D-ICSS (bottom) maps for CPDS-BBT in the (A) singlet and (B) triplet states, respectively, at $n = 8 - \pi$.

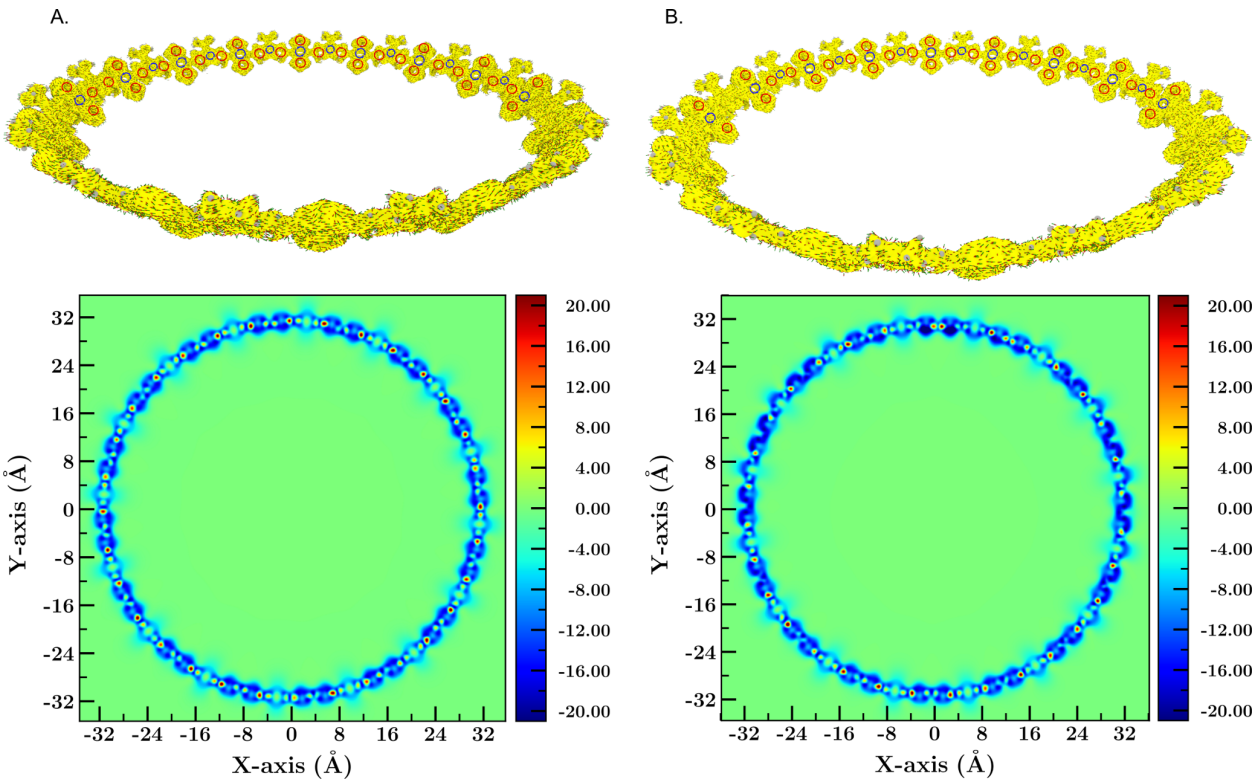

Figure S42: Related to Figure 5. AICD plots (top) and 2D-ICSS (bottom) maps for CPDS-BBT in the (A) singlet and (B) triplet states, respectively, at n = 16.

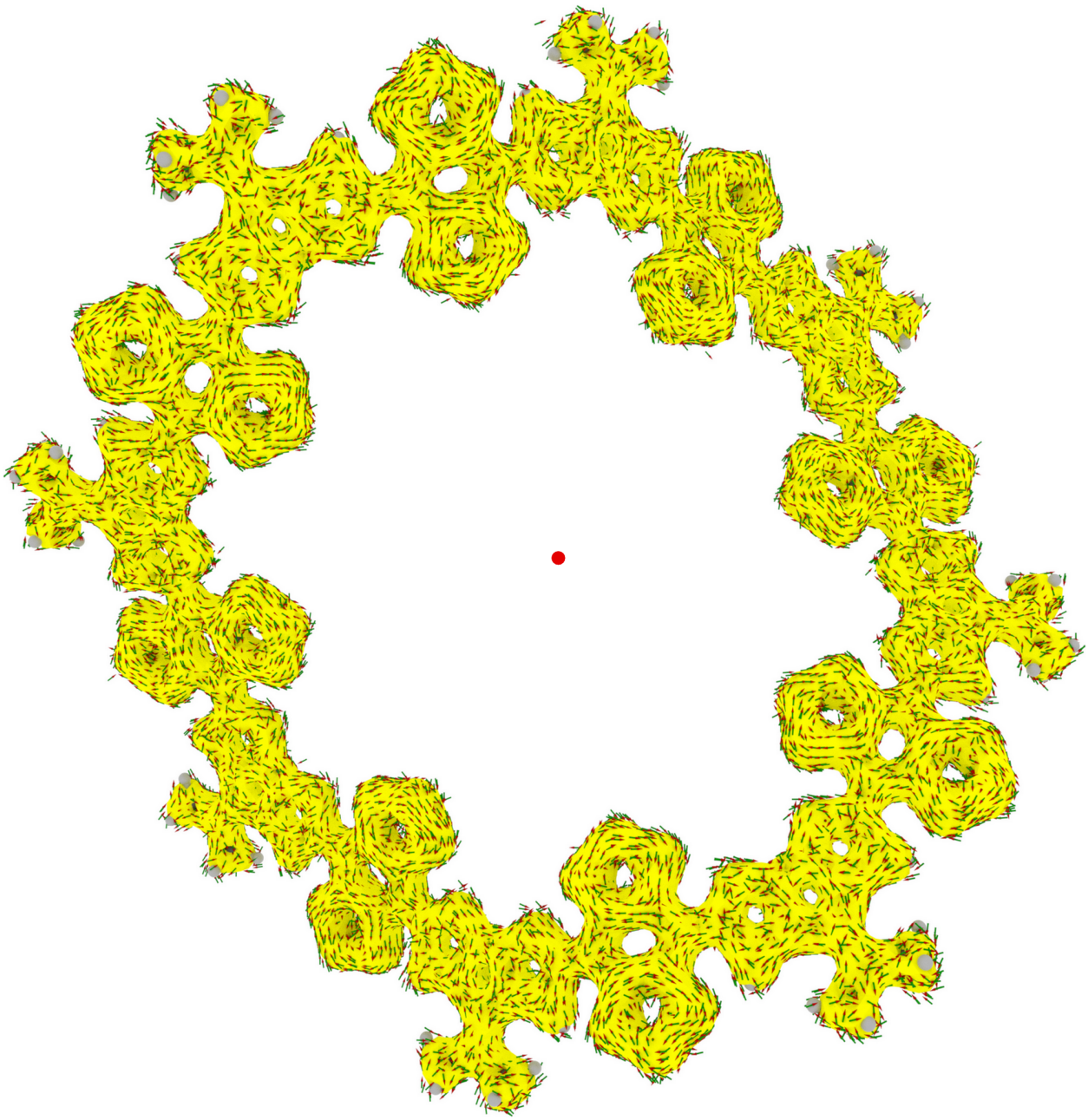

Figure S43: Related to Figure 5. Magnified AICD plot for CPDF-BBT in the singlet state at $n = 8$. The arrow indicate the direction of the applied magnetic field.

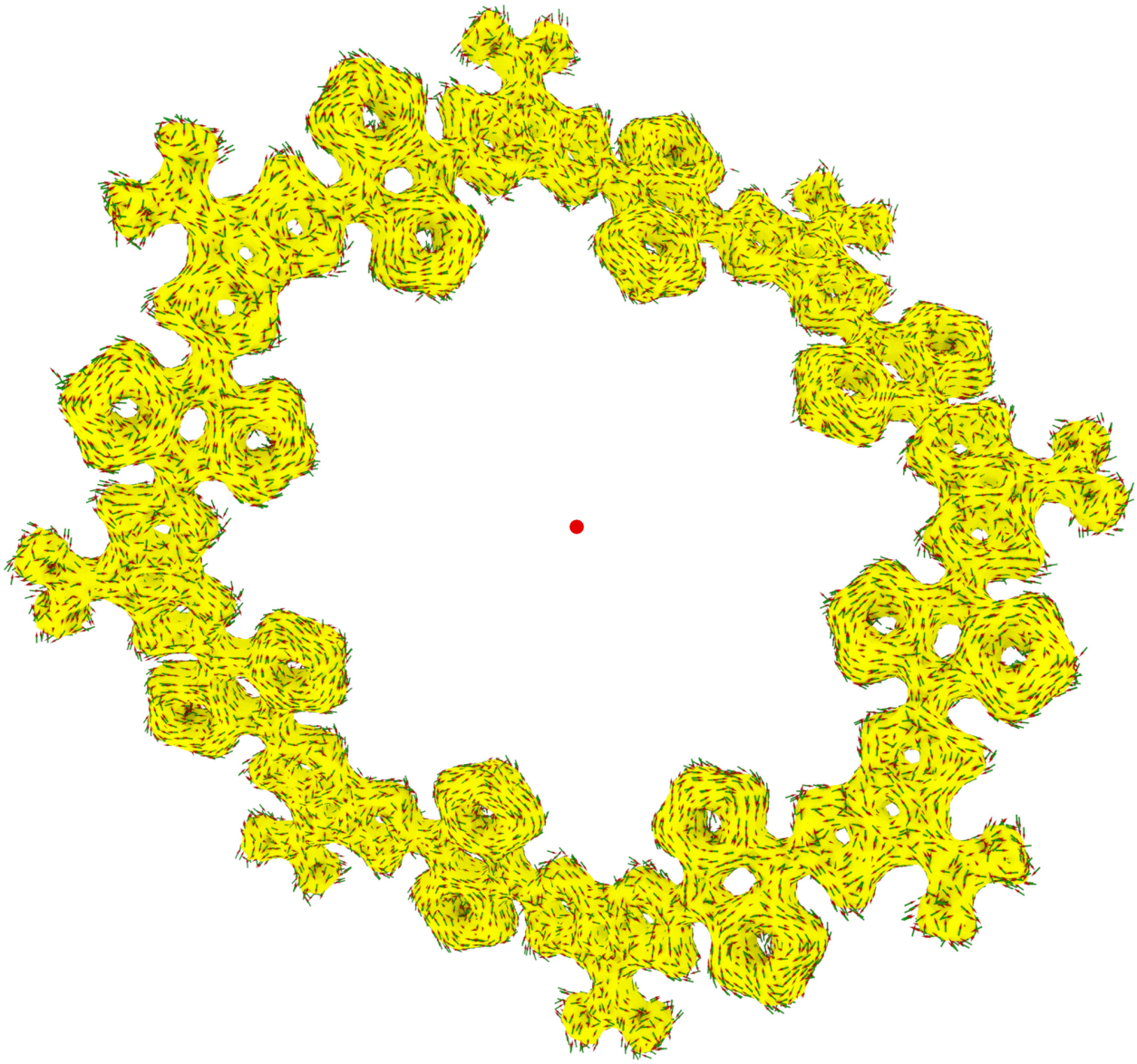

Figure S44: Related to Figure 5. Magnified AICD plot for CPDF-BBT in the triplet state at n = 8. The arrow indicate the direction of the applied magnetic field.

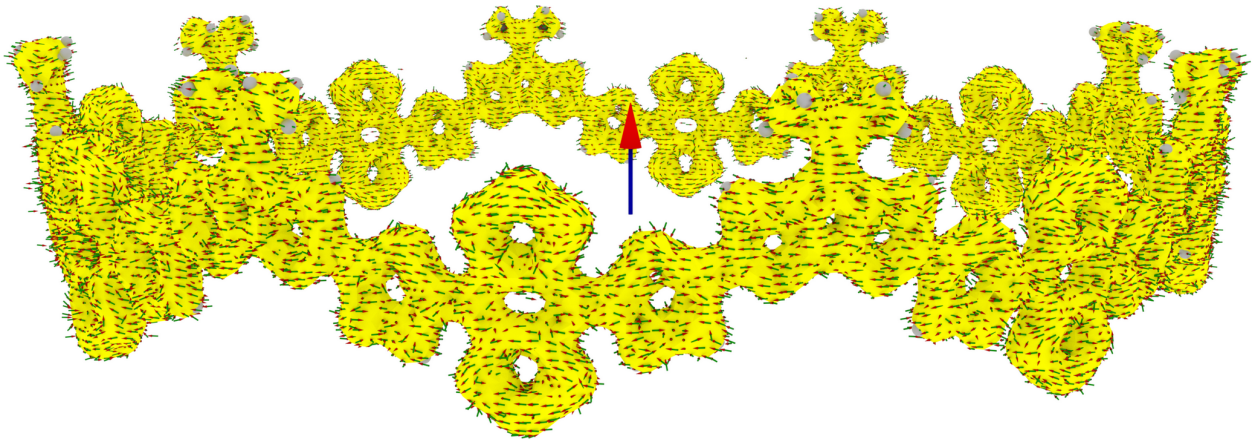

Figure S45: Related to Figure 5. Magnified AICD plot for CPDF-BBT in the singlet state at $n = 8 - \pi$. The arrow indicate the direction of the applied magnetic field.

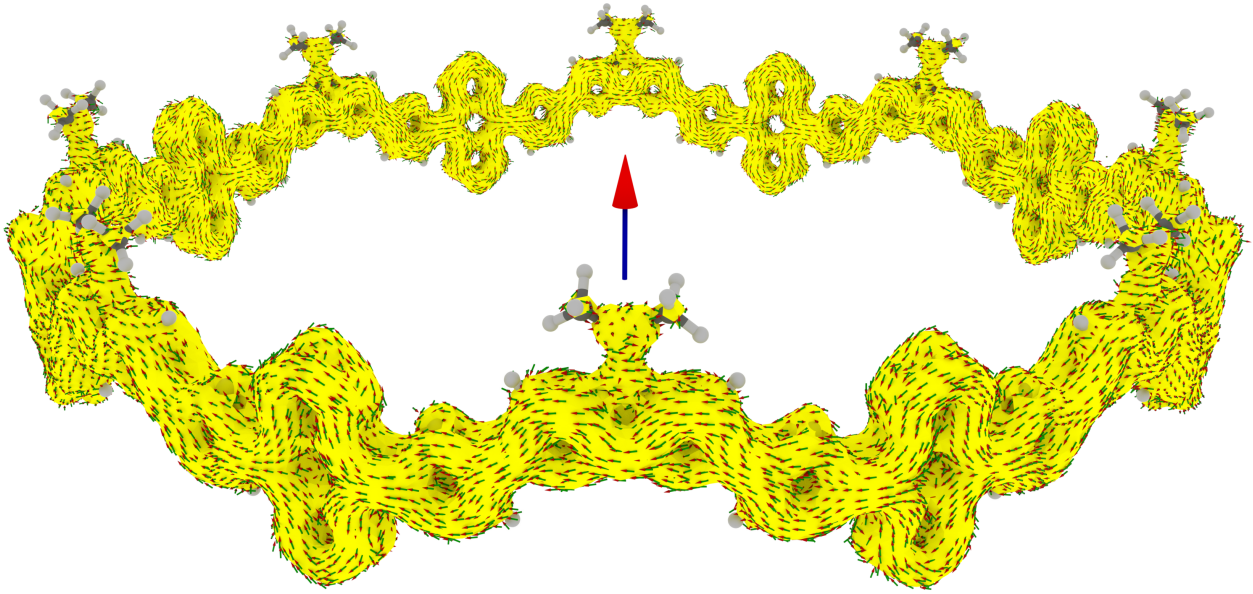

Figure S46: Related to Figure 5. Magnified AICD plot for CPDF-BBT in the triplet state at $n = 8 - \pi$. The arrow indicate the direction of the applied magnetic field.

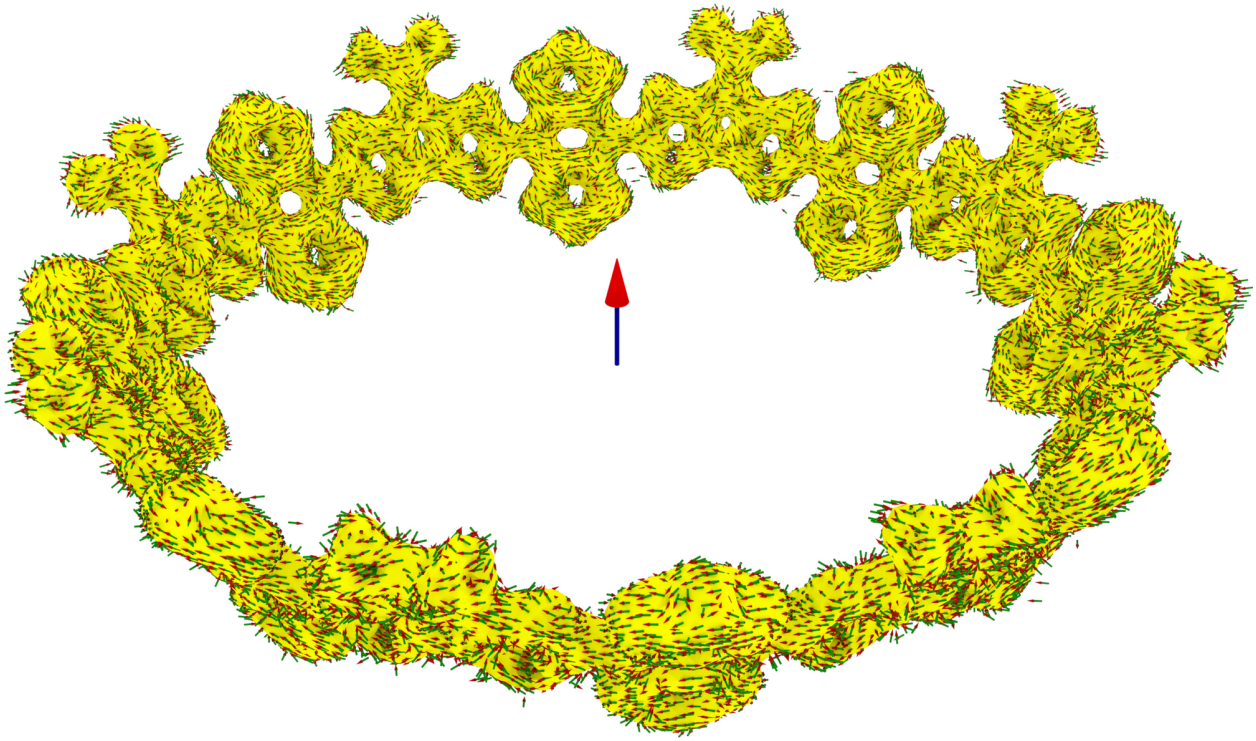

Figure S47: Related to Figure 5. Magnified AICD plot for CPDT-BBT in the singlet state at $n = 8$. The arrow indicate the direction of the applied magnetic field.

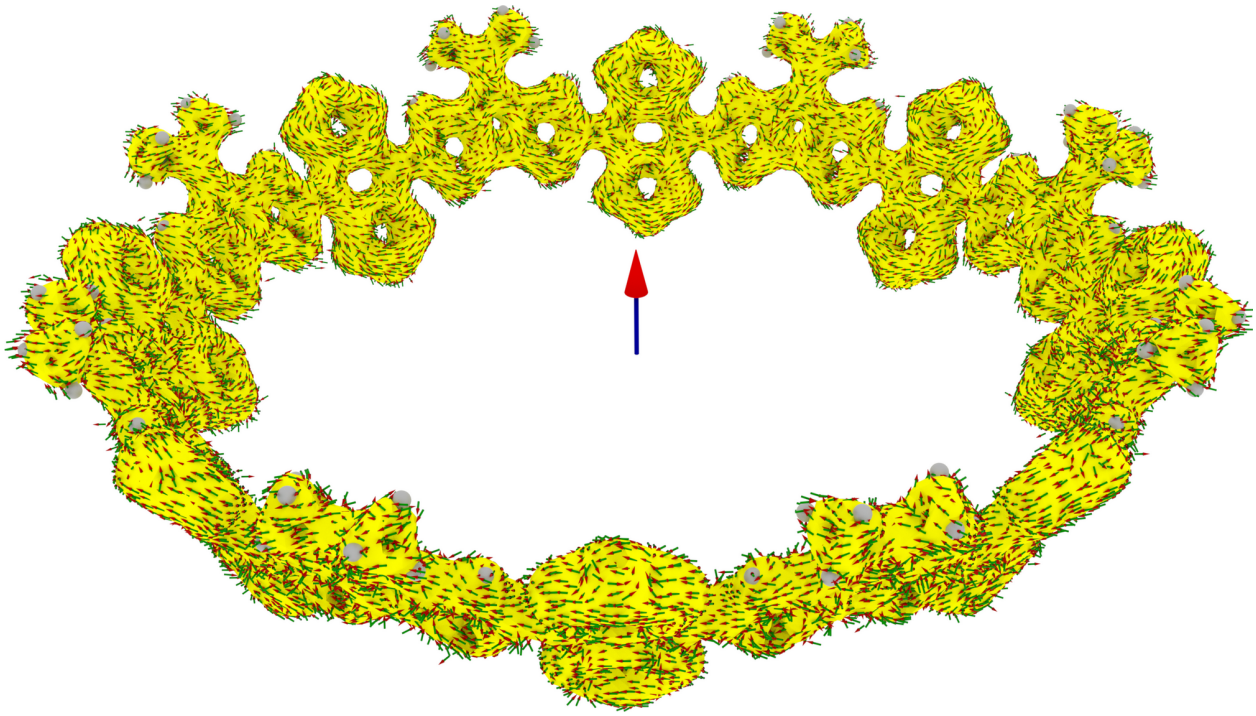

Figure S48: Related to Figure 5. Magnified AICD plot for CPDT-BBT in the triplet state at $n = 8$. The arrow indicate the direction of the applied magnetic field.

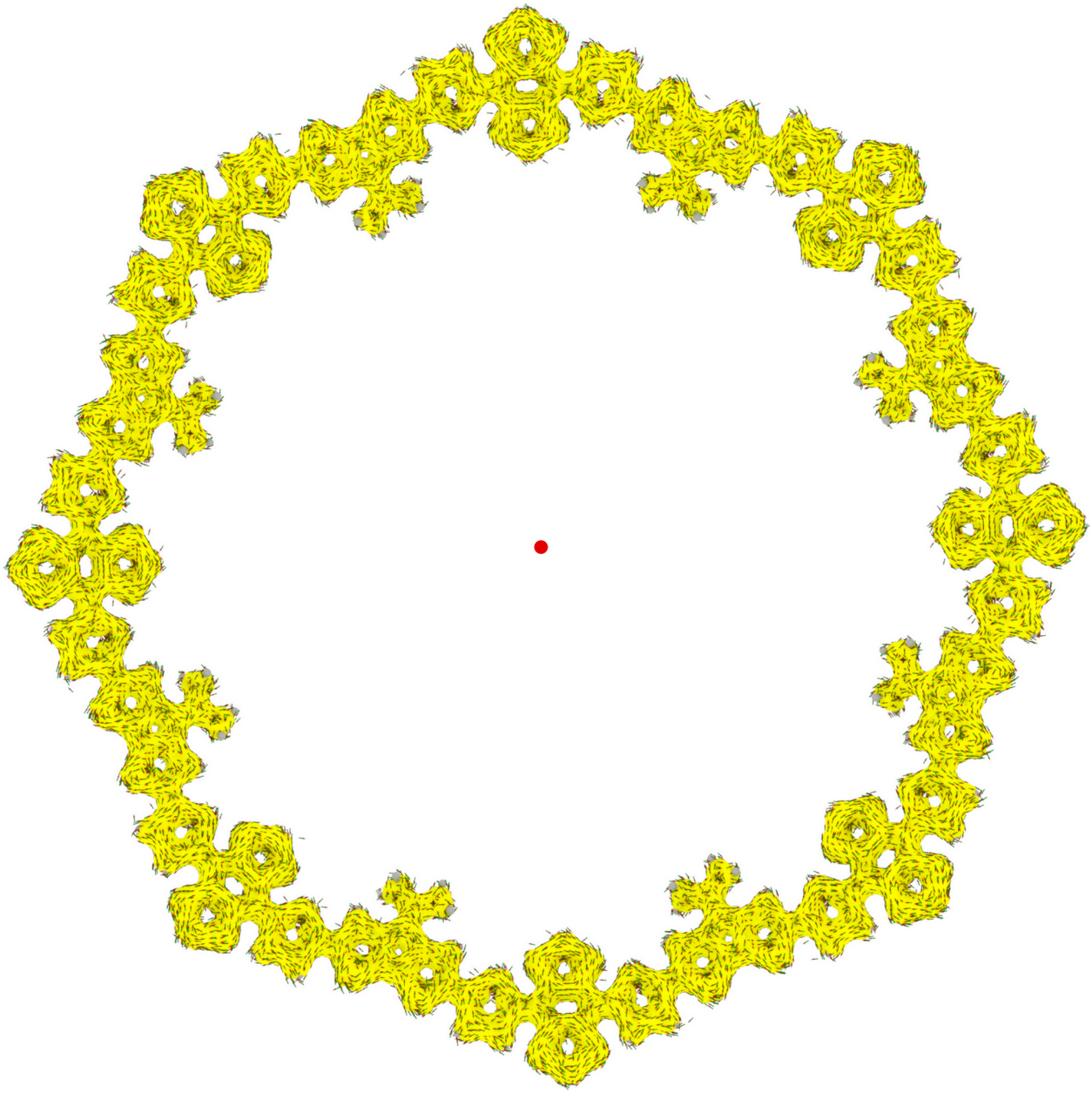

Figure S49: Related to Figure 5. Magnified AICD plot for CPDT-BBT in the singlet state at $n = 8 - \pi$. The arrow indicate the direction of the applied magnetic field.

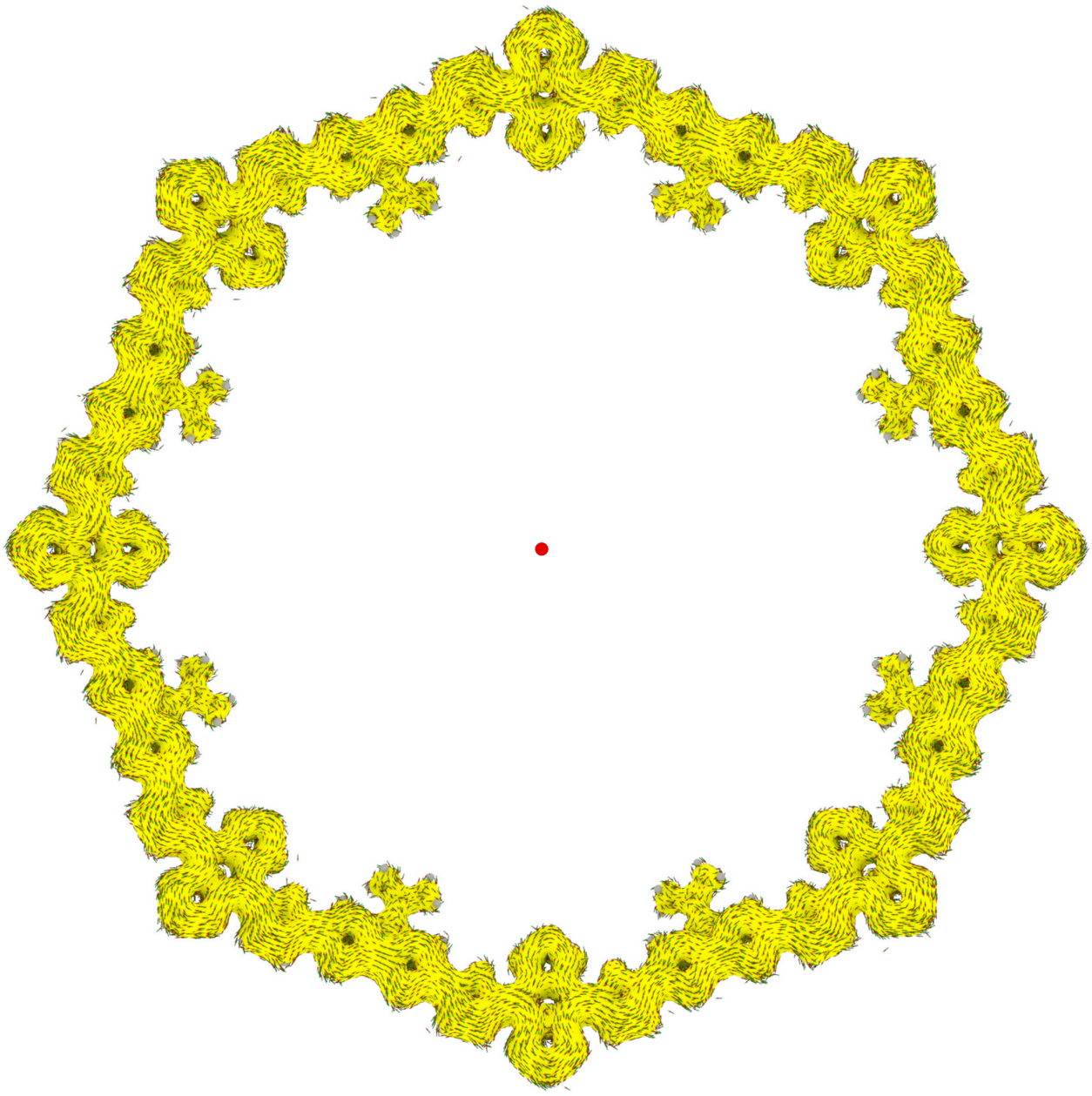

Figure S50: Related to Figure 5. Magnified AICD plot for CPDT-BBT in the triplet state at $n = 8 - \pi$. The arrow indicate the direction of the applied magnetic field.

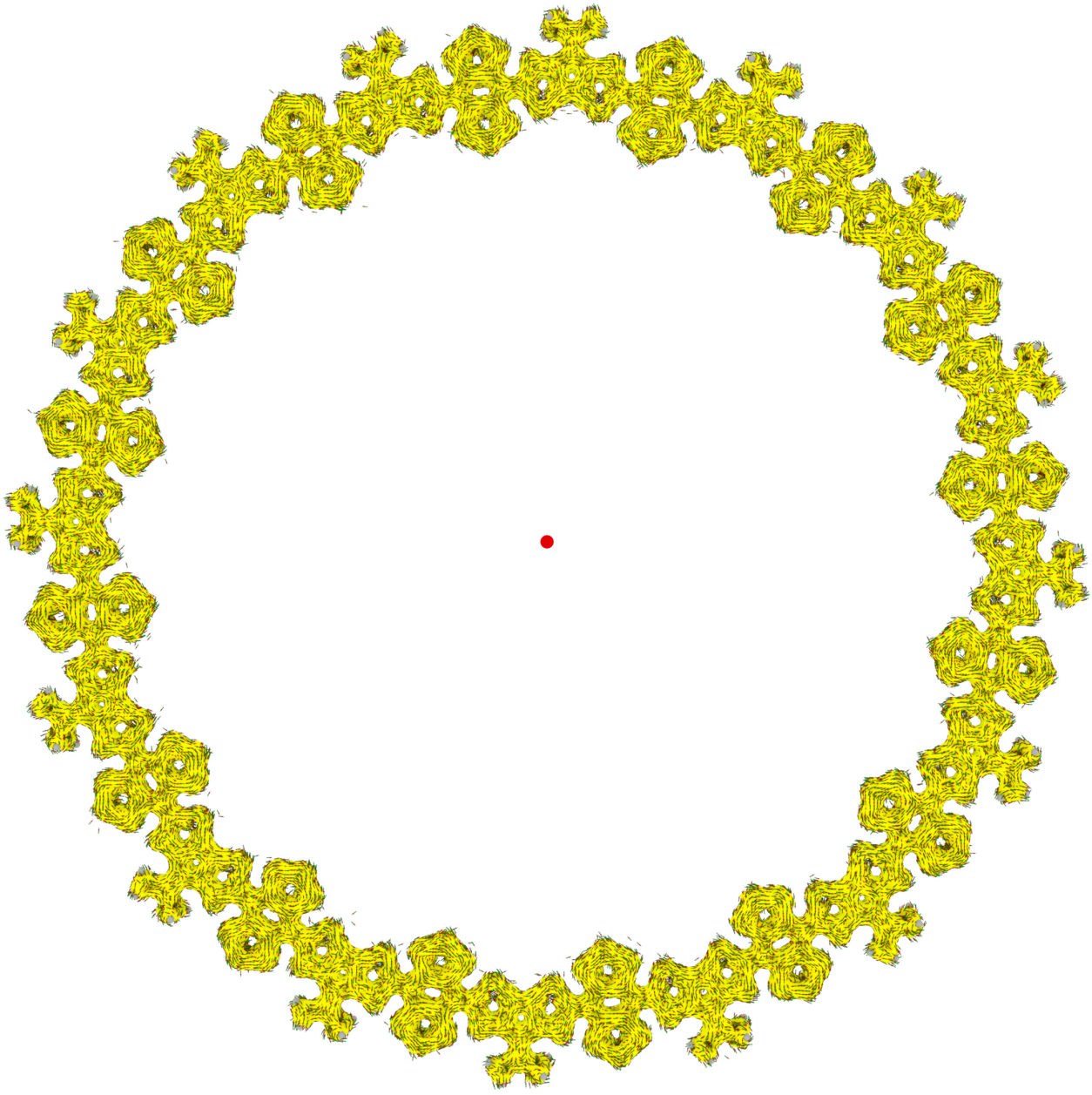

Figure S51: Related to Figure 5. Magnified AICD plot for CPDT-BBT in the singlet state at n = 16. The arrow indicate the direction of the applied magnetic field.

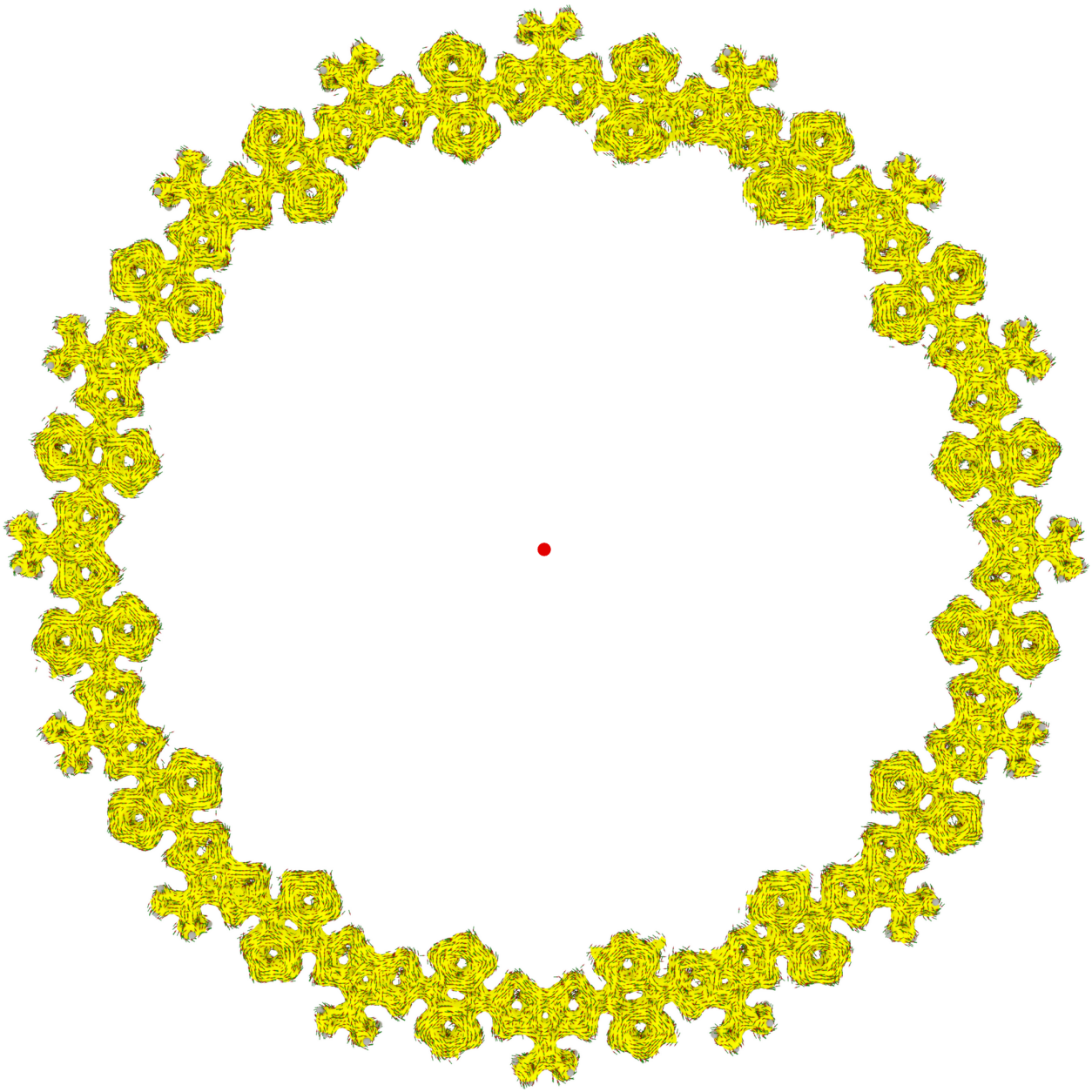

Figure S52: Related to Figure 5. Magnified AICD plot for CPDT-BBT in the triplet state at n = 16. The arrow indicate the direction of the applied magnetic field.

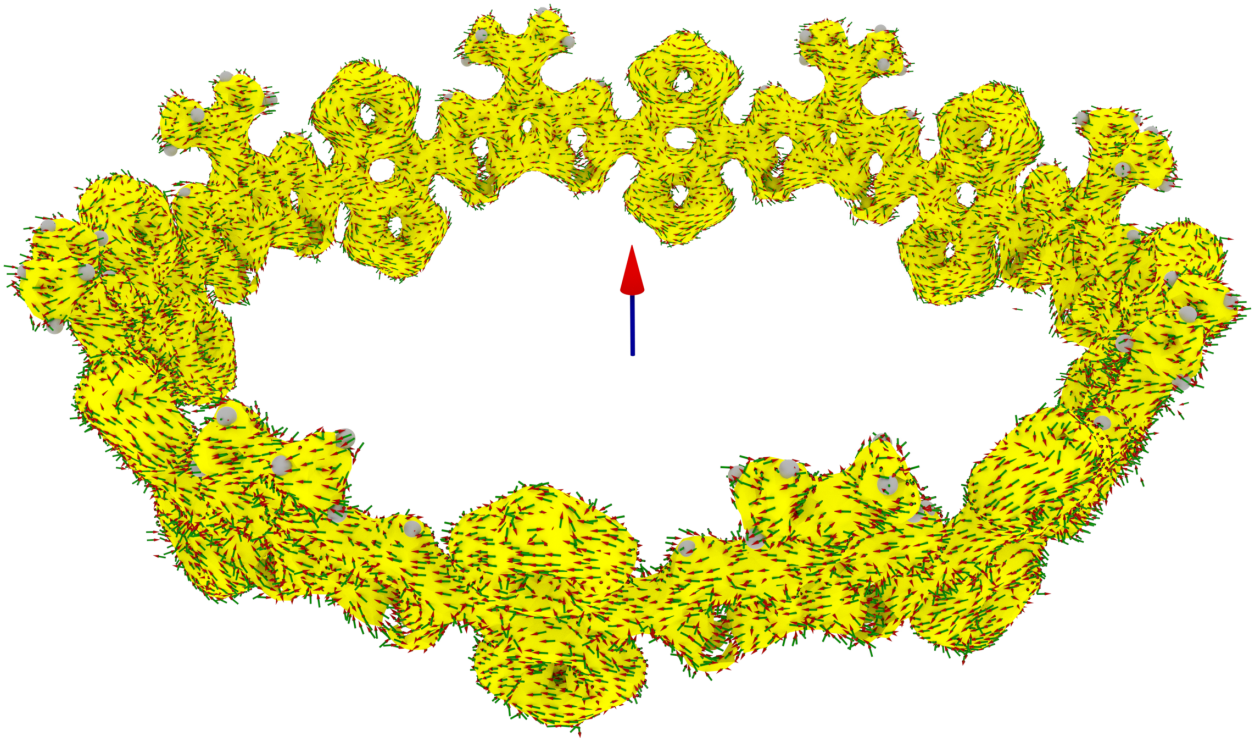

Figure S53: Related to Figure 5. Magnified AICD plot for CPDS-BBT in the singlet state at n = 8. The arrow indicate the direction of the applied magnetic field.

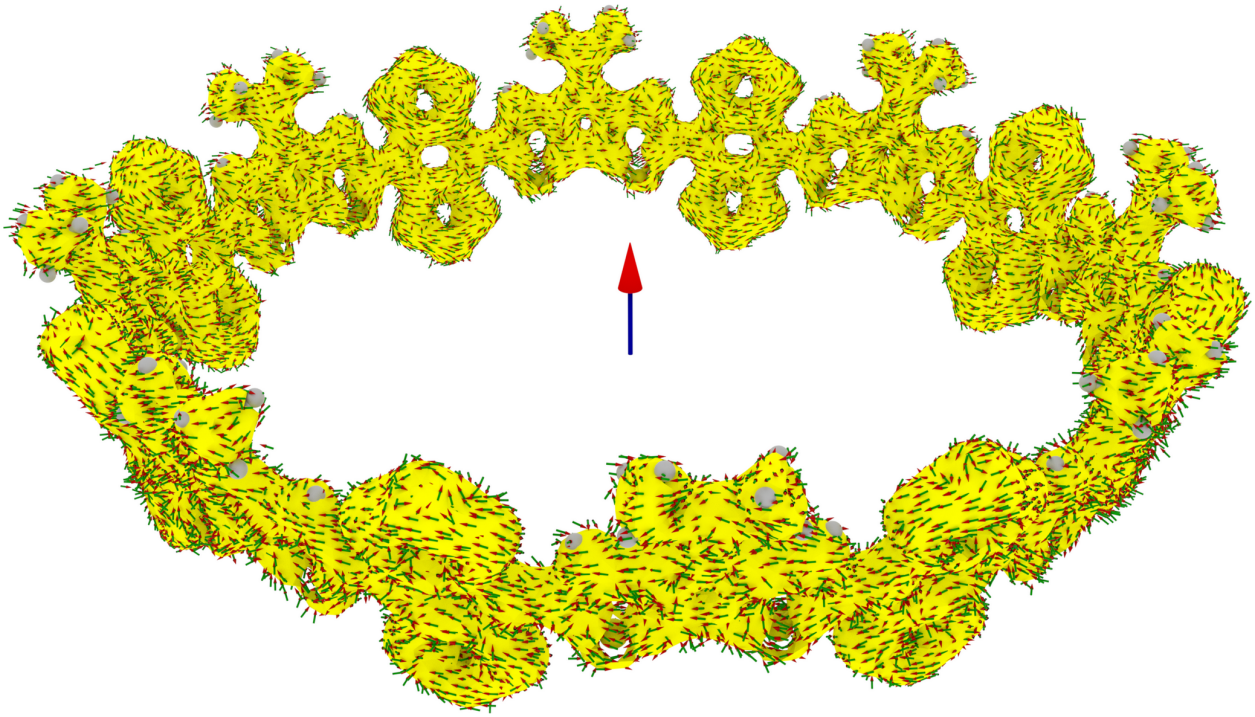

Figure S54: Related to Figure 5. Magnified AICD plot for CPDS-BBT in the triplet state at n = 8. The arrow indicate the direction of the applied magnetic field.

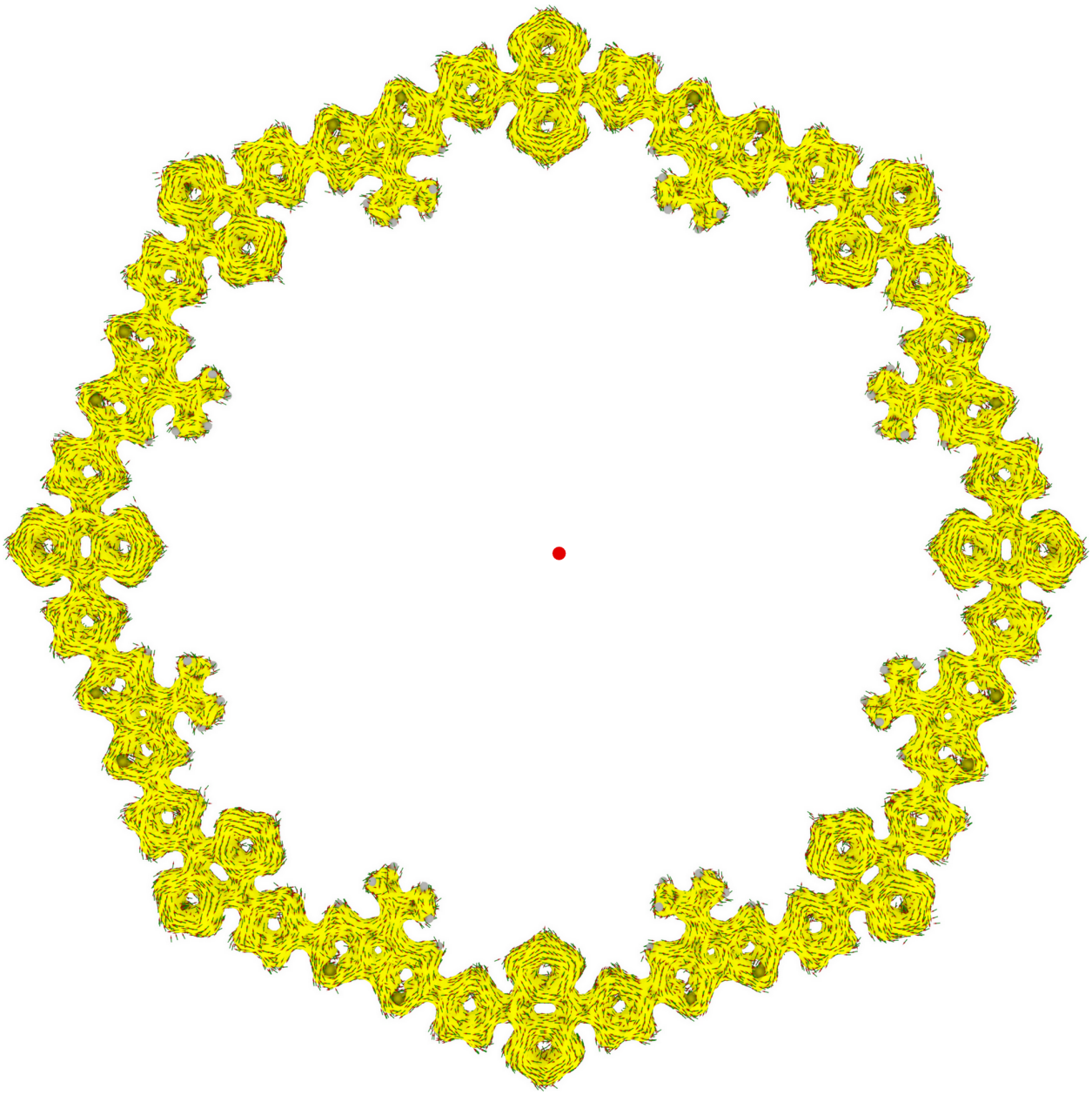

Figure S55: Related to Figure 5. Magnified AICD plot for CPDS-BBT in the singlet state at $n = 8 - \pi$. The arrow indicate the direction of the applied magnetic field.

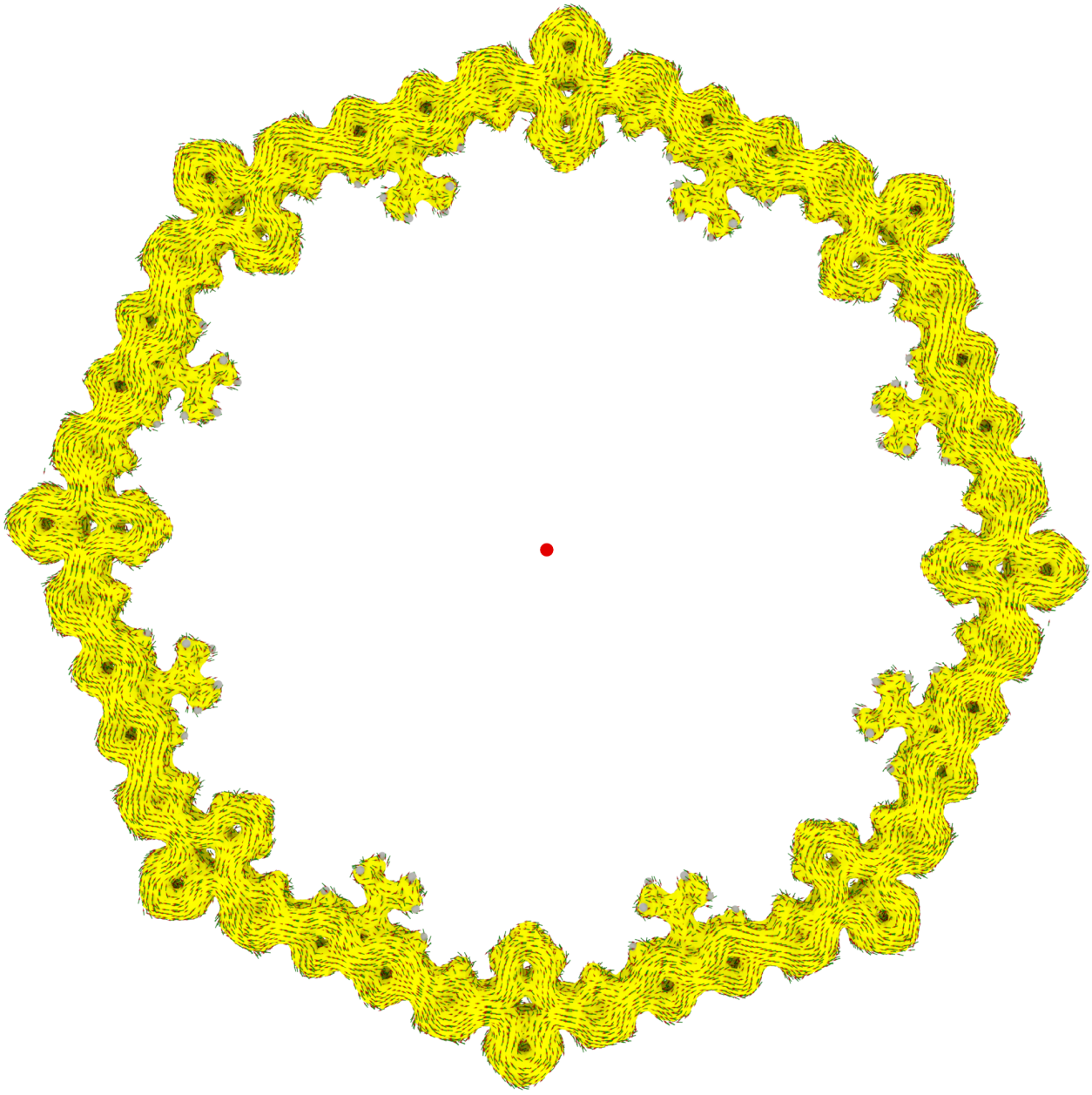

Figure S56: Related to Figure 5. Magnified AICD plot for CPDS-BBT in the triplet state at $n = 8 - \pi$. The arrow indicate the direction of the applied magnetic field.

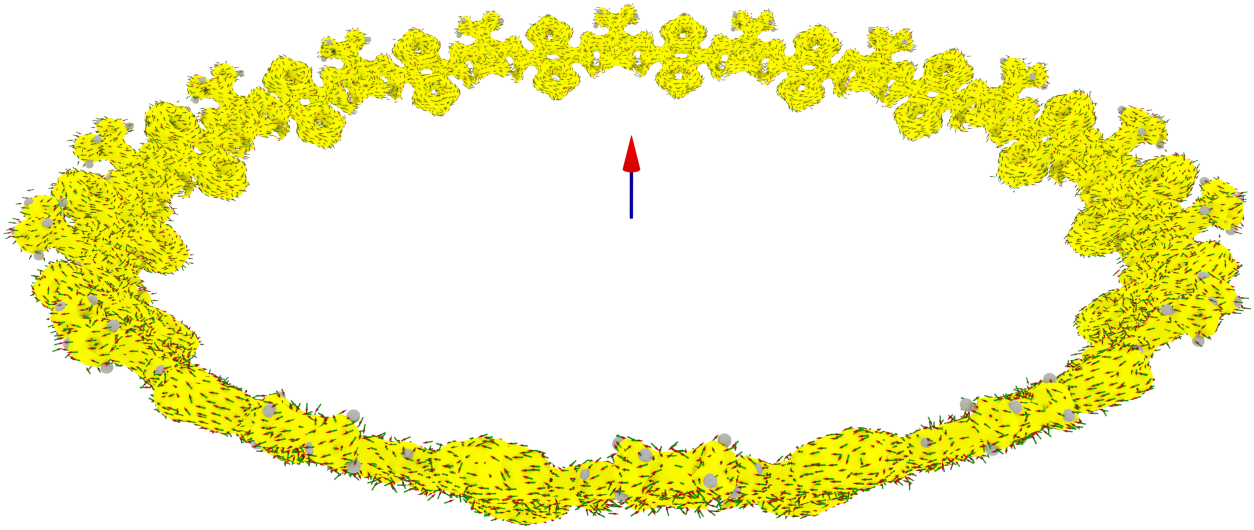

Figure S57: Related to Figure 5. Magnified AICD plot for CPDS-BBT in the singlet state at n = 16. The arrow indicate the direction of the applied magnetic field.

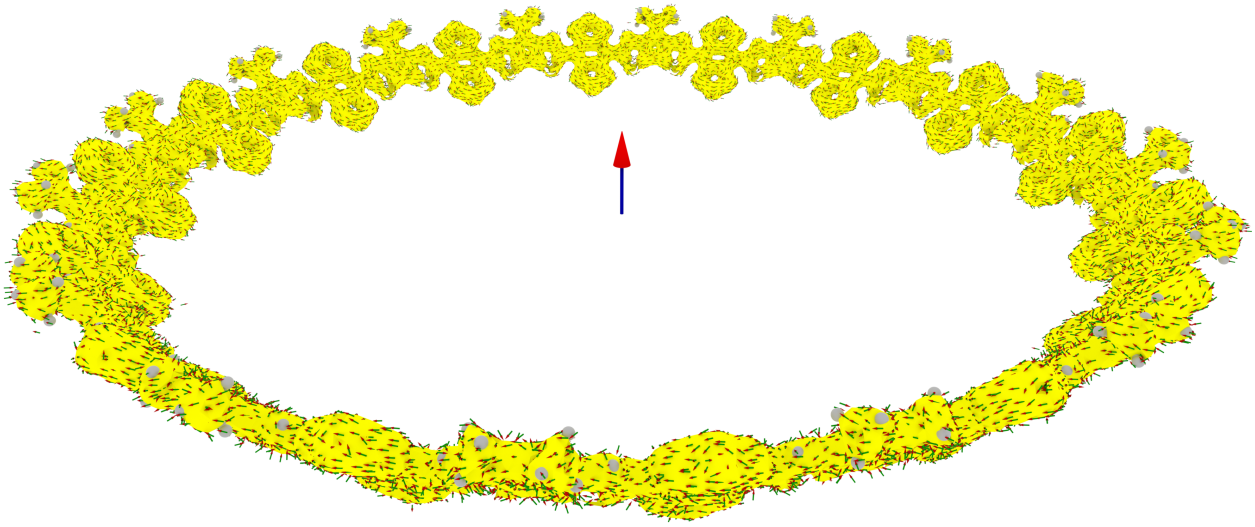

Figure S58: Related to Figure 5. Magnified AICD plot for CPDS-BBT in the triplet state at n = 16. The arrow indicate the direction of the applied magnetic field.

Movie S1: Related to Figure 2. AIMD simulation trajectory for the CPDT-BBT (n = 8) macrocycle.

Transparent Methods

Computational details

All the calculations are performed with Gaussian 16 software package (Frisch et al., 2016). Molecular geometries for the singlet and higher electronic states of the model oligomers (n = 8, 16, and 8 − π) are optimized using hybrid density functional, B3LYP (Becke, 1993). Calculation on CPDF-BBT with $n = 8 - \pi$ indicates that the C4 symmetric configuration is only 0.05 kJ/mol lower than the C1 symmetry, C2 and C8 essentially have the same energy as C1. The C1, C2, C4, and C8 geometries have same Boltzmann weights. Therefore, all the calculations are performed at C1 symmetry, without any further symmetry search in the CPDF-, CPDT-, and CPDS-BBT macromolecules. Our study on linear D−A polymer indicates the gas phase calculated properties corroborate the experimental observation (London et al., 2019); therefore, the geometry optimizations and electronic properties are calculated in the gas phase. Also, at the computational limit, the calculated electronic properties on a n = 8 repeat unit reproduces the experimental findings (London et al., 2019). Therefore, we have started with n = 8 repeat units of CPDF-, CPDT-, and CPDS-BBT macromolecules and followed the oligomer approach.

For the *Se* atom, LANL2DZdp basis set is used along with associated effective core potentials (Schuchardt et al., 2007), with 6-31G(*d, p*) (Francl et al., 1982) basis set for other the atoms. All parameters for geometry optimizations set to defaults. For the oligomers, geometries considered optimized once the RMS forces on all atoms converged to zero (Foresman and Frisch, 2015). A single-reference wave function cannot determine the electronic structure of open-shell molecules (Abe, 2013). Multi-reference configuration schemes are computationally very demanding; therefore, a broken-symmetry (BS) (Noodleman, 1981) wave function used to characterize the open-shell singlet state. The triplet and higher spin-states are optimized from the BS optimized

geometry using an unrestricted wave function.

A molecule with two unpaired electrons localized at two degenerate or nearly degenerate non-bonding molecular orbitals (NBMOs) is a diradical (Abe, 2013). The electronic properties of an open-shell molecule is best defined by a quantitative multi-radical (or polyradical) index, y_i (i = 0–7), which is an indication of the degree of localization of pair of electrons at different sites. A high value of y_i indicates a high degree of electron correlation, i.e., doubly-excited electronic configuration has a higher weight in the ground-state electronic wave function (Nakano, 2017). Theoretically, y_i is defined as the occupation number of the lowest unoccupied natural orbitals (LUNO+i) (Head-Gordon, 2003). In case of a closed-shell molecule, the orbital occupancy can be either 2 (doubly occupied) or 0 (empty orbital), however, in case of an open-shell molecule, this occupancy varies in between 0 and 2 (Nakano, 2017). Therefore, for a closed-shell molecule, the LUNO+i occupancy is 0 and it increases as the molecule start to develop open-shell character, and approaches a value of 1 for a pure open-shell molecule. Therefore, a closed-shell (y_i = 0), intermediate ($0 < y_i < 1$), and pure (y_i = 1) polyradical molecule can be defined by y_i values (London et al., 2019). Here, the polyradical (y_i) indexes obtained from population analysis of natural orbitals as the occupation numbers of lowest unoccupied natural orbitals (LUNOs).

Nucleus independent chemical shift (NICS(0)) (Schleyer et al., 2001) is computed by the gauge-independent atomic orbital (GIAO) (Ditchfield, 1974) method on the optimized geometry by single point energy calculation placing a ghost atom at the center of the macromolecules and also on each rings along the conjugated backbone. NICS is an excellent probe for the magnetic index of aromaticity or antiaromaticity of a molecule. A high negative NICS value indicates molecule as aromatic, a positive NICS value indicates as antiaromatic, and a 0 (zero) value indicates the corresponding molecule as nonaromatic.

NBO6 program package (Glendening et al., 2013) is used to predict the spin location from natural spin densities of the Kohn-Sham MOs. Time-dependent DFT (TDDFT) calculation at the (U)CAM-B3LYP (Yanai et al., 2004) level is used to simulate the lowest 20 singlet excited

states with Tamm-Dancoff approximation (Hirata and Head-Gordon, 1999) in the presence of implicit solvent. Integral equation formalism (IEFPCM) of the Polarizable Continuum Model (PCM) (Tomasi et al., 2005) is used with chloroform as the implicit solvent. AICD (anisotropy of the induced current density) plots are generated by method developed by Herges *et al.* (Geuenich et al., 2005) and 2D-ICSS (2D-iso-chemical shielding surface) maps generated by the method developed by Klod *et al.* (Klod and Kleinpeter, 2001)

Ab initio molecular dynamics (AIMD) simulations are performed with CP2K software package with QuickStep module (VandeVondele et al., 2005). AIMD simulations are carried out for 1.30 ps with 0.5 fs time step. One CPDT-BBT macromolecule with $n = 8$ repeat units is placed in a large ($50 \times 50 \times 30$ Å) periodic box. Simulation is performed with canonical ensemble (NVT) and Nosé-Hoover thermostat is used to maintain temperature at 298.15 K (Nosé, 1984; Hoover, 1985). The core-electronic states are described with Goedecker-Teter-Hutter (GTH) pseudopotentials and DZVP-MOLOPT basis set is used for all atoms (Goedecker et al., 1996; VandeVondele and Hutter, 2007). 600 Ry energy cutoff is used with the finer mesh cutoff set at 50 Ry. PBE functional is used for the exchange and correlation interaction with Grimme's DFT−D3 pair potential (Perdew et al., 1996; Grimme et al., 2010). SCF cycles are converged at 1×10^{-6} with energy convergence set to 1×10^{-10}.

The root mean square deviation (RMSD) of CPDT-BBT macromolecule ($n = 8$) is calculated using MDTraj code (McGibbon et al., 2015). RMSD measures the structural deviation of a molecule from a reference structure. The optimized geometry of CPDT-BBT from B3LYP functional is used as a reference frame. At each time step, MDTraj aligned structure to eliminate the translational and orientational changes of the entire structure, which allowed us to quantify the deviation caused by internal coordinate change. The RMSD is calculated using to the following equation:

$$RMSD(t) = \sqrt{\sum_{i=1}^{N} \frac{1}{N}[r_i(0) - r_i(t)]^2} \quad (1)$$

Supplemental References

Abe, M., 2013. Diradicals. Chem. Rev. 113, 7011–7088.

Becke, A.D., 1993. A new mixing of hartree–fock and local density-functional theories. J. Chem. Phys. 98, 1372–1377.

Ditchfield, R., 1974. Self-consistent perturbation theory of diamagnetism: I. a gauge-invariant lcao method for nmr chemical shifts. Mol. Phys. 27, 789–807.

Foresman, J.B., Frisch, Æ., 2015. Exploring Chemistry with Electronic Structure Methods. 3 ed., Gaussian, Gaussian Inc. Wallingford CT.

Francl, M.M., Pietro, W.J., Hehre, W.J., Binkley, J.S., Gordon, M.S., DeFrees, D.J., Pople, J.A., 1982. Self-consistent molecular orbital methods. xxiii. a polarization-type basis set for second-row elements. J. Chem. Phys. 77, 3654–3665.

Frisch, M.J., Trucks, G.W., Schlegel, H.B., Scuseria, G.E., Robb, M.A., Cheeseman, J.R., Scalmani, G., Barone, V., Petersson, G.A., Nakatsuji, H., Li, X., Caricato, M., Marenich, A.V., Bloino, J., Janesko, B.G., Gomperts, R., Mennucci, B., Hratchian, H.P., Ortiz, J.V., Izmaylov, A.F., Sonnenberg, J.L., Williams-Young, D., Ding, F., Lipparini, F., Egidi, F., Goings, J., Peng, B., Petrone, A., Henderson, T., Ranasinghe, D., Zakrzewski, V.G., Gao, J., Rega, N., Zheng, G., Liang, W., Hada, M., Ehara, M., Toyota, K., Fukuda, R., Hasegawa, J., Ishida, M., Nakajima, T., Honda, Y., Kitao, O., Nakai, H., Vreven, T., Throssell, K., Montgomery, Jr., J.A., Peralta, J.E., Ogliaro, F., Bearpark, M.J., Heyd, J.J., Brothers, E.N., Kudin, K.N., Staroverov, V.N., Keith, T.A., Kobayashi, R., Normand, J., Raghavachari, K., Rendell, A.P., Burant, J.C., Iyengar, S.S., Tomasi, J., Cossi, M., Millam, J.M., Klene, M., Adamo, C., Cammi, R., Ochterski, J.W., Martin, R.L., Morokuma, K., Farkas, O., Foresman, J.B., Fox, D.J., 2016. Gaussian 16 Revision B.01. Gaussian Inc. Wallingford CT.

Geuenich, D., Hess, K., Köhler, F., Herges, R., 2005. Anisotropy of the induced current density (acid), a general method to quantify and visualize electronic delocalization. Chem. Rev. 105, 3758–3772.

Glendening, E.D., Landis, C.R., Weinhold, F., 2013. Nbo 6.0: Natural bond orbital analysis program. J. Comput. Chem. 34, 1429–1437.

Goedecker, S., Teter, M., Hutter, J., 1996. Separable dual-space gaussian pseudopotentials. Phys. Rev. B 54, 1703.

Grimme, S., Antony, J., Ehrlich, S., Krieg, H., 2010. A consistent and accurate ab initio parametrization of density functional dispersion correction (dft-d) for the 94 elements h-pu. J. Chem. Phys. 132, 154104.

Head-Gordon, M., 2003. Characterizing unpaired electrons from the one-particle density matrix. Chem. Phys. Lett. 372, 508–511.

Hirata, S., Head-Gordon, M., 1999. Time-dependent density functional theory within the tamm–dancoff approximation. Chem. Phys. Lett. 314, 291–299.

Hoover, W.G., 1985. Canonical dynamics: Equilibrium phase-space distributions. Phys. Rev. A 31, 1695.

Klod, S., Kleinpeter, E., 2001. Ab initio calculation of the anisotropy effect of multiple bonds and the ring current effect of arenesapplication in conformational and configurational analysis. J. Chem. Soc., Perkin. Trans. 2 , 1893–1898.

London, A.E., Chen, H., Sabuj, M., Tropp, J., Saghayezhian, M., Eedugurala, N., Zhang, B., Liu, Y., Gu, X., Wong, B., Rai, N., Azoulay, J., 2019. A high-spin ground-state donor-acceptor conjugated polymer. Sci. Adv. 5, eaav2336.

McGibbon, R.T., Beauchamp, K.A., Harrigan, M.P., Klein, C., Swails, J.M., Hernández, C.X., Schwantes, C.R., Wang, L.P., Lane, T.J., Pande, V.S., 2015. Mdtraj: a modern open library for the analysis of molecular dynamics trajectories. Biophys. J 109, 1528–1532.

Nakano, M., 2017. Open-shell-character-based molecular design principles: Applications to nonlinear optics and singlet fission. Chem. Rec. 17, 27–62.

Noodleman, L., 1981. Valence bond description of antiferromagnetic coupling in transition metal dimers. J. Chem. Phys. 74, 5737–5743.

Nosé, S., 1984. A unified formulation of the constant temperature molecular dynamics methods. J. Chem. Phys. 81, 511–519.

Perdew, J.P., Burke, K., Ernzerhof, M., 1996. Generalized gradient approximation made simple. Phys. Rev. Lett. 77, 3865.

Schleyer, P.v.R., Manoharan, M., Wang, Z.X., Kiran, B., Jiao, H., Puchta, R., van Eikema Hommes, N.J., 2001. Dissected nucleus-independent chemical shift analysis of π-aromaticity and antiaromaticity. Org. Lett. 3, 2465–2468.

Schuchardt, K.L., Didier, B.T., Elsethagen, T., Sun, L., Gurumoorthi, V., Chase, J., Li, J., Windus, T.L., 2007. Basis set exchange: a community database for computational sciences. J. Chem. Inf. Model. 47, 1045–1052.

Tomasi, J., Mennucci, B., Cammi, R., 2005. Quantum mechanical continuum solvation models. Chem. Rev. 105, 2999–3094.

VandeVondele, J., Hutter, J., 2007. Gaussian basis sets for accurate calculations on molecular systems in gas and

condensed phases. J. Chem. Phys. 127, 114105.

VandeVondele, J., Krack, M., Mohamed, F., Parrinello, M., Chassaing, T., Hutter, J., 2005. Quickstep: Fast and accurate density functional calculations using a mixed gaussian and plane waves approach. Comput. Phys. Commun. 167, 103–128.

Yanai, T., Tew, D.P., Handy, N.C., 2004. A new hybrid exchange–correlation functional using the coulomb-attenuating method (cam-b3lyp). Chem. Phys. Lett. 393, 51–57.